



---

Università degli Studi Roma Tre  
Dipartimento di Matematica e Fisica “*E. Amaldi*”

**SEARCH FOR CHARGED LEPTON FLAVOUR VIOLATION  
IN  $\tau \rightarrow 3\mu$  CHANNEL AT *BelleII***

**Alberto Martini**  
Ph.D. Degree in Physics  
XXXIII Cycle

Ph.D. Program Coordinator: Prof. G. Degrassi

Supervisors: Dott. Paolo Branchini  
Dott. Enrico Graziani



# Contents

<b>Introduction</b>	<b>1</b>
<b>1 Physics motivations</b>	<b>3</b>
1.1 Standard Model of particle physics . . . . .	3
1.1.1 Neutrino oscillation phenomenon . . . . .	6
1.1.2 Charged Lepton Flavour Violation . . . . .	8
1.1.2.1 $\tau^\pm \rightarrow \mu^\pm \mu^\mp \mu^\pm$ in the Standard Model . . . . .	9
1.1.2.2 $\tau^\pm \rightarrow \mu^\pm \mu^\mp \mu^\pm$ in New Physics Model . . . . .	10
1.2 Experimental status of Lepton Flavour Violation in $\tau \rightarrow \mu$ transitions . . . . .	14
1.2.1 Experimental challenges and advantages for the $\tau^\pm \rightarrow$ $\mu^\pm \mu^\mp \mu^\pm$ search at <i>BelleII</i> . . . . .	16
<b>2 The <i>BelleII</i> experiment</b>	<b>19</b>
2.1 The accelerator SuperKEKB . . . . .	19
2.1.1 Nano-beam scheme . . . . .	21
2.1.2 Particle production and environment advantages . . . . .	23
2.2 The <i>BelleII</i> detector . . . . .	24
2.2.1 Pixel vertex detector . . . . .	27
2.2.2 Silicon-strip vertex detector . . . . .	27
2.2.3 Central Drift Chamber . . . . .	28
2.2.4 Particles identification system . . . . .	28
2.2.4.1 Time-Of-Propagation counter . . . . .	28
2.2.4.2 Aerogel Ring-Imaging Cherenkov detector . . . . .	30
2.2.5 Electromagnetic calorimeter . . . . .	31
2.2.6 $K_L$ and $\mu$ detector . . . . .	32
2.2.7 Trigger . . . . .	35
2.3 <i>BelleII</i> software general description . . . . .	36
<b>3 Muon identification at the <i>BelleII</i> experiment</b>	<b>39</b>
3.1 Muon identification in the KLM . . . . .	40

3.1.1	Track extrapolation . . . . .	41
3.1.2	Likelihood determination . . . . .	42
3.2	Muon identification performances in $e^+e^- \rightarrow \mu^+\mu^-\gamma$ channel .	46
3.2.1	Efficiency definition . . . . .	46
3.2.2	Event selection . . . . .	47
3.2.3	Systematic uncertainty . . . . .	48
3.2.4	muonID efficiency results . . . . .	49
3.3	Mis-identification rate from hadrons . . . . .	51
<b>4</b>	<b>Analysis strategy of the <math>\tau^\pm \rightarrow \mu^\pm \mu^\mp \mu^\pm</math> decay</b>	<b>53</b>
4.1	Analysis strategy in short . . . . .	53
4.2	Data-set description . . . . .	55
4.2.1	Event reconstruction criteria . . . . .	55
4.2.2	Signal region definition . . . . .	57
4.2.2.1	$M_{3\mu}$ and $\Delta E_{3\mu}$ correlation study . . . . .	57
4.2.2.2	$M_{3\mu}$ and $\Delta E_{3\mu}$ fit . . . . .	58
4.3	Background rejection . . . . .	59
4.3.1	Discriminating variable description . . . . .	59
4.3.2	MuonID optimisation procedure . . . . .	62
4.3.3	Analysis optimisation procedure . . . . .	63
4.3.4	Additional hand made selection . . . . .	65
4.4	Analysis comparison with previous results . . . . .	70
<b>5</b>	<b>Data-MC corrections and evaluation of systematic uncertainties</b>	<b>71</b>
5.1	Control sample description . . . . .	72
5.2	Trigger definitions . . . . .	72
5.3	Signal systematics . . . . .	73
5.3.1	Beam energy shift . . . . .	73
5.3.2	Tracking efficiency . . . . .	74
5.3.3	Momentum resolution . . . . .	74
5.3.4	Trigger . . . . .	74
5.3.5	MuonID . . . . .	84
5.4	Background systematics . . . . .	85
5.4.1	MuonID . . . . .	90
<b>6</b>	<b>Results</b>	<b>93</b>
6.1	Analysis results . . . . .	93
6.1.1	Data-MC side-band checks . . . . .	94
6.1.2	Data un-blinding . . . . .	95
6.2	Limit estimation . . . . .	95

<i>CONTENTS</i>	V
6.2.1 Upper limit settings implementation . . . . .	96
6.2.2 The Bayesian Analysis Toolkit . . . . .	96
6.3 Limit results . . . . .	97
<b>Conclusions and future prospects</b>	<b>99</b>
<b>Appendices</b>	<b>101</b>



# List of Figures

1.1	Summary table of the SM particles including mass, charge, spin and name information. Fermions are gathered in three different generations while bosons are classified depending on the force interaction carried. . . . .	4
1.2	Penguin diagrams for $\tau^\pm \rightarrow \mu^\pm \mu^\mp \mu^\pm$ in the SM. Neutrino oscillation is needed to conserve the leptonic flavour <sup>1</sup> . . . . .	9
1.3	Feynman diagrams for the $\tau^\pm \rightarrow \mu^\pm \mu^\mp \mu^\pm$ in the SUSY+seesaw model[1]. . . . .	11
1.4	Feynman diagrams for the $\tau^\pm \rightarrow \mu^\pm \mu^\mp \mu^\pm$ decay enhanced in the Littlest Higgs model with $T$ -parity[1]. . . . .	12
1.5	Feynman diagrams of $\tau^\pm \rightarrow \mu^\pm \mu^\mp \mu^\pm$ decay in the $R$ -parity violation model. Here the interaction is mediated by a sneutrino, the supersymmetric partner of the SM neutrino. [1]	13
1.6	Feynman diagrams of the $\tau^\pm \rightarrow \mu^\pm \mu^\mp \mu^\pm$ decay in the TC2 framework [1]. . . . .	14
1.7	Summary of the experimental measurements for several CLFV channels. The most sensitive $\tau \rightarrow \mu$ transition results come from BaBar (empty blue triangle shape) and Belle (full blue diamond shape) [2]. . . . .	14
1.8	Summary of the upper limits on BF for several LFV $\tau$ channels for the CLEO (pink), BaBar (blue), Belle (red) and LHCb (black) experiments, at 90% C.L. [3]. . . . .	15
1.9	Scheme of the difficulty in background rejection, at analysis level, for several LFV channels in $\tau$ sector. . . . .	16
2.1	SuperKEKB accelerator system, from the production of the beams to the collisions at the IP. . . . .	21
2.2	Schematic view of the nano-beam scheme adopted by <i>BelleII</i> . . . . .	22
2.3	Overview of the SuperKEKB and KEKB parameters [4],[5]. The comparison shows how the nano-beam scheme improves the luminosity. . . . .	22

2.4	Luminosity profile of the SuperKEKB collider. . . . .	23
2.5	3-D picture of the <i>BelleII</i> detector and its components. . . . .	25
2.6	Detailed view of the geometry and components of the <i>BelleII</i> detector. . . . .	26
2.7	Schematic view of the PXD (left) and SVD (right) detectors. . . . .	27
2.8	Design of a TOP quartz bar and propagation of the photons towards the MPC-PMTs. . . . .	29
2.9	Representation of the total internal reflection of Cherenkov photons produced by kaons and pions inside a TOP quartz bar. . . . .	29
2.10	Schematic view of the main components and the working principle of the ARICH detector. . . . .	30
2.11	KLM schematic composition. . . . .	32
2.12	KLM geometrical scheme. The angular acceptance of each sub-region is summarised at the bottom of the image. . . . .	33
2.13	KLM scintillator strip scheme. The read out system is displayed at the edge of the strip. . . . .	34
2.14	KLM RPC layer detailed composition. . . . .	34
2.15	Scheme of the working principle of the <i>BelleII</i> trigger system. . . . .	35
2.16	Schematic example of the event processing chain in BASF2. . . . .	37
3.1	Summary of muonID efficiencies and hadron-lepton mis-ID rates in a specific BKLM $\theta$ bin, for a threshold of 0.9. Note that the mis-ID rate was inflated by a factor 3 for illustration purposes. . . . .	40
3.2	Schematic view of the track extrapolation process from CDC towards KLM with matching and non-matching hits displayed. . . . .	41
3.3	Probability $\text{prob}_n$ dependence upon the barrel KLM layer number when a particle exits the BKLM. The muon (left) and pion (right) hypothesis cases are shown. . . . .	42
3.4	Probability $\text{prob}_n$ dependence upon the endcap KLM layer number when a particle exits the EKLM without crossing the BKLM. The muon (left) and pion (right) hypothesis cases are shown. . . . .	43
3.5	Probability $\text{prob}_n$ dependence upon the entire KLM layer number when a particle exits the EKLM, crossing the BKLM first. The muon (left) and pion (right) hypothesis cases are shown. . . . .	43
3.6	Reduced $\chi^2$ distributions for $\mu^+$ (left) and $\pi^+$ (right) for 4 (top) and 12 (bottom) d.o.f.. The red line is the fit to the upper tail of the histogram. . . . .	45

3.7	Momentum (left) and theta (right) distributions of the muons in the lab frame. The data/MC ratios are displayed on the bottom. . . . .	48
3.8	Data-MC agreement of the invariant mass distribution of the $\mu\mu$ system. . . . .	48
3.9	MuonID efficiency (left) and data-MC corrections (right) as a function of the momentum of tracks, for a specific BKLM region. Both plots refer to a muonID cut of 0.5. . . . .	49
3.10	MuonID efficiency (left) and data-MC corrections (right) as a function of the momentum of tracks, for a specific EKLM-BKLM separation region in the backward side. Both plots refer to a muonID cut of 0.5. . . . .	50
3.11	MuonID efficiency (left) and data-MC corrections (right) as a function of the momentum of tracks, for a specific EKLM region. Both plots refer to a muonID cut of 0.5. . . . .	50
3.12	Data and MC mis-ID rates comparison as a function of the momentum of tracks, relatively to a part of the BKLM region. The plot refers to the $\tau \rightarrow 3\pi\nu_\tau$ channel and a muonID cut of 0.5. . . . .	51
4.1	Event selection scheme overview. The two taus point to opposite directions: one is decaying into 3 muons and the other into 1prong. Tracks are coming from the IP region. . . .	56
4.2	$M_{3\mu}$ and $\Delta E_{3\mu}$ correlation plot. The correlation angle is extracted from the pol1 fit (blue line). . . . .	57
4.3	On the left, the $M_{3\mu}$ - $\Delta E_{3\mu}$ 2D plot is shown to underline the correlation. On the right, the same plot with de-correlated variables is reported. . . . .	58
4.4	On the left (right) the fit on $M_{3\mu}$ ( $\Delta E'_{3\mu}$ ) is reported. The 2 CB functions are in blue, the Gaussian in green and the total fit in red. The dashed pink lines represent the $3\sigma$ interval around the mean. The pulls are shown at the bottom of the plots, where the dashed red lines represent the boundaries at $\pm 2$ while the solid line indicates the null value. . . . .	59
4.5	$\Delta E'_{3\mu} - M'_{3\mu}$ scatter plot for signal (coloured points) and background (black dots) MC. . . . .	60
4.6	On the left (right) starting from the top there are the distributions of $M_{\tau_{tag}}$ , Thrust, $\Delta E_{\tau_{tag}}$ and $p_{miss}$ for the leptonic (hadronic) tag case. . . . .	61

4.7	On the left (right) starting from the top there are the distributions of $(\theta_{p_{miss}} - \theta_{\tau_{tag}})_{CMS}$ and $VisE^{CMS}$ for the leptonic (hadronic) tag case. . . . .	62
4.8	On the left (right) there is the distribution of $M_{miss}^2$ for the leptonic (hadronic) tag case. The dashed blue lines indicate the hand made cuts chosen. . . . .	66
4.9	On the left (right) starting from the top there are the distributions of p of the track in tag side, $p_{miss}$ , p of track1 in sig side and p of track2 in sig side for the leptonic (hadronic) tag case. The dashed blue lines indicate the hand made cuts chosen. . . . .	67
4.10	On the left (right) starting from the top there are the distributions of p of track3 in sig side, $n_\gamma$ tag side, $n_\gamma$ sig side and $n_{\pi^0}$ tag side for the leptonic (hadronic) tag case. The dashed blue lines indicate the hand made cuts chosen. . . . .	68
4.11	On the left (right) starting from the top there are the distributions of $n_{\pi^0}$ sig side, $(\theta_{p_{miss}} - \theta_{\tau_{tag}})_{CMS}$ , Thrust and $VisibleE_{CMS}$ for the leptonic (hadronic) tag case. The dashed blue lines indicate the hand made cuts chosen. . . . .	69
5.1	Trigger efficiencies of fff, ffo (left column) and hie, lml0, lml12 (right column) upon $\Delta E$ for the electron (top), muon (middle) and pion (bottom) tag track cases. . . . .	75
5.2	Trigger efficiency of fff as a function of $\Delta E$ . On top the electron case, on bottom left the muon case and on bottom right the pion case are displayed. . . . .	76
5.3	Trigger efficiency of lml0 as a function of $\Delta E$ . On top the electron, on bottom left the muon and on bottom right the pion tag cases are displayed. . . . .	77
5.4	Cluster energy deposition of muons (left) and pions (right) obtained from MC. The fit on the muon distribution is made with the sum of 2 gaussian functions and the total $\sigma$ is weighted with the integrals of each gaussian. . . . .	78
5.5	Trigger efficiency of lml0 as a function of $\Delta E$ , when the cluster energy of the 3 pions are the same as for muons. On top the electron case, on bottom left the muon case and on bottom right the pion case are displayed. . . . .	79
5.6	Trigger efficiency of cdcklm (left column) and $n_{cdcklm}$ (right column) for the $\tau^\pm \rightarrow \mu^\pm \mu^\mp \mu^\pm$ case. Electron (top), muon (middle) and pion (bottom) tag cases are displayed. . . . .	81

5.7	Trigger efficiency systematics of cdcklm event per event for the electron, muon and pion tag track cases. The mean value corresponds to the systematics uncertainty. . . . .	82
5.8	Final trigger efficiency selection for the $\tau^\pm \rightarrow \mu^\pm \mu^\mp \mu^\pm$ analysis. Electron (top), muon (left) and pion (right) tag cases are displayed. . . . .	83
5.9	Trigger efficiency systematics event by event for the electron (top), muon (middle left) and pion (middle right) tag track cases. The mean value corresponds to the systematics uncertainty. . . . .	84
5.10	Systematics gaussian including muonID efficiency systematics for each muon in the signal side. A double gaussian fit with the results are superimposed. . . . .	85
5.11	On the left (right) starting from the top there are the distributions of $\Delta E_{\tau_{tag}}$ , $\Delta E_{\tau_{sig}}$ and $M_{\tau_{tag}}$ for the leptonic (hadronic) tag case. . . . .	86
5.12	On the left (right) starting from the top there are the distributions of $M_{\tau_{sig}}$ , $M_{miss}^2$ , $p_{miss}$ and $(\theta_{p_{miss}} - \theta_{\tau_{tag}})_{CMS}$ for the leptonic (hadronic) tag case. . . . .	87
5.13	On the left (right) starting from the top there are the distributions of Thrust and VisibleEnergy <sub>CMS</sub> for the leptonic (hadronic) tag case. . . . .	88
5.14	Data-MC discrepancies extracted form several variables not weighted (top) and weighted (bottom) to the signal shape. A pol0 fit with the corresponding error is superimposed. . . . .	89
5.15	Systematics gaussian including muonID efficiency and misID systematics for each track in the signal side. The double gaussian fit result is superimposed. . . . .	91
6.1	Summary of the 90% CL upper limits for the BF of $\tau$ LFV decays obtained in the CLEO (purple boxes), BaBar (blue inverted triangles), Belle experiments (green triangles) and LHCb (yellow boxes). The red circles indicate the <i>BelleII</i> expectations, extrapolated from Belle results to an integrated luminosity of $50 \text{ ab}^{-1}$ . . . . .	95
6.2	Distribution of the limit value (S) provided by BAT. The 90% of the statistics is below $8.30 \cdot 10^{-8}$ . . . . .	97



# List of Tables

1.1	Summary table of the upper limits on the $\tau^\pm \rightarrow \mu^\pm \mu^\mp \mu^\pm$ BF for different NP theoretical frameworks. . . . .	10
2.1	Summary of the main production cross sections at <i>BelleII</i> . . .	24
3.1	Summary table of momentum and polar angle bins (together with the KLM sections) used to provide the muonID corrections.	46
4.1	Summary table of the intervals used during the optimisation procedure. . . . .	63
4.2	Initialisation value for Thrust, $M_{\tau_{tag}}$ and $\Delta E_{\tau_{tag}}$ used in the first optimisation step. . . . .	63
4.3	Cut values obtained with the optimisation procedure where r1 refers to tracks with $p < 0.7$ GeV, r2 to $0.7 \text{ GeV} < p < 1.0$ GeV and r3 to $p > 1$ GeV. The 4 sample used for the optimisations, from the top to the bottom, are defined as: 1 <sup>st</sup> sample from 0 to 2 $\text{ab}^{-1}$ , 2 <sup>nd</sup> sample from 1 to 3 $\text{ab}^{-1}$ , 3 <sup>rd</sup> sample from 2 to 4 $\text{ab}^{-1}$ , 4 <sup>th</sup> sample from 3 to 5 $\text{ab}^{-1}$ . Leptonic and hadronic tag cases are displayed as Lep and Had. . . . .	64
4.4	List of the hand made cuts to be applied to the data-sample. .	66
5.1	Summary of the trigger efficiency $\varepsilon$ results followed by the uncertainties which indicate the systematics. . . . .	79
5.2	Summary table of the signal systematic uncertainties. Electron, muon and pion tag cases are considered for the trigger systematics (el, mu and pi, respectively). The total uncertainty is reported at the bottom. . . . .	85

6.1	Results of efficiency and number of background events passing the optimised and additional hand made cuts. Binomial statistical error is added for the signal while a Poisson one is considered for the background as a reference, since it does not enter the limit computation. Results are given for the leptonic and hadronic tag cases. . . . .	94
6.2	Comparison between data and MC yields outside the signal region, between $10\sigma$ and $20\sigma$ . The statistical errors for the MC selection are showed. . . . .	94
6.3	Summary upper limit results for the $\tau^\pm \rightarrow \mu^\pm \mu^\mp \mu^\pm$ BF. Values are reported in terms of $10^{-8}$ . . . . .	98
4	Summary table of the data and MC efficiencies and the final correction values. Results are provided for $\mu\text{ID}>0.5$ and the uncertainties reported are statistical and systematical. . . . .	103
5	Summary table of the data and MC efficiencies and the final correction values. Results are provided for $\mu\text{ID}>0.9$ and the uncertainties reported are statistical and systematical. . . . .	105
6	Summary table of the data and MC efficiencies and the final correction values. Results are provided for $\mu\text{ID}>0.95$ and the uncertainties reported are statistical and systematical. . . . .	107

# Introduction

The standard model theory successfully describes the phenomenology of particles interactions in an extensive way. However, it has some limitations in explaining, for example, the neutrino mass ordering or their number of families. Therefore, new physics models are being investigated and the *BelleII* experiment, a second generation experiment at a B-factory, provides the perfect environment for precision measurements in the flavour sector. The violation of the leptonic flavour number is of much interest since it has very small probability to occur within the standard model framework. This effect is often enhanced in models beyond the standard model: current experiments, expected to rely on a large amount of data, have enough sensitivity to probe most of their parameter space. Lepton flavour violation studies, in the context of the  $\tau$  sector, are very interesting since  $\tau$  lepton is difficult to manage. Tau leptons can decay in a wide range of different final states: Lepton Flavour Violation (LFV) searches are mostly concentrated in signatures with electrons and muons. Golden channels are  $\tau^\pm \rightarrow l^\pm \gamma$  ( $l=e,\mu$ ) and the  $\tau^\pm \rightarrow \mu^\pm \mu^\mp \mu^\pm$ , which is the subject of this thesis. Its clear signal signature helps in the background reduction, which is composed mainly by  $q\bar{q}$  events. A new analysis method was studied for this thesis work, with particular care of the muon identification for the tracks coming from the LFV decaying  $\tau$  (signal  $\tau$ ). An extensive study of the identification performances was provided for an independent sample ( $e^+e^- \rightarrow \mu^+\mu^-\gamma$ ) in order to correctly take into account data-MC mismatches. In addition to the muon identification, several other variables were used to discriminate signal from background and an optimisation method based on the Punzi figure of merit maximisation was deployed. A crucial step is the identification of a signal region, based on  $\Delta E = E_{3\mu} - E_{\text{beam}}$  and  $M_{3\mu}$  variables, in which the optimisation process was carried out.

The signal efficiency and the number of the survived background events are computed after the application of the full set of cuts. These values, together with the number of observed data events inside the signal region,

were used as inputs for the upper limit estimation on the branching fraction of  $\tau^\pm \rightarrow \mu^\pm \mu^\mp \mu^\pm$ .

In Chapter 1 an overview of the physics motivations and the experimental status of the lepton flavour violation decays in the  $\tau$  sector, especially for the  $\tau^\pm \rightarrow \mu^\pm \mu^\mp \mu^\pm$  channel, is given. In Chapter 2 the *BelleII* experiment is described with particular focus on the  $K_L^0$  and  $\mu$  detector (KLM). Chapter 3 introduces the muon identification algorithm in *BelleII* and describes the analysis of the dimuon radiative channel, used to extract the data-MC correction factors of the muonID efficiency. In Chapter 4 the analysis steps and the optimisation procedure for the  $\tau^\pm \rightarrow \mu^\pm \mu^\mp \mu^\pm$  search are outlined, while Chapter 5 explains how the systematic effects affecting this measurement were performed. The final Chapter 6 provides the results of the analysis selection and the upper limit estimation.

# Chapter 1

## Physics motivations

The Standard Model (SM) is the theory that describes the fundamental particles and how they interact with each other. The main goal of the *BelleII* experiment is to perform precision measurements in the flavour sector and to explore the physics Beyond the SM (BSM) relying on a large amount of data. New Physics (NP) signals can be discovered in several fields of interest for *BelleII* including the  $\tau$  sector, in particular in the search of Lepton Flavour Violation (LFV) processes.

This chapter briefly describes the SM theoretical basis and the motivation for a LFV search in the  $\tau^\pm \rightarrow \mu^\pm \mu^\mp \mu^\pm$  channel. Ultimately, an overview of the experimental status of LFV searches is given.

### 1.1 Standard Model of particle physics

The SM predicts most of the phenomena governed by the electromagnetic, weak and strong forces. At present, it is our best understanding of the fundamental particles and their interactions. The SM is a unified gauge theory represented by direct product of the gauge groups  $SU(3)_c \times SU(2)_L \times U(1)_Y$  and its fundamental blocks are fermions, either quarks or leptons. Both occur in three generations and each of them includes two particles, as summarised in Fig. 1.1. For all the fermions a corresponding anti-fermion particle exists too.

Quarks, denoted as u, c and t (d, s and b), participate in strong interactions and have fractional electric charge  $2/3$  ( $-1/3$ ). They are identified by the *color*, an additional charge existing in the strong interaction theory (QCD). Quarks are not observed in nature as free particles, instead they form bound states called hadrons, which are composed either of three quarks (baryons) or a pair of quark and anti-quark

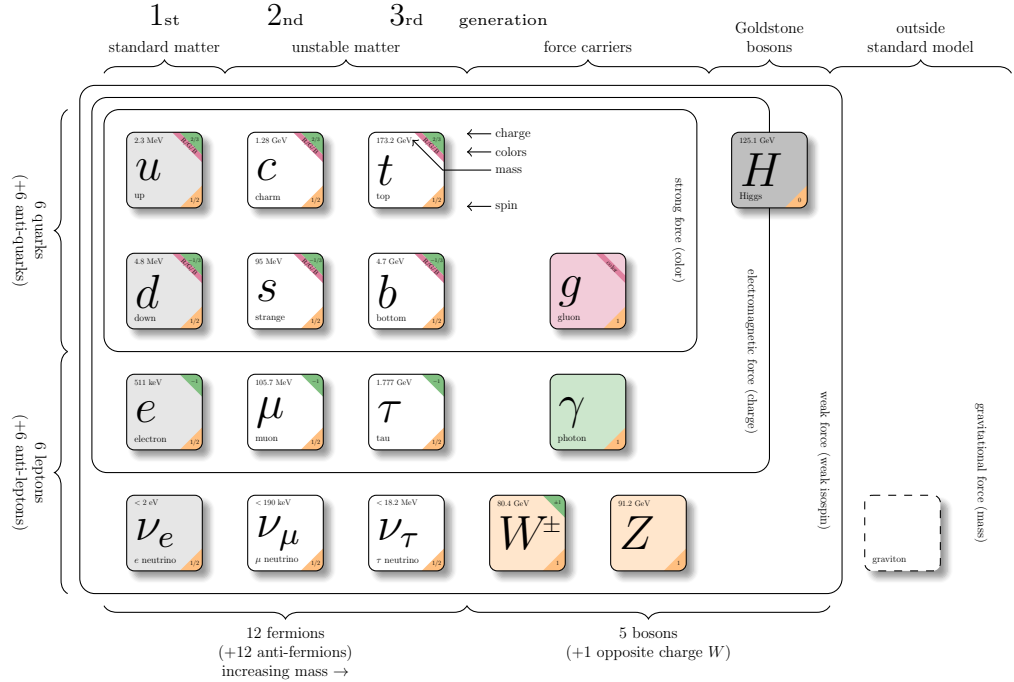


Figure 1.1: Summary table of the SM particles including mass, charge, spin and name information. Fermions are gathered in three different generations while bosons are classified depending on the force interaction carried.

(mesons). Mesons and baryons are colorless objects [6],[7].

Leptons do not interact via strong interactions and each generation is composed of a charged and a neutral fermion: the electron ( $e$ ) and electron neutrino ( $\nu_e$ ), the muon ( $\mu$ ) and the muon neutrino ( $\nu_\mu$ ), the tau ( $\tau$ ) and the tau neutrino ( $\nu_\tau$ ). Each lepton is tagged with a leptonic quantum number  $L$  that is defined as  $+1$  for leptons,  $-1$  for anti-leptons and  $0$  for non-leptonic particles. In addition, three more leptonic numbers  $L_f$  were introduced and assigned to each generation of leptons, where  $f = e, \mu, \tau$  identifies the flavour. In this way, the lepton number counts all the leptons involved in a process, while the lepton flavour is restricted to each generation separately. Therefore lepton flavour violation does not imply lepton number violation.

The interaction between SM particles is mediated by the exchange of force carrier bosons (see Fig.1.1): the photon ( $\gamma$ ) together with  $W^\pm$  and  $Z$  for the electroweak interactions (included in the  $SU(2)_L \times U(1)_Y$  group), 8 gluons for the strong interaction (coupled with the color charge  $c$ ) and the Higgs boson, providing the mass to the particles via the spontaneous

symmetry breaking mechanism [8]. The complex scalar field of the Higgs boson has non-zero vacuum expectation value, which induces the generation of the SM particle masses.

The SM interactions and particles are described by the following Lagrangian, in a renormalisable form:

$$\mathcal{L}_{SM} = \mathcal{L}_{kin} + \mathcal{L}_{EW} + \mathcal{L}_{QCD} + \mathcal{L}_{Higgs} + \mathcal{L}_{Yuk} \quad (1.1)$$

The kinetic term  $\mathcal{L}_{kin}$  includes the gauge bosons self interactions,  $\mathcal{L}_{EW}$  represents the electroweak theory,  $\mathcal{L}_{QCD}$  describes how quarks and gluons interact in QCD,  $\mathcal{L}_{Higgs}$  contains the self-interaction of the Higgs and how it interacts with the SM bosons while  $\mathcal{L}_{Yuk}$  involves the interaction of the Higgs with the SM fermions.

The mass matrix term arising from the interaction of quarks with the Higgs field does not coincide with the flavour ones. The so called Cabibbo-Kobayashi-Maskawa (CKM) matrix was introduced (see Eq. 1.2) to transform the mass to the flavour eigenstates.

$$\hat{V}_{CKM} = \begin{pmatrix} V_{ud} & V_{us} & V_{ub} \\ V_{cd} & V_{cs} & V_{cb} \\ V_{td} & V_{ts} & V_{tb} \end{pmatrix} \quad (1.2)$$

It describes the charged current transitions of the u, c, t quarks to d, s, b and each matrix element represents the amplitude of a particular transition. The CKM matrix can be parametrised by three Euler angles and one irreducible complex phase, which opens to the possibility of the Charge and Parity (CP) symmetry violation. Using a specific parametrisation of the CKM matrix (the Wolfenstein one [9], which is also the most common), the diagonal terms of the matrix are shown to be close to 1, while the off diagonal ones scale down following the power of  $\sin \theta_C$ , which is the Cabibbo angle<sup>1</sup> [10]. The transitions between quarks belonging to the same generation are Cabibbo favoured, while the others are Cabibbo suppressed or double-Cabibbo suppressed.

Although the SM is extremely successful in describing the experimental results, it can not explain several phenomena such as the hierarchy problem (about the number of fermion families and their mass differences), the baryon asymmetry in the universe (excess of baryonic matter over antimatter), the existence of the dark matter and energy, the neutrino

---

<sup>1</sup>From experimental measurements, the sine of the Cabibbo angle is estimated to be  $\sin \theta \simeq 0.23$ , explaining the quark mixing phenomenon in the simplified scenario of two families.

oscillations and their masses.

The *BelleII* experiment aims at performing precision measurements in the flavour sector and to search for the physics BSM. In the context of a B-factory, the  $\tau$  physics is a promising sector where a NP signal can be discovered, since a large and background-clean data-set can be collected.

### 1.1.1 Neutrino oscillation phenomenon

The neutrino oscillation was predicted by Bruno Pontecorvo in 1957 and experimentally observed for four different sources: solar[11], atmospheric[12], accelerator[13] and reactor[14]. Analogously to the quark sector, the neutrino weak interaction (flavour) eigenstates  $\nu_e, \nu_\mu, \nu_\tau$  do not coincide with mass ones  $\nu_1, \nu_2, \nu_3$ . The former can be expressed in terms of the latter through a rotation defined by the unitary matrix PMNS (Pontecorvo, Maki, Nakagawa and Sakata) [15], that provides the amplitude of each transformation:

$$\begin{pmatrix} \nu_e \\ \nu_\mu \\ \nu_\tau \end{pmatrix} = \underbrace{\begin{pmatrix} U_{e1} & U_{e2} & U_{e3} \\ U_{\mu1} & U_{\mu2} & U_{\mu3} \\ U_{\tau1} & U_{\tau2} & U_{\tau3} \end{pmatrix}}_{PMNS \text{ matrix}} \cdot \begin{pmatrix} \nu_1 \\ \nu_2 \\ \nu_3 \end{pmatrix} \quad (1.3)$$

Using a specific parameterization, the PMNS matrix can be expressed as:

$$\begin{aligned} U &= \begin{pmatrix} c_{12}c_{13} & s_{12}c_{13} & s_{13}e^{-i\delta} \\ -s_{12}c_{23} - c_{12}s_{23}s_{13}e^{i\delta} & c_{12}c_{23} - s_{12}s_{23}s_{13}e^{i\delta} & s_{23}c_{13} \\ s_{12}s_{23} - c_{12}c_{23}s_{13}e^{i\delta} & -c_{12}s_{23} - s_{12}c_{23}s_{13}e^{i\delta} & c_{23}c_{13} \end{pmatrix} \cdot \\ &\cdot \begin{pmatrix} 1 & 0 & 0 \\ 0 & e^{i\alpha_2/2} & 0 \\ 0 & 0 & e^{i\alpha_3/2} \end{pmatrix} = \\ &= \begin{pmatrix} 1 & 0 & 0 \\ 0 & c_{23} & s_{23} \\ 0 & -s_{23} & c_{23} \end{pmatrix} \begin{pmatrix} c_{13} & 0 & s_{13}e^{-i\delta} \\ 0 & 1 & 0 \\ -s_{13}e^{-i\delta} & 0 & c_{13} \end{pmatrix} \begin{pmatrix} c_{12} & s_{12} & 0 \\ -s_{12} & c_{12} & 0 \\ 0 & 0 & 1 \end{pmatrix} \cdot \\ &\cdot \begin{pmatrix} 1 & 0 & 0 \\ 0 & e^{i\alpha_2/2} & 0 \\ 0 & 0 & e^{i\alpha_3/2} \end{pmatrix}, \quad c_{ij} = \cos \theta_{ij} \quad , \quad s_{ij} = \sin \theta_{ij} \quad (1.4) \end{aligned}$$

The PMNS matrix is parametrised in terms of the three Euler rotation angles ( $\theta_{12}$ ,  $\theta_{23}$  and  $\theta_{13}$ ) and a complex phase ( $\delta$ ) but in case  $\nu = \bar{\nu}$  (Majorana neutrinos) two additional phases have to be added ( $\alpha_2$  and  $\alpha_3$ ). As of today, there are no experimental measurements that can distinguish between the Dirac or Majorana nature of neutrinos. The current best estimate for the PMNS matrix elements [16], within a  $3\sigma$  interval, are shown below:

$$|U_{3\sigma}| = \begin{pmatrix} 0.801 \rightarrow 0.845 & 0.513 \rightarrow 0.579 & 0.143 \rightarrow 0.156 \\ 0.233 \rightarrow 0.507 & 0.461 \rightarrow 0.694 & 0.631 \rightarrow 0.778 \\ 0.261 \rightarrow 0.526 & 0.471 \rightarrow 0.701 & 0.611 \rightarrow 0.761 \end{pmatrix} \quad (1.5)$$

The time evolution of a neutrino can be described by the following relation, using the mass eigenstates:

$$|\nu_i(t)\rangle = e^{-i(E_i t - \vec{p}_i \cdot \vec{x})} |\nu_i(0)\rangle \quad (1.6)$$

where  $i$  identify the neutrino family,  $E_i$  is the corresponding energy,  $\vec{p}_i$  is the three-dimensional momentum vector and  $\vec{x}$  is the position vector. Assuming that  $|\vec{p}_i| = p_i \gg m_i$  and  $p_i \simeq E_i \equiv E$ , the neutrino energy  $E_i$  can be written as:

$$E_i = \sqrt{p_i^2 + m_i^2} \simeq p_i + \frac{m_i^2}{2p_i} \approx E + \frac{m_i^2}{2E} \quad (1.7)$$

and the neutrino wave function would become:

$$|\nu_i(t \simeq L)\rangle = e^{-im_i^2 \frac{L}{2E}} |\nu_i(0)\rangle \quad (1.8)$$

where no phase factor was considered and  $t \simeq L$  is assumed (relativistic neutrino condition with  $c = 1$ ). Then the oscillation phenomenon from flavour  $\alpha$  to  $\beta$  is expressed as:

$$P(\nu_\alpha \rightarrow \nu_\beta) = |\langle \nu_\beta | \nu_\alpha(t) \rangle|^2 = \left| \sum_i U_{\alpha i}^* U_{\beta i} e^{-im_i^2 \frac{L}{2E}} \right|^2 \quad (1.9)$$

This formulation can be simplified, for a two-flavour scheme for which  $U$  is a 2x2 rotation matrix, with the following probability expression:

$$P(\nu_\alpha \rightarrow \nu_\beta) = \sin^2(2\theta) \cdot \sin^2 \left( 1.27 \cdot \frac{\Delta m_{ij}^2 [eV^2]}{E [MeV]} L [m] \right) \quad (1.10)$$

where  $\theta$  is the mixing angle between the two flavour considered,  $L$  is the distance between the point of production and detection of neutrinos, while  $\Delta m_{ij} = m_i - m_j$  is the mass difference of the two neutrinos involved in the oscillation phenomenon. The oscillation length  $L^{osc}$  can be derived from Eq.1.10 to be:

$$L^{osc} = \frac{4\pi E}{\Delta m_{ij}^2} \quad (1.11)$$

In order to be sensitive to a specific  $\Delta m_{ij}^2$  the experiments have to be made with  $E/L \simeq \Delta m_{ij}^2$ . In fact, having  $E/L \gg \Delta m_{ij}^2$  means that there is not enough time for the oscillation to occur, since  $\sin^2 x_{ij} \ll 1$ . Instead, if  $E/L \ll \Delta m_{ij}^2$  the oscillating phase is averaged to  $\langle \sin^2 \theta_{ij} \rangle = 1/2$ , making the effect not visible. The observation of the oscillation implies that the mixing phenomenon occurs ( $\theta \neq 0$ ) and the neutrino mass differences is different from zero, meaning that at least two out of three neutrino families are massive.

The experimental measurements of the mass differences in the three-flavour scheme, performed for different  $E/L$  ratios and from different sources [9], give the following results:

$$\begin{aligned} \Delta m_{21}^2 &= 7.39_{-0.20}^{+0.21} \cdot 10^{-5} eV^2 \\ |\Delta m_{32}^2| &= 2.449_{-0.03}^{+0.032} \cdot 10^{-3} eV^2 \end{aligned} \quad (1.12)$$

Note that the uncertainties on these measurements are large but were improved a lot in the past years (see [16] for more details).

### 1.1.2 Charged Lepton Flavour Violation

Leptonic mixing and massive neutrinos play a crucial role in the searches of NP signals among many sectors like the Charged Lepton Flavour Violation (CLFV): it describes the transitions between  $e$ ,  $\mu$  and  $\tau$  that do not conserve the lepton family number. There are several extensions of the SM that take into account such processes and the most minimal one consists in the addition of right-handed neutrinos, so that lepton number is conserved. With these considerations, individual lepton numbers are violated and accounted by the PMNS matrix, while CLFV transitions like  $\tau^\pm \rightarrow \mu^\pm \mu^\mp \mu^\pm$  can occur. However, the decay rates are predicted to be very small and far away from the experimental sensitivities. Therefore, the observation of a CLFV process would imply the existence of NP.

This section introduces the theoretical mechanisms and motivations for the CLFV search for the  $\tau^\pm \rightarrow \mu^\pm \mu^\mp \mu^\pm$  decay.

### 1.1.2.1 $\tau^\pm \rightarrow \mu^\pm \mu^\mp \mu^\pm$ in the Standard Model

The neutral lepton flavour violation is already observed within the SM in the neutrino oscillation, implying that it has to occur in the charged sector as well. In the SM, the majority of the CLFV processes, such as  $\mu \rightarrow e\gamma$ ,  $\tau \rightarrow 3l$ ,  $\mu \rightarrow 3e$ , involve loops, as shown in Fig. 1.2 for the  $\tau^\pm \rightarrow \mu^\pm \mu^\mp \mu^\pm$  case. The oscillation of the neutrinos within the decay vertex dimension has a very tiny probability to occur, making the Branching Fractions (BF) of these processes very small.

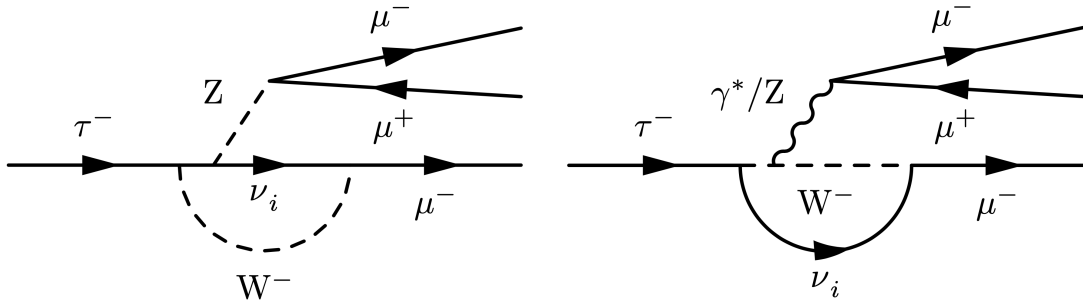


Figure 1.2: Penguin diagrams for  $\tau^\pm \rightarrow \mu^\pm \mu^\mp \mu^\pm$  in the SM. Neutrino oscillation is needed to conserve the leptonic flavour <sup>3</sup>.

The amplitude of each penguin diagrams is proportional to the PMNS matrix elements product  $U_{\tau,i}U_{\mu,i}^*$  and has a kinematic dependence expressed as:

$$f\left(\frac{m_{\nu_i}}{m_W}\right) = 1 + c \cdot \frac{m_{\nu_i}^2}{m_W^2} \quad (1.13)$$

where  $c$  is the expansion factor,  $m_{\nu_i}^2$  is the neutrino square mass differences and  $m_W^2$  is the W boson squared mass. The sum over all neutrino generations gives the following estimate of the amplitude (A) [17]:

$$\begin{aligned} A &\propto \sum_{i=1}^3 U_{\tau,i}U_{\mu,i}^* \left(1 + c \cdot \frac{m_{\nu_i}^2}{m_W^2}\right) \\ &= \sum_{i=1}^3 U_{\tau,i}U_{\mu,i}^* + \sum_{i=1}^3 (U_{\tau,i}U_{\mu,i}^*) \left(1 + c \cdot \frac{m_{\nu_i}^2}{m_W^2}\right) < 10^{-54} \quad (1.14) \end{aligned}$$

The first sum is null due to the unitarity of the PMNS matrix while the second one is suppressed due to the mass ratio, even if the order of magnitude of

<sup>3</sup>Note that the neutrino mass eigenstates  $\nu_i$  do not oscillate, but the interference of diagrams with different mass eigenstates produces the  $\nu_\tau \rightarrow \nu_\mu$  flavour oscillation.

the  $U$  matrix elements is the unit. The very small value of  $A$  prevents any observation of CLFV given the achievable existing experimental sensitivities, unless phenomena BSM occur.

### 1.1.2.2 $\tau^\pm \rightarrow \mu^\pm \mu^\mp \mu^\pm$ in New Physics Model

The possibility of the existence of CLFV comes from the introduction of new theoretical frameworks that could explain the limitations of the SM. Measuring an upper limit on the BF of several decays can constraint the parameter space of the NP models, or even exclude them completely. On the other hand, the observation of a CLFV signal would prove the existence of a new effect.

It is preferable to search for a CLFV process in the third lepton generation instead of in the other two, lighter generations, due to the mass dependence of several NP model couplings. Moreover, differently from the  $\mu$  and the  $e$ , the  $\tau$  lepton can decay to both quarks and leptons giving the possibility to access a larger number of decay modes, that can be enhanced by NP models and studied experimentally.

The prediction of several models BSM can be investigated by the current and future experiment sensitivities, such as *BelleII*. Some of the models are based on the Supersymmetry (SUSY)[18] which introduces a symmetry between bosons and fermions. The Minimal Supersymmetric Standard Model (MSSM) includes the SUSY and contains both the SM particles and their supersymmetric partners.

In Tab. 1.1 a summary of the NP model predictions is reported. For more details on the theoretical frameworks see [1].

Table 1.1: Summary table of the upper limits on the  $\tau^\pm \rightarrow \mu^\pm \mu^\mp \mu^\pm$  BF for different NP theoretical frameworks.

NP model	BF limit for $\tau^\pm \rightarrow \mu^\pm \mu^\mp \mu^\pm$
Littlest Higgs with T-parity[19]	$10^{-8}$
R-parity violating SUSY[20]	$10^{-8}$
Non-universal $Z'$ [21]	$10^{-8}$
MSSM + seesaw[22][23]	$10^{-9}$
SUSY SO(10)[24]	$10^{-10}$
SUSY Higgs[25]	$10^{-10}$
SM + heavy Majorana $\nu$ [26]	$10^{-10}$

In the following, a brief explanation of the models with the highest BF predictions is given.

**1.1.2.2.1 MSSM + seesaw** The SM does not explain the differences between the masses of neutrinos and charged leptons, generated by the couplings with the Higgs field. The "seesaw mechanism" gives an explanation for the relative sizes of the neutrino masses in the SM by the introduction of additional right-handed sterile neutrinos ( $\tilde{\chi}$ ), assumed to be Majorana particles with masses of the order of 1 TeV. Together with the sterile neutrinos also new boson mediators  $W'$  and  $Z'$  are introduced and used in the MSSM to give mass to sterile neutrinos.

An example of the Feynman diagram that contributes to the  $\tau^\pm \rightarrow \mu^\pm \mu^\mp \mu^\pm$  channel is shown in Fig.1.3, where H and A represent additional Higgs introduced in the MSSM while  $\tilde{\nu}$  ( $\tilde{l}$ ) is the supersymmetric partner of the neutrinos (leptons) provided by the SUSY theory.

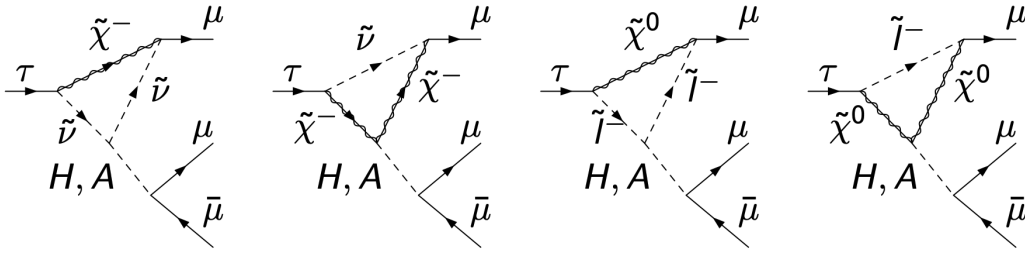


Figure 1.3: Feynman diagrams for the  $\tau^\pm \rightarrow \mu^\pm \mu^\mp \mu^\pm$  in the SUSY+seesaw model[1].

Considering the MSSM+seesaw model validity, a prediction of the branching ratio of the  $\tau^\pm \rightarrow \mu^\pm \mu^\mp \mu^\pm$  decay, for specific assumptions on the parameters of the model, is:

$$BF(\tau \rightarrow \mu\mu\mu) \simeq 10^{-7} \left( \frac{\tan\beta}{60} \right)^6 \times \left( \frac{100\text{GeV}}{m_A} \right)^4 \quad (1.15)$$

where  $m_A$  is the mass of a new Higgs introduced by the MSSM, while  $\beta$  is defined as the ratio between the two Higgs vacuum expectation values  $v_H/v_A$ . A detailed description of the calculations that lead to this estimation is available at [23].

**1.1.2.2.2 Littlest Higgs with  $T$ -parity** Little Higgs (LH) models are recently proposed as a solution to the "Little Hierarchy problem"<sup>4</sup> by causing the electroweak symmetry breaking and introducing new particles such as  $W_H$  and  $Z_H$  mediators and the heavy neutrino  $\nu_H$ . These models require also that the SM Higgs boson is a pseudo-Goldstone boson[29][30], preventing quadratic divergent contributions at one-loop level. If these corrections appear in tow-loop diagrams, a Higgs mass of  $\sim 10$  TeV is expected and some fine-tuning of the framework is needed[31]. A  $T$ -parity symmetry[19] can be added to this framework at the TeV scale, seeking to act only on the new particles and leaving the tree-level corrections untouched. This symmetry is needed to avoid problems related to the anomalous coupling introduced by the additional particles. Therefore, tree level contributions are forbidden by the model, but additional loop diagrams for  $T$ -odd particles are allowed. In Fig. 1.4 examples of the Feynman diagrams are displayed.

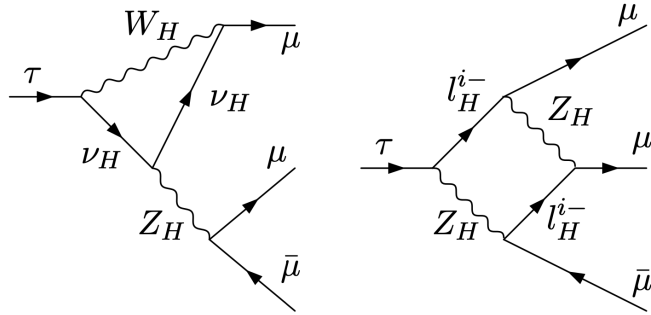


Figure 1.4: Feynman diagrams for the  $\tau^\pm \rightarrow \mu^\pm \mu^\mp \mu^\pm$  decay enhanced in the Littlest Higgs model with  $T$ -parity[1].

**1.1.2.2.3  $R$ -parity violating SUSY** With the introduction of additional particles and interactions provided by the SUSY, the baryon number and the lepton number can be violated<sup>5</sup>. The  $R$ -parity is a discrete symmetry introduced to avoid having those violations occurring within the SUSY theoretical framework.

<sup>4</sup>Several models BSM attempt to explain the reason for the GeV scale attributed to the Higgs boson mass, with the addition of new particles at the TeV scale [27]. Precision measurements found no NP evidence for masses below 7 TeV[28]. This produced the so-called "Little Hierarchy problem".

<sup>5</sup>Experimentally, the conservation of these quantities was tested to high levels of precision thus theory usually do not want to accept such violations.

$R$ -parity variable ( $R_p$ ) is +1 for SM particles ( $R$ -even) and -1 for the SUSY ones ( $R$ -odd) and it is defined as:

$$R = 3B + L + 2S \quad (1.16)$$

where  $B$  is the baryon number,  $L$  the lepton number and  $S$  the spin. The  $R$ -parity conservation assures the stability of the lightest supersymmetric particle of the model: it also allows to have a good dark matter candidate but it can be violated in several cases[20]. In such violation contexts, the  $\tau^\pm \rightarrow \mu^\pm \mu^\mp \mu^\pm$  decay can be mediated by the exchange of a  $\tilde{\nu}$ , as shown in Fig. 1.5.

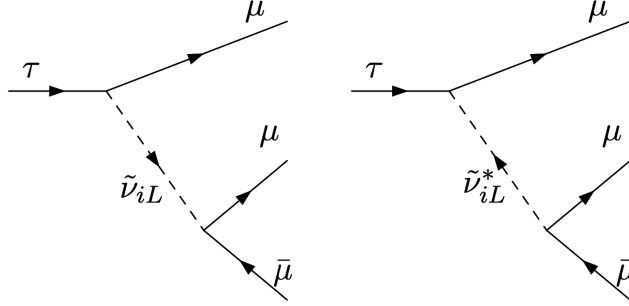


Figure 1.5: Feynman diagrams of  $\tau^\pm \rightarrow \mu^\pm \mu^\mp \mu^\pm$  decay in the  $R$ -parity violation model. Here the interaction is mediated by a sneutrino, the supersymmetric partner of the SM neutrino. [1]

**1.1.2.2.4 Non-universal  $Z'$**  The existence of an extra gauge boson  $Z'$  is introduced in several extensions of the SM and it is a good candidate to explain some tensions observed in the quark sector. The Topcolor-assisted technicolor (TC2) model [21] introduces a new set of particles including the top-pion  $\pi_t$  [32] and a non-universal  $Z'$  boson, that can give significant contributions to Flavour Changing Neutral Currents (FCNC) processes. Typically, these models predict large couplings to the third generation leptons that are mediated by the  $Z'$ . The Feynman diagrams allowed by those models, contributing to  $\tau^\pm \rightarrow \mu^\pm \mu^\mp \mu^\pm$ , are displayed in Fig. 1.6. Here, two extreme cases, where either one of the two particles between  $Z'$  and  $\pi_t$  dominates the decay, are considered.

The predicted BF is proportional to  $m_{Z'}^4$ , and, for a mass of 1 TeV, the upper limit on the  $\tau^\pm \rightarrow \mu^\pm \mu^\mp \mu^\pm$  BF is  $4 \cdot 10^{-8}$ .

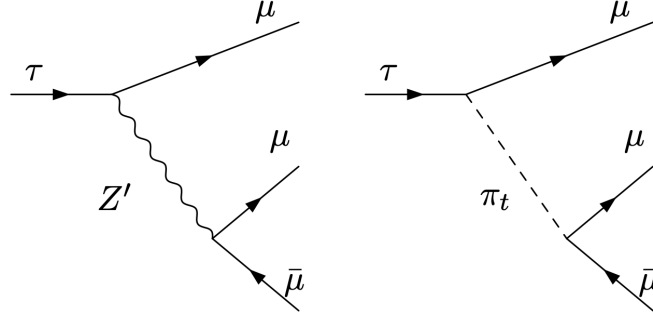


Figure 1.6: Feynman diagrams of the  $\tau^\pm \rightarrow \mu^\pm \mu^\mp \mu^\pm$  decay in the TC2 framework [1].

## 1.2 Experimental status of Lepton Flavour Violation in $\tau \rightarrow \mu$ transitions

Several experiments searched for CLFV decays but, so far, there are no experimental evidences. In Fig. 1.7 a history graph of the experimental limits, measured by the main experiments of the past [33], shows that the first studies started in the '50s.

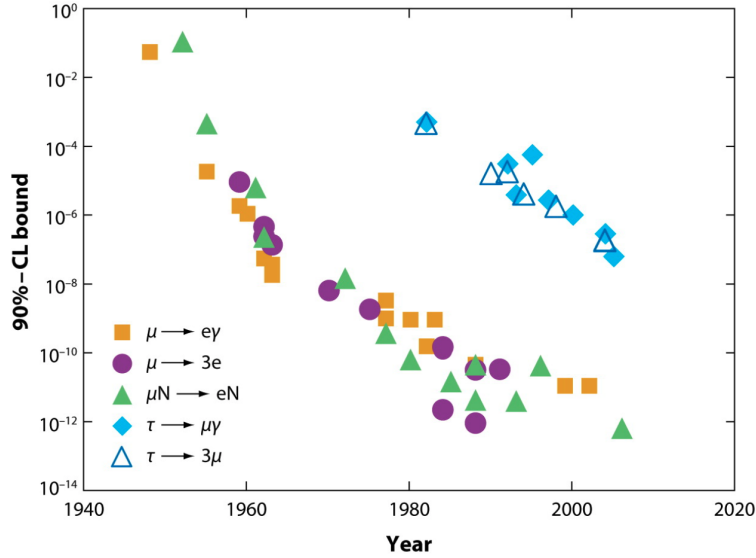


Figure 1.7: Summary of the experimental measurements for several CLFV channels. The most sensitive  $\tau \rightarrow \mu$  transition results come from BaBar (empty blue triangle shape) and Belle (full blue diamond shape) [2].

The experiments that investigated the  $\mu \rightarrow e$  transitions were made for that purpose only and managed to probe BF values down to  $\sim 10^{-14}$ , due to very clean environments. For the  $\tau \rightarrow \mu$  transitions there is no dedicated experiment since taus are very difficult to manage due to their very small lifetime:  $2.9 \cdot 10^{-13}$  s. Moreover, the  $\tau$  lepton is the only one that can decay hadronically, making the reconstruction process harder with respect to the lighter leptons. For this reasons, large experiments, like the ones at the B-factories, are the most indicated to perform CLFV measurements in the  $\tau$  sector.

In Fig. 1.8 the limits on the BF of many decay channels are reported for several experiments, showing that the  $e^+e^-$  colliders are the most suitable for this purpose.

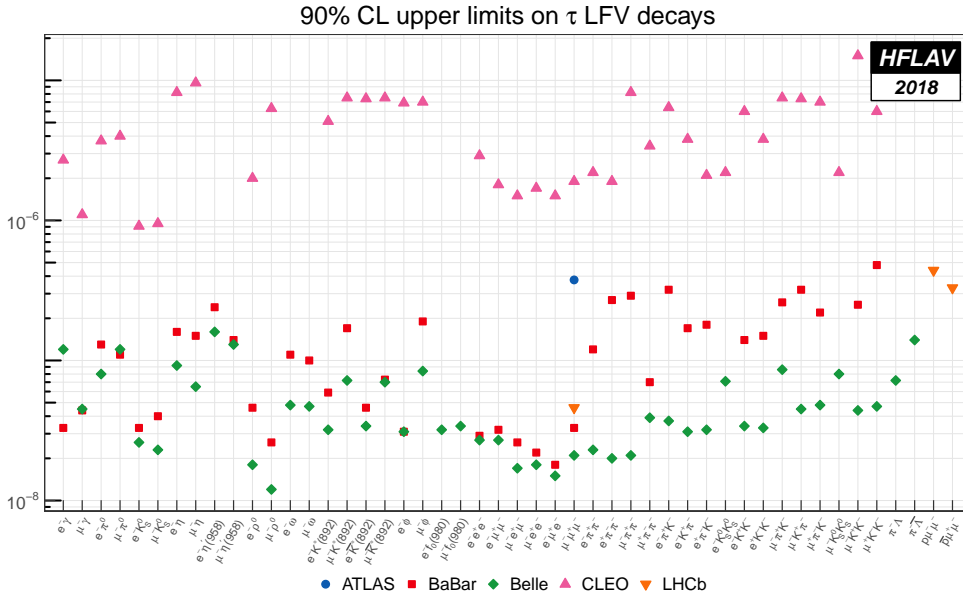


Figure 1.8: Summary of the upper limits on BF for several LFV  $\tau$  channels for the CLEO (pink), BaBar (blue), Belle (red) and LHCb (black) experiments, at 90% C.L. [3].

The best results are achieved at the Belle and BaBar experiments that relied on a data-set corresponding to  $782 \text{ fb}^{-1}$  and  $486 \text{ fb}^{-1}$ , respectively. Focusing on the  $\tau^\pm \rightarrow \mu^\pm \mu^\mp \mu^\pm$  decay channel, they measured an upper limit on the BF at 90% C.L. of:

$$\text{BaBar}[34] : BF(\tau^\pm \rightarrow \mu^\pm \mu^\mp \mu^\pm) < 3.3 \cdot 10^{-8} \quad (1.17)$$

$$\text{Belle}[35] : BF(\tau^\pm \rightarrow \mu^\pm \mu^\mp \mu^\pm) < 2.1 \cdot 10^{-8} \quad (1.18)$$

These limits were extracted considering a signal efficiency of 6.6% and 7.6% with 0 observed events. These results will be compared with the outcome of

the work discussed in this thesis. In the specific case of the  $\tau^\pm \rightarrow \mu^\pm \mu^\mp \mu^\pm$  decay, the LHCb experiment provided a result[36] comparable with the best estimates. The presence of three muons in the final state allow the well performing LHCb trigger system to reject the major sources of backgrounds. Moreover, having three charged tracks coming from the same  $\tau$ , together with a large CMS boost, give major advantages to this specific search, unlike for the other analyses.

### 1.2.1 Experimental challenges and advantages for the $\tau^\pm \rightarrow \mu^\pm \mu^\mp \mu^\pm$ search at *BelleII*

Experiments at the B-factories like *BelleII* have large advantages in  $\tau$  searches (see Chap. 2 Sec. 2.1.2). In particular for the  $\tau^\pm \rightarrow \mu^\pm \mu^\mp \mu^\pm$  case, the well defined energy of the initial state can be exploited to measure the mass and the energy of the taus in an accurate way. This is a crucial aspect in the selection of such a decay since the absence of missing energy, differently from any other SM  $\tau$  processes, helps in having a clear signature. Moreover, the background "free" environment provided by the B-factory allows to reconstruct almost all particles in the events in an efficient way. In addition, having very few SM processes that can mimic the NP one is favouring this decay signature on the other ones. For this reason the  $\tau^\pm \rightarrow \mu^\pm \mu^\mp \mu^\pm$ , together with  $\tau^\pm \rightarrow \mu^\pm \gamma$ , is considered a LFV  $\tau$  golden channel although the BF estimations are smaller. In Fig. 1.9 a scheme indicating the background rejection difficulties is shown for several channels.

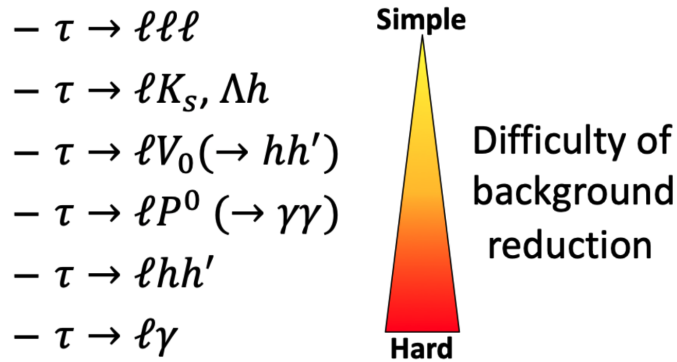


Figure 1.9: Scheme of the difficulty in background rejection, at analysis level, for several LFV channels in  $\tau$  sector.

The disadvantage of having three muons in the final state concerns the

large contributions of  $\mu \rightarrow \pi$  mis-identification rate that is an almost irreducible source (see Chap. 3, Sec.3.3 for more details). This problem can be partially overcome with a well performing muon identification system.



# Chapter 2

## The *BelleII* experiment

The *BelleII* experiment [37] represents the first experiment of a new generation. It operates at the  $e^+e^-$  collider SuperKEKB in Tsukuba (Japan) at the KEK laboratory. *BelleII* and SuperKEKB are upgrades of the Belle experiment and the KEKB accelerator, which ran from 1999 to 2010. The SuperKEKB accelerator is planned to reach an instantaneous luminosity of  $\mathcal{L} \simeq 6 \cdot 10^{35} \text{cm}^{-2} \text{s}^{-1}$  (recently updated value), about 50 times more than KEKB. This large improvement will be accomplished not only increasing the circulating currents, but also employing the nano-beam scheme, which was initially proposed for the SuperB project by P.Raimondi [38], [39]. While the goal of the first generation B-factories (Belle at KEKB, KEK and BaBar at PEP-II, SLAC) was the discovery of CP violation in the B mesons and the measurement of the unitarity triangle parameters, the *BelleII* main focus is the investigation of physics BSM via the precise measurement of SM parameters like CP asymmetries, as well as the observation of rare or forbidden decays.

In this chapter, a description of the accelerator machine and detector components is given. Additional information can be found in [37], [40].

### 2.1 The accelerator SuperKEKB

The SuperKEKB is the accelerator machine with the highest instantaneous luminosity ever built. It was thought specifically for the *BelleII* experiment and is placed in the same tunnel of its predecessor KEKB. SuperKEKB uses asymmetric  $e^+$  and  $e^-$  beams of, respectively, 4 GeV and 7 GeV of energy. It operates at a Center of Mass (CM) energy of  $10.58 \text{ GeV}/c^2$ , just at the  $\Upsilon(4S)$  mass resonance. The energy asymmetry of the beams results in a Lorentz boost of the laboratory system with respect to the center of mass system of

$\Upsilon(4S)$ . This boost is represented by a  $\beta\gamma$  factor of:

$$\beta\gamma = \frac{P_{e^-} - P_{e^+}}{\sqrt{s}} \simeq \frac{E_{e^-} - E_{e^+}}{\sqrt{4E_{e^+}E_{e^-}}} \simeq 0.28 . \quad (2.1)$$

The CM boost allows to amplify and resolve the decay vertex positions of the B mesons coming from  $\Upsilon(4S)$ . Considering the *BelleII* boost, the flight distance of the B mesons is  $\sim 130 \mu\text{m}$  that can be resolved with the high resolution achieved by the *BelleII* vertex detectors. The boost was reduced with respect to the one used in KEKB ( $\beta\gamma=0.42$ ) in order to cope with the increase of instantaneous luminosity.

The electron beam of SuperKEKB is produced in the pre-injector accelerator through the interaction of a pulsed laser with a cathode. Then electrons are accelerated with a linear accelerator (Linac) up to 7 GeV. A part of these electrons are used to produce positrons through the interaction with a tungsten target located in the middle of the Linac accelerator. These  $e^+$  are injected into a Damping Ring (DR) in order to reduce the beam emittance to the level needed for high luminosity operations. After this process, positrons are accelerated using the remaining half part of the Linac, up to 4 GeV. At the final acceleration stage, electrons are injected into the High Energy Ring (HER) while positrons into the Low Energy Ring (LER). The collisions take place at a specified Interaction Point (IP) or Interaction Region (IR). A schematic view of the acceleration processes is shown in figure 2.1.

The beams are not perfectly head-on, in fact they have a crossing angle of  $2\phi = 83 \text{ mrad}$ , which is about 4 times larger than KEKB. This value is chosen mainly by considerations related to the optics of the beams: with a large crossing angle, the final focus quadrupole magnets can be independent for the two beams and they can be placed closer to the IP.

SuperKEKB successfully operated since 2016 following 3 different data-taking periods:

- Phase 1: 2016 commissioning run meant to estimate the beam-induced background (no collisions happening), with no final focus magnets installed. Measurements were performed with a suite of dedicated detectors, collectively known as BEAST II [41].
- Phase 2: 2018 run used mostly for commissioning studies. The detector installed was not complete since only a part of the Vertex Detector was in place. During this data-taking period the *BelleII* collaboration collected  $\sim 496 \text{ pb}^{-1}$  with which two physics results were published (see [42],[43] for more details).

- Phase 3: since March 2019 *BelleII* is taking data with the complete detector installed, reaching the highest instantaneous luminosity ever achieved up to now at a B-factory:  $L=2.4 \cdot 10^{34} \text{cm}^{-2} \text{s}^{-1}$ .

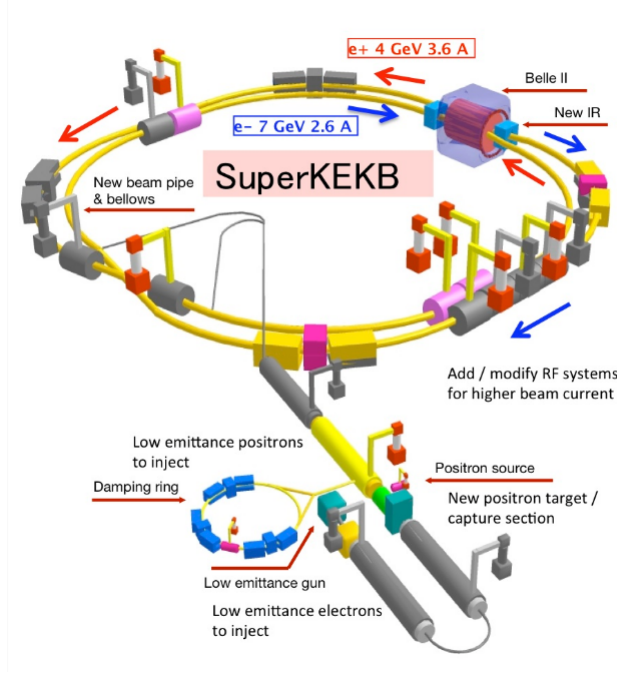


Figure 2.1: SuperKEKB accelerator system, from the production of the beams to the collisions at the IP.

### 2.1.1 Nano-beam scheme

The *BelleII* experiment is able to reach a high luminosity thanks to the new idea of the nano-beam scheme which consists in the minimization of the transversal dimensions of the colliding beams. The idea is to minimise, as much as possible, the betatron function  $\beta_y^*$ , that represents the transverse spread of the particles circulating in the collider with respect to their nominal trajectory. This is possible by reducing the overlap region of the beams  $d \simeq \sigma_{y^*} / \phi$  (see Fig. 2.2), where  $\sigma_{y^*}$  is the y dimension of the bunch at the IP. This will be reduced of a factor 20 with respect to KEKB, down to  $\sim 50$  nm. The reduced value of the overlap region represents a lower bound for  $\beta_y^*$  that can be expected to be squeezed to  $\sim \sigma_z / \phi_{Piw}^1$ , avoiding the hourglass

<sup>1</sup>The Piwinski angle  $\phi_{Piw}$  is defined as  $\theta_x \sigma_z / \sigma_x^* \sim 20$ , where  $\theta_x$  is the half horizontal crossing angle. The longitudinal size of the overlap between colliding bunches decreases by the Piwinski angle as  $\sigma_z / \phi_{Piw}$ , which is much shorter than the bunch length  $\sigma_z$ .

effect.

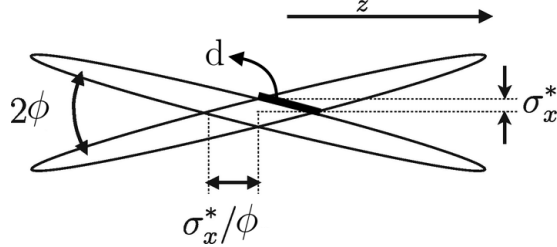


Figure 2.2: Schematic view of the nano-beam scheme adopted by *BelleII*.

The luminosity of the accelerator machine is expressed as follows:

$$L = \frac{\gamma_{\pm}}{2er_e} \left( 1 + \frac{\sigma_y^*}{\sigma_x^*} \right) \frac{I_{\pm} \xi_{y\pm}}{\beta_{y\pm}^*} \frac{R_L}{R_{\xi_y}} \quad (2.2)$$

where  $r_e$ ,  $e$  and  $\gamma$  are respectively the electron classical radius, the elementary electric charge and the Lorentz factor. The  $\pm$  signs distinguish the positron (+) from the electron (-) and the ratio between the parameters  $R_L$  and  $R_{\xi_y}$  represents a geometrical reduction factor, that takes into account the crossing angle. The overall value of these parameters is around 1 so the luminosity mainly depends on the remaining parameters: the total beam current ( $I_{\pm}$ ), the vertical beam-beam parameter ( $\xi_{y\pm}$ ) and the vertical beta function at the IP ( $\beta_{y\pm}^*$ ). A comparison between KEKB and SuperKEKB parameters is shown in Fig. 2.3.

	<b>KEKB</b>	<b>SuperKEKB</b>	
		2019	Design
Energy [GeV]	3.5/8.0	4.0/7.007	4.0/7.007
Beam current [A]	1.64/1.19	0.88/0.70	3.6/2.6
Number of bunches	1584	1576	2500
$\epsilon_x$ [nm]	18/24	2.0/4.6	3.2/4.6
$\xi_{y\pm}$	0.129/0.090	0.028/0.019	0.088/0.081
$\sigma_{y\pm}^*$ [nm]	940/940	140/180	48/62
$\beta_{y\pm}^*$ [mm]	5.9/5.9	1.0/1.0	0.27/0.30
$\beta_{x\pm}^*$ [mm]	1200/1200	80/60	32/25
Luminosity [ $\text{cm}^{-2}\text{s}^{-1}$ ]	$1.71 \times 10^{34}$	$1.14 \times 10^{34*}$	$8 \times 10^{35}$

Figure 2.3: Overview of the SuperKEKB and KEKB parameters [4],[5]. The comparison shows how the nano-beam scheme improves the luminosity.

The *BelleII* experiment is expected to collect data for a total integrated

luminosity of  $50 \text{ ab}^{-1}$  before 2031 and, as of now, the collected integrated luminosity is  $\sim 75 \text{ fb}^{-1}$ . The luminosity profile of SuperKEKB is reported in figure 2.4.

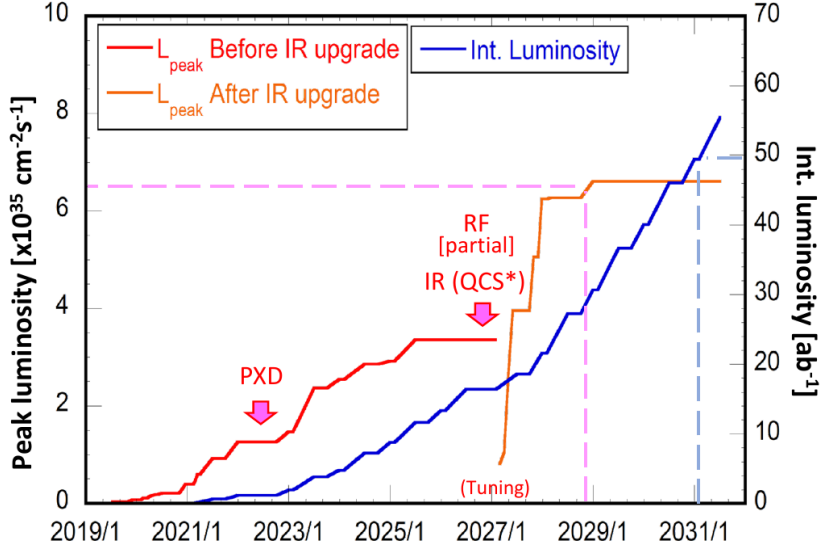


Figure 2.4: Luminosity profile of the SuperKEKB collider.

### 2.1.2 Particle production and environment advantages

The primary aim of SuperKEKB is the production of beauty hadrons. They can be largely generated by B-factories and hadronic machines (like the LHC), but the advantage of a B-factory is the extremely clean environment and a well known initial CM energy, at the expense of large cross sections and wide spectrum of beauty hadron production. The knowledge of the initial state allows to constraint the reconstruction of final state candidates, which is a powerful tool to further suppress background contributions.

SuperKEKB runs at a CM energy of the  $\Upsilon(4S)$  resonance, a bound state of  $b$  and  $\bar{b}$  quarks (*bottomonium*) which mainly decays to  $B\bar{B}$  pairs. These are produced almost at rest in the CM frame since the  $B$  mass is  $5.279 \text{ GeV}/c^2$ . SuperKEKB will allow to collect about  $55 \cdot 10^9$   $B\bar{B}$  pairs at full luminosity, giving huge advantages in flavour physics with respect to other statistically limited experiments like BES III [44] at Beijing Electron–Positron Collider II (BEPC II). The huge amount of  $e^+e^-$  collisions features a unique environment also for electroweak and QED studies. About  $45 \cdot 10^9$  of both  $\tau$

and  $\mu$  pairs are expected in the full data-set, giving the possibility to investigate a large amount of processes with high precision. In particular for  $\tau$  sector, it is convenient to search for new physics because of the well-understood mechanisms that govern its production and decay. The *BelleII* experiment is particularly suited to study  $\tau$  physics due to the clean environment and the usage of an hermetic detector: this allows to well reconstruct decays involving neutrinos in the final state, which are very difficult to manage at hadron colliders. As a consequence, the searches of processes with very small BF and the investigation of LFV decays, such as the  $\tau^\pm \rightarrow \mu^\pm \mu^\mp \mu^\pm$ , are very convenient.

The total production cross sections for various physics processes at *BelleII* [45] are shown in Tab. 2.1.

Table 2.1: Summary of the main production cross sections at *BelleII*.

Process	Cross section (nb)
$\Upsilon(4S)$	1.05
$u\bar{u}$	1.61
$d\bar{d}$	0.4
$c\bar{c}$	1.30
$s\bar{s}$	0.38
$\tau^+\tau^-$	0.92
$\mu^+\mu^-$	1.16
$e^+e^-$	$\sim 40$

## 2.2 The *BelleII* detector

In order to take advantage of the high luminosity provided by the SuperKEKB machine, the *BelleII* detector [40] needs to perform accordingly. Although the background contributions are expected to be 40 times higher than the ones in Belle, the *BelleII* detector aims to obtain at least the same performances achieved by its predecessor. The detector, from the innermost to the outermost part, is composed by the following sub-detectors:

- VerteX Detector (VXD): it is composed by a PiXel vertex Detector (PXD), a completely new silicon detector made of 2 layers of pixel sensors, and a Silicon-strip Vertex Detector (SVD), made of 4 layers of Double-sided Silicon Strip detector;

- Central Drift Chamber (CDC): wire chamber filled by a helium-ethane gas mixture, with the purpose of tracking charged particles together with the VXD;
- Particles IDentification (PID) system: it is composed by 2 Cherenkov-based detectors. A Time-Of-Propagation counter (TOP), made of quartz bars and located in the barrel region, and an Aerogel Ring-Imaging Cherenkov detector (ARICH), made of aerogel and located in the forward region;
- ELeCtromagnetic Calorimeter (ECL): it is made of CsI(T) truncated pyramid crystals providing  $16.1X_0$ ;
- Superconductive solenoid: it provides an homogeneous magnetic field of 1.5 T along the direction of the beams;
- $K_L^0$  and Muon (KLM): it is made of Resistive Plate Chambers (RPCs) and/or scintillators as active materials, alternated with iron plates as the absorber. The iron is also devoted to the return yoke of the magnetic field.

An overview of the whole *BelleII* detector is given in figures 2.5 and 2.6.

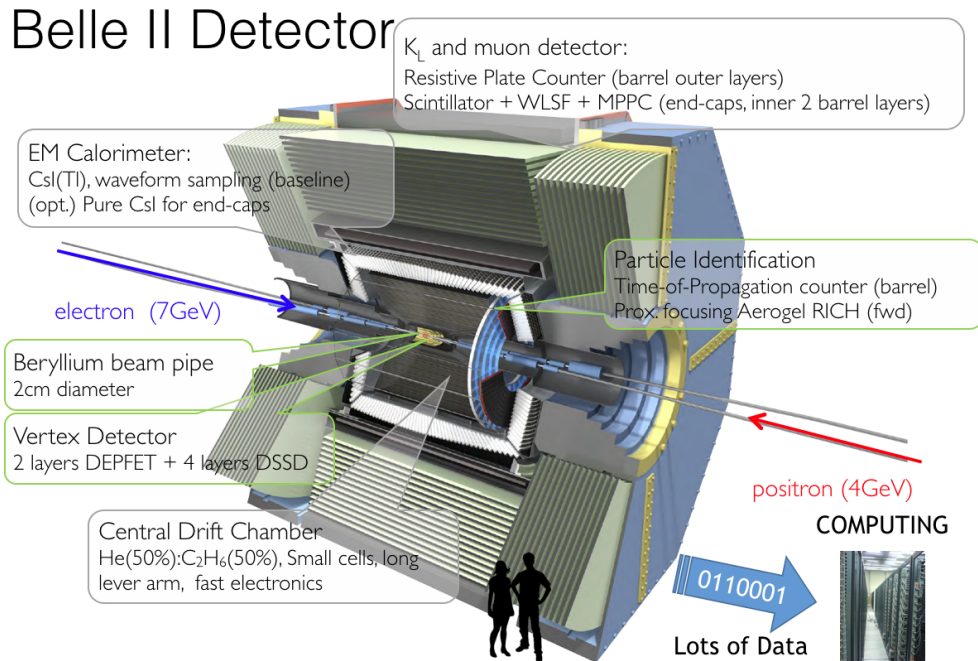


Figure 2.5: 3-D picture of the *BelleII* detector and its components.



### 2.2.1 Pixel vertex detector

The pixel vertex detector consists in two layers of pixel sensors based on DEPLETED Field-Effect Transistor (DEPFET) technology, covering a polar angular acceptance from  $17^\circ$  to  $155^\circ$ . In order to cope with the high background rate it is crucial to use a pixel technology close to the IP. The layers are placed respectively at 1.4 cm and 2.2 cm radially. The dimension of the single pixel is  $50 \times 50$ - $55 \mu\text{m}$  for the innermost layers and  $50 \times 70$ - $85 \mu\text{m}$  for the outermost ones. The readout electronics is moved outside the acceptance region to reduce the material budget (below  $0.2\%$   $X_0$  for each layer) so to minimize multiple scattering. The hit resolution is of the order of  $10 \mu\text{m}$ .

A schematic representation of the pixel detector is shown in figure 2.7 (left).

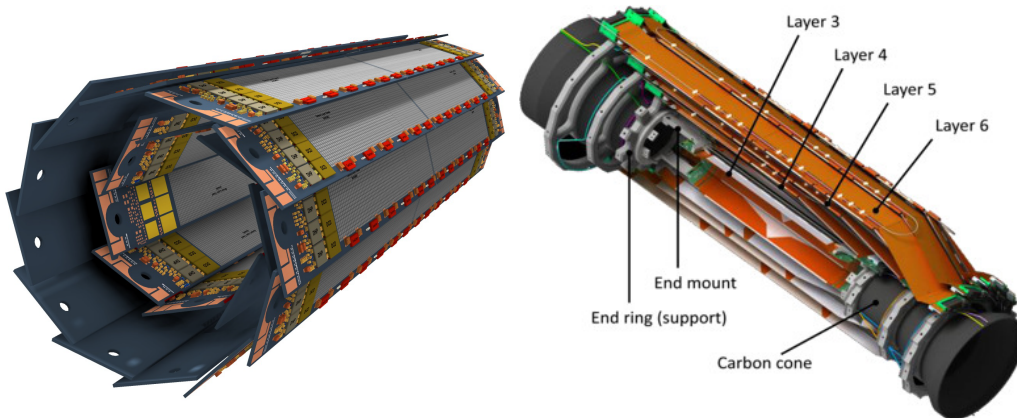


Figure 2.7: Schematic view of the PXD (left) and SVD (right) detectors.

### 2.2.2 Silicon-strip vertex detector

The SVD consists in four layers of Double-sided Silicon Strip Detectors (DSSDs) with an asymmetric polar angular acceptance that goes from  $17^\circ$  to  $150^\circ$ .

The four layers are made of several ladders composed by a different number of DSSD of distinct shapes (as shown in Fig. 2.7, right). An innovative technique, implemented to simplify the cooling system and reduce connections, is called the Origami chip-on-sensor. It uses a flexible kapton layer wrapped around the sensors that connects the two sides to the read out board. The average efficiency of hit reconstruction is found to be above

99.5%, while the hit resolution is  $\sim 11 \mu\text{m}$  in the  $r\text{-}\phi$  direction and  $\sim 30 \mu\text{m}$  in the  $z$  direction.

The combination of the PXD and SVD provides excellent vertex resolution as well as the reconstruction of low momentum tracks that do not reach the CDC.

### 2.2.3 Central Drift Chamber

The central drift chamber of *BelleII* is intended to measure the charged particle momentum. It provides information about the particle identification by measuring the energy loss and contributes deeply to the trigger decisions. The CDC is a large gaseous detector (50 % He, 50 % C<sub>2</sub>H<sub>6</sub>) composed by 56 cylindrical layers of wires, divided into 9 super-layers. The super-layers alternate between stereo and axial layers. The CDC polar angular coverage goes from  $17^\circ$  to  $150^\circ$  while radially it is placed between 16 cm and 113 cm.

The CDC structure is closed by two carbon cylinder and 2 aluminium end-plates. The two aluminium end-plates have complex conical shapes to limit occupancy, mostly from Bhabha scattering in the forward direction, and to maximize acceptance. The front-end electronic is located near the backward end-plate and it uses an Application-Specific Integrated Circuit (ASIC) chip that incorporates an amplifier, a shaper, and a discriminator. The readout system handles high trigger rates with less dead time, with respect to the corresponding readout system of Belle.

The CDC provides a position resolution of  $\sim 2 \text{ mm}$  in  $z$  and  $\sim 100 \mu\text{m}$  in  $r$  while the resolution on the energy loss is  $\sim 12\%$  for incoming particles at  $\theta = 90^\circ$ .

### 2.2.4 Particles identification system

The *BelleII* PID system is composed by the TOP and the ARICH sub-detectors. They are described separately below.

#### 2.2.4.1 Time-Of-Propagation counter

The TOP detector consists in 16 quartz bars placed between the CDC outermost cylinder and the ECL. A module is identified as 2 bars glued together, with a total length of 2500 mm and a transverse area of  $44 \times 20 \text{ mm}^2$ .

TOP measures the time of propagation of the Cherenkov photons internally

reflected in the quartz bars. A mirror is placed at the forward end of the quartz bars, in order to reflect photons, while at the backward end is an array of Micro-Channel Plate (MCP) PMTs that measure the x position and the precise time of arrival of incident photons (Fig. 2.8).

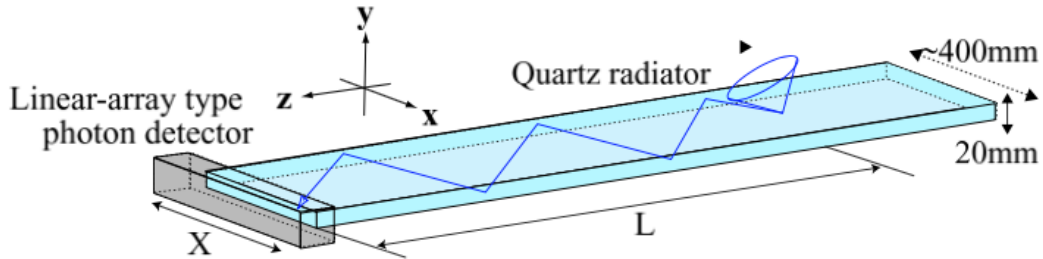


Figure 2.8: Design of a TOP quartz bar and propagation of the photons towards the MPC-PMTs.

By using the combined information of the arriving position and time of the tracks, provided by the tracking detectors, it is possible to extract the Cherenkov angle  $\theta_C$ . Consequently the velocity within the quartz bar can be estimated and the likelihoods for different mass hypothesis extracted. A schematic figure representing the working principle of TOP is shown in Fig. 2.9).

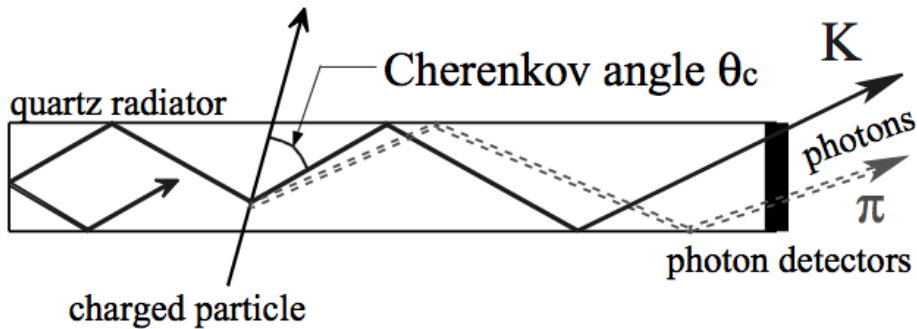


Figure 2.9: Representation of the total internal reflection of Cherenkov photons produced by kaons and pions inside a TOP quartz bar.

The MCP-PMTs have excellent timing and gain performance: the transit time spread is around 30 ps and the gain is  $\sim 10^6$  for single photo-electrons. The charge deposited on a MCP-PMT is converted to a waveform that will be used to determine the photon detection time, with a resolution of 50 ps.

### 2.2.4.2 Aerogel Ring-Imaging Cherenkov detector

The ARICH detector is placed in the forward endcap and it is composed by 4 main elements (see Fig. 2.10) each with specific aims:

- Silica aerogel Cherenkov radiator: the charged particles pass through the aerogel generating Cherenkov photons. This radiator is highly transparent in order to avoid the absorption and scattering of the generated photons;
- Expansion volume of 20 cm: the Cherenkov light originated in the aerogel radiates through this volume so that photons can be well distinguished at the adjacent photon detector;
- Photon detector: it consists of an array of Hybrid Avalanche Photo-Detector (HAPD), each made of Avalanche Photo-Diode (APD) sensors. The latter provide measurement of the position when at least 10 photons are detected, in order to ensure high precision.
- Readout system: it is able to readout  $\sim 80000$  channels from the photon detector using ASIC chips.

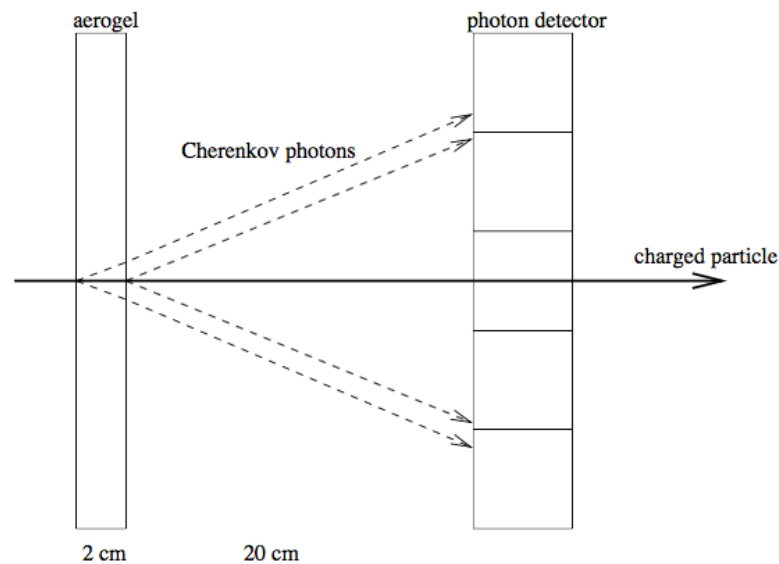


Figure 2.10: Schematic view of the main components and the working principle of the ARICH detector.

The resolution of a RICH counter is defined as  $\sigma_{track} = \sigma_0 / \sqrt{N_\gamma}$  where  $N_\gamma$  is the number of photons detected while  $\sigma_0 = 14.3$  mrad is the single photon resolution. The value of  $N_\gamma$  increases with the aerogel radiator thickness together with the uncertainty on the emission point of the radiation. The *BelleII* ARICH detector uses a non-homogeneous aerogel radiator with two layers of different refractive indices:  $n_1 = 1.046$  and  $n_2 = 1.056$ . This ensures a better focus of the Cherenkov rings thus a better measurement of the radius. The resolution is found to be  $\sigma_{track} \simeq 4.5$  mrad, assuming 12.7 photons detected per charged track in average.

### 2.2.5 Electromagnetic calorimeter

The ECL aims to detect photons over a wide energy range (from 20 MeV to 7 GeV) and to determine their energies and positions. It is also intended to identify electrons and to provide  $K_L^0$  identification together with the KLM. Moreover ECL is used in several trigger decisions and in the measurement of the instantaneous machine luminosity. The *BelleII* calorimeter is the upgrade version of the Belle one. It uses the same crystals and a new readout electronics system to cope with increased background conditions. The barrel section is 3 m long, with an inner radius of 1.25 m and a polar angular acceptance that goes from  $32.20^\circ$  to  $128.70^\circ$ . Including the endcaps, the acceptance is enlarged and goes from  $12.10^\circ$  to  $155.03^\circ$ . The total structure is made of 8736 CsI(T) crystals of truncated pyramid shape, with an average size about  $6 \times 6$  cm<sup>2</sup> in cross section and 30 cm in length, corresponding to about  $16 X_0$ .

The scintillation light is detected by two  $10 \times 20$  mm<sup>2</sup> photo-diodes, glued to the rear surface of each crystal. These are equipped with wave-form-sampling readout electronics to cope with a large pile-up noise and a high background environment. A LED is also used to inject light pulses into the crystal volume to monitor its optical behaviour. A pre-amplifier is attached to each photo-diode, providing two independent output signals from the crystals.

The intrinsic energy resolution  $\sigma_E$  of the calorimeter can be approximated as:

$$\frac{\sigma_E}{E} = \sqrt{\left(\frac{0.066\%}{E}\right)^2 + \left(\frac{0.81\%}{\sqrt[4]{E}}\right)^2 + (1.34\%)^2} \quad (2.3)$$

where the energy  $E$  is measured in GeV.

### 2.2.6 $K_L$ and $\mu$ detector

The KLM detector is located outside the superconducting solenoid and it is meant to provide the Particle identification (PID) for particles with high penetration power:  $\mu^\pm$  and  $K_L$ .

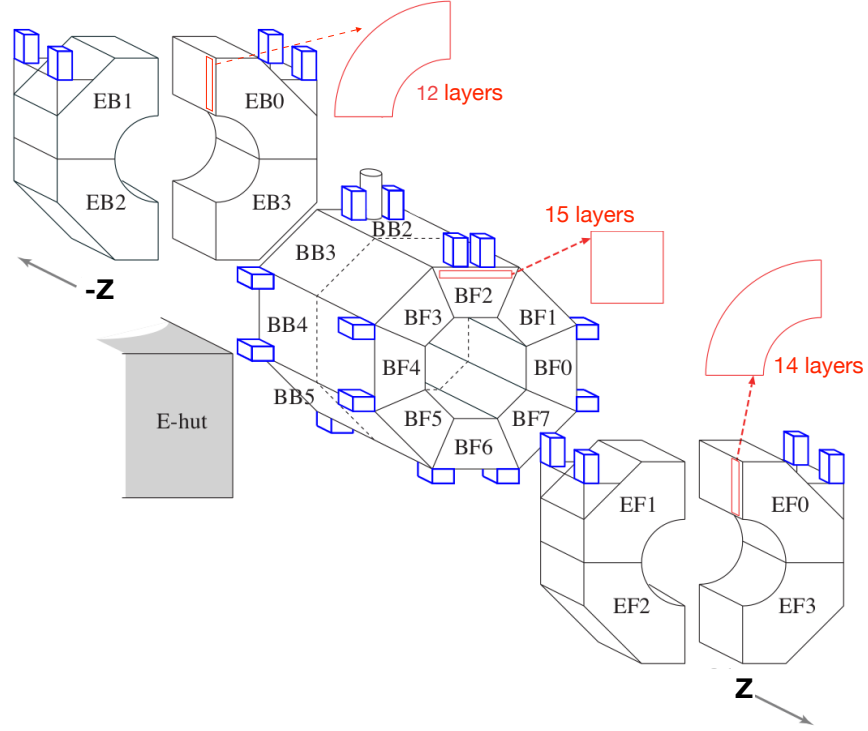


Figure 2.11: KLM schematic composition.

It is divided into a barrel (BKLM) and an endcap region (EKLM) (see Fig. 2.11):

- BKLM is composed of 16 sectors: 8 forward (BF) and 8 backward (BB). Each sector has 15 layers equipped with Resistive Plate Chambers (RPC), except for the first innermost 2 which use scintillators, alternated with 4.7 cm thick iron plates. The latter are needed as magnetic flux return for the solenoid and provide 3.9 interaction lengths ( $\lambda_0$ ), allowing hadronic showers of  $K_L^0$ s. Each layer is made of 2 planes of RPCs coupled together: these have independent HV controls and orthogonal strips configuration. The polar angle acceptance is within  $37^\circ$  and  $130^\circ$  (see Fig. 2.12) .

- EKLM is composed of 8 sectors: 4 forward (EF) and 4 backward (EB). Each sector includes 14 (12) layers in the forward (backward). EKLM layers are made of 2 orthogonal scintillator planes, needed to cope with the expected high background rate and mainly induced by slow neutrons in *BelleII*. The Belle experiment used only RPCs with their long dead time. The Belle experiment used only RPCs with their long dead time. The polar angle acceptance goes from  $18^\circ$  to  $47^\circ$  and from  $122^\circ$  to  $155^\circ$  (see Fig. 2.12)

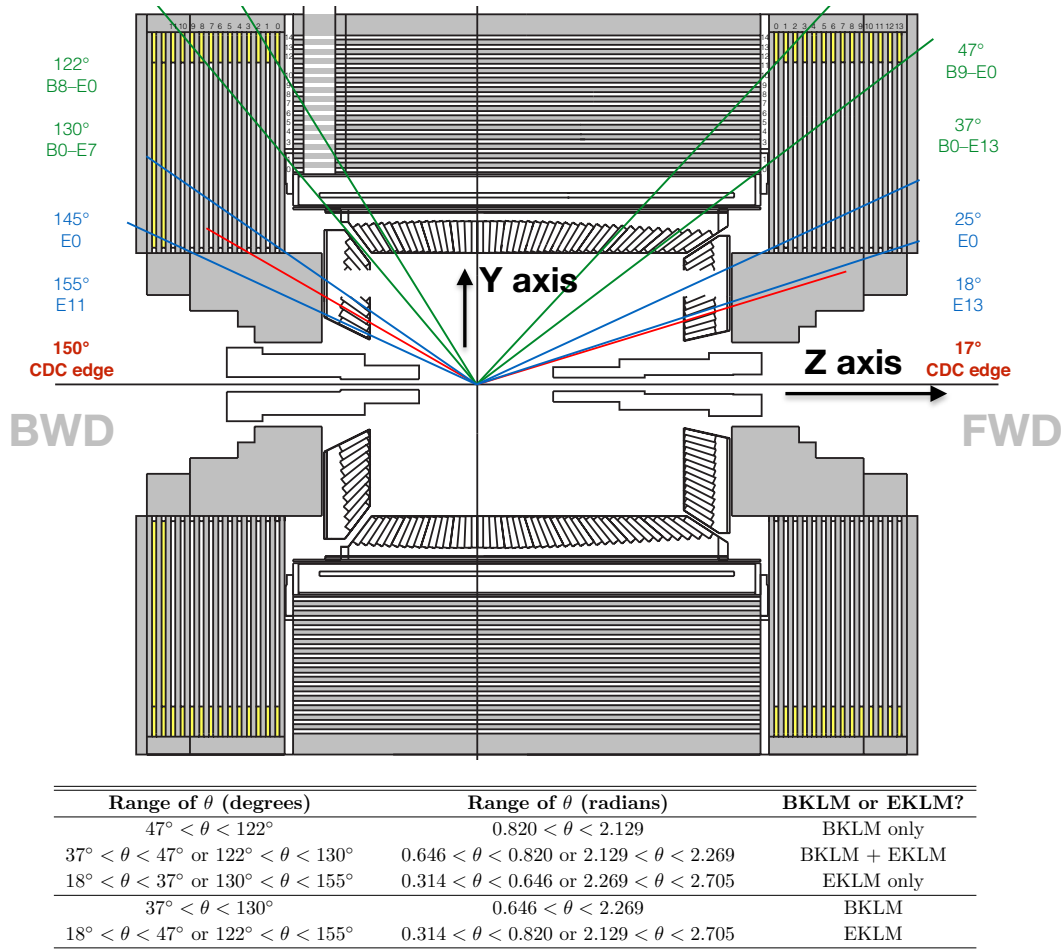


Figure 2.12: KLM geometrical scheme. The angular acceptance of each sub-region is summarised at the bottom of the image.

The scintillator strips have a cross section of (7-10)x40 mm and a length of  $\sim 2.8$  m. They accommodate Wave Length Shifter (WLS) fibers in the center, in order to guide the light towards Silicon Photo Multiplier (SiPMs)

coupled at the strip ends (see Fig. 2.13). The SiPMs is made of a matrix of pixel photodiodes that have a time resolution of  $\sim 1$  ns, allowing the KLM to provide measurements of the  $K_L^0$  time-of-flight.

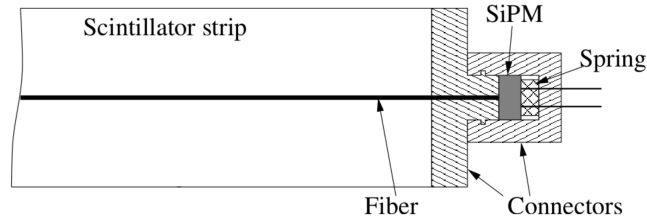


Figure 2.13: KLM scintillator strip scheme. The read out system is displayed at the edge of the strip.

The RPC consists in two parallel sheets of float glass (the electrodes) separated by 1.9 mm of free space. This gap is filled with a gas mixture composed by 62% HFC-134a, 30% argon, and 8% butane-silver. The high voltage is applied to the electrodes through a thin layer of carbon-doped paint, placed on the outer surfaces of each electrode (see Fig. 2.14).

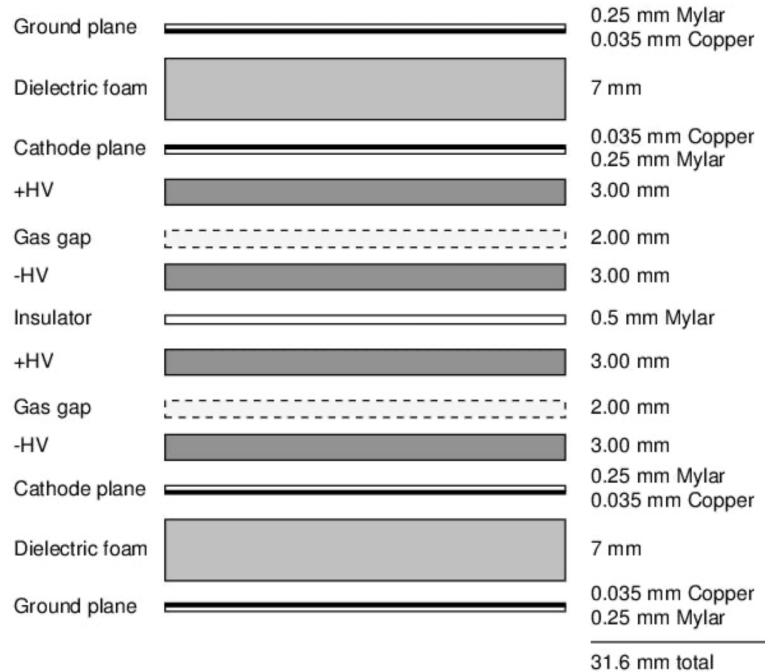


Figure 2.14: KLM RPC layer detailed composition.

A substantial upgrade of the KLM structure, involving the substitution of RPC with scintillator layers, is foreseen before the end of 2026.

The KLM gives information about the passage of a particle by detecting the presence of hits in each layer and by providing time measurements. At the moment, the timing algorithm has to be further developed thus no time information can be used (this will be crucial in order to have a well performing  $K_L^0$  identification). The reconstruction efficiency of muons with more than 1 GeV momentum is  $\sim 90\%$  (see section 3 for more details) while  $K_L^0$  reconstruction efficiency is  $\sim 80\%$  for particles with momentum  $>3$  GeV.

### 2.2.7 Trigger

SuperKEKB will provide a total event rate of  $\sim 50$  kHz at the maximum instantaneous luminosity. The environment at the  $e^+e^-$  colliders is relatively clean with the exception due to the high Bhabha rate, which has to be somehow limited. A solid trigger system is required for several very low multiplicity channels such as  $\tau$  decays, two-photon physics or even single photon triggers for dark photon searches. The *BelleII* trigger system is divided into a Level 1 trigger (L1) and a High Level Trigger (HLT). A schematic view of the trigger flow is reported in Fig. 2.15.

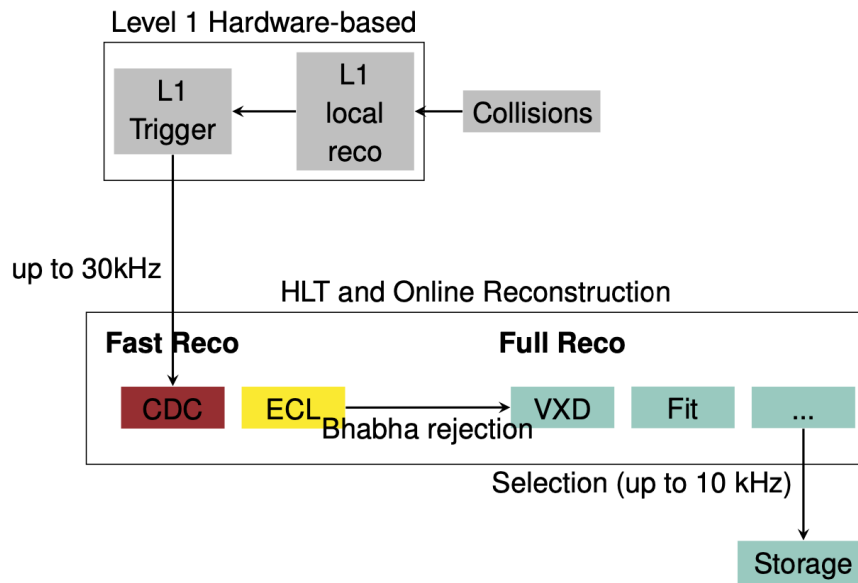


Figure 2.15: Scheme of the working principle of the *BelleII* trigger system.

The L1 trigger is implemented at hardware level and it gathers signals from many sub-trigger systems, with a maximum rate of 30 kHz. The information coming from the corresponding sub-detectors are summarized and sent to the Global Decision Logic (GDL). A large part of the L1 trigger information is provided by the CDC and the ECL. All the trigger components are based on a Field Programmable Gate Array (FPGA) logic. The CDC provides two-dimensional and three-dimensional tracking information and uses the  $z$  coordinate of the tracks to reject beam background events (for which the track vertices are far from the IP). New techniques exploiting neural network approaches are currently being studied and their performances seem promising. The ECL trigger system uses two complementary configurations: a trigger line based on the total energy released in the calorimeter and an isolated-cluster counting trigger. The former is able to identify Bhabha scattering and  $\gamma\gamma$  events with high efficiency and veto most of them, while the latter increases the efficiency for low multiplicity events.

The HLT is implemented at software level and it is intended to further reduce the event rate down to 10 kHz. As a first step, the HLT performs a fast reconstruction with the software used in offline analysis, relying on information coming from all sub-detectors apart from PXD. The reconstructed tracks (formed by CDC+SVD) are extrapolated back to the PXD to define Region of Interests (ROI), used to select the PXD hits to be combined later. The HLT filter was not turned on during the data taking period but it was used to produce some offline skims (for example for dimuon and hadronic events).

### 2.3 *BelleII* software general description

The *BelleII* software, called BASF2 (Belle Analysis Software Framework 2) [46], provides the tools to perform physics analyses using a module-based framework. It is made of a fixed set of virtual functions available to all the modules, that can be gathered together and sequentially executed in order to form a path, which is managed by a so-called steering file (written using a Python script language interpreter). Modules also mutually exchange information through a common data-store and can communicate with a database store that provides all sort of calibrations and settings, as shown in Fig. 2.16. The BASF2 software imports some external libraries such as: EvtGen [47] and PYTHIA [48], used for the event generation process, Geant4 [49], used to simulate the interactions of the particles with matter, and ROOT [50], used to analyse the data.

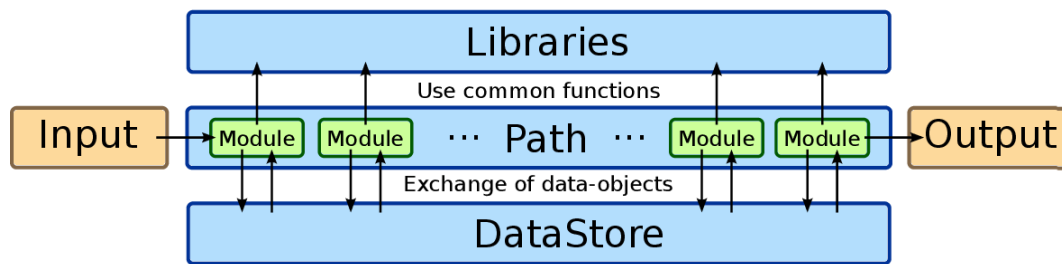


Figure 2.16: Schematic example of the event processing chain in BASF2.



## Chapter 3

# Muon identification at the *BelleII* experiment

The PID is based on detector quantities coming from the *BelleII* sub-detectors. The algorithms are implemented in different ways and their outcomes are quantified in log-Likelihood values assigned to six particle hypothesis independently: e,  $\mu$ ,  $\pi$ , K, P, d (deuteron). These values are combined together as a sum, in order to have a unique likelihood per particle. The combination of the log-likelihoods is performed considering the same weights for each sub-detectors. Assuming the pion case as an example:

$$\log\mathcal{L}_\pi = \log\mathcal{L}_\pi^{\text{SVD}} + \log\mathcal{L}_\pi^{\text{CDC}} + \log\mathcal{L}_\pi^{\text{TOP}} + \log\mathcal{L}_\pi^{\text{ARICH}} + \log\mathcal{L}_\pi^{\text{ECL}} + \log\mathcal{L}_\pi^{\text{KLM}}. \quad (3.1)$$

The final PID variable used in physics analyses is then normalised to every particle hypothesis, as reported in Eq. 3.4.

The muon identification (muonID) performances rely mostly on ECL, TOP and KLM detector information. Restricting to the muon and pion cases, the fake rate is defined as the probability of identifying a real muon as a pion, while the mis-ID rate is the probability of identifying a real pion as a muon. More in detail, the ECL provides separation between muons and electrons, protons and deuterons via the calorimetric energy deposition. Since muons produced at *BelleII* are in the vast majority of the cases Minimum Ionising Particles (MIP), they loose a small amount of energy in the ECL crystals, in contrast to the other type of particles. Fake rates from kaons are handled mainly by the TOP detector, that provides further discrimination by using information about the Time of Flight (TOP) and the time of propagation of the Cherenkov light. Pions behave very similarly to muons and the only powerful way to discriminate between the two is to

rely on the KLM, that overall provides the largest contribution. Several channels were taken into account to investigate the muonID at *BelleII*: for the efficiency,  $J/\Psi \rightarrow \mu\mu$ ,  $e^+e^- \rightarrow e^+e^-\mu^+\mu^-$ ,  $e^+e^- \rightarrow \mu^+\mu^-\gamma$  while for the mis-ID rates,  $K_S^0 \rightarrow \pi^+\pi^-$ ,  $D^{*+} \rightarrow D^0(K^-\pi^+)\pi^+$  and  $e^+e^- \rightarrow \tau^\pm(1P)\tau^\mp(3P)$ . An overview of the results is shown in Fig. 3.1 as a function of the momentum of the tracks.

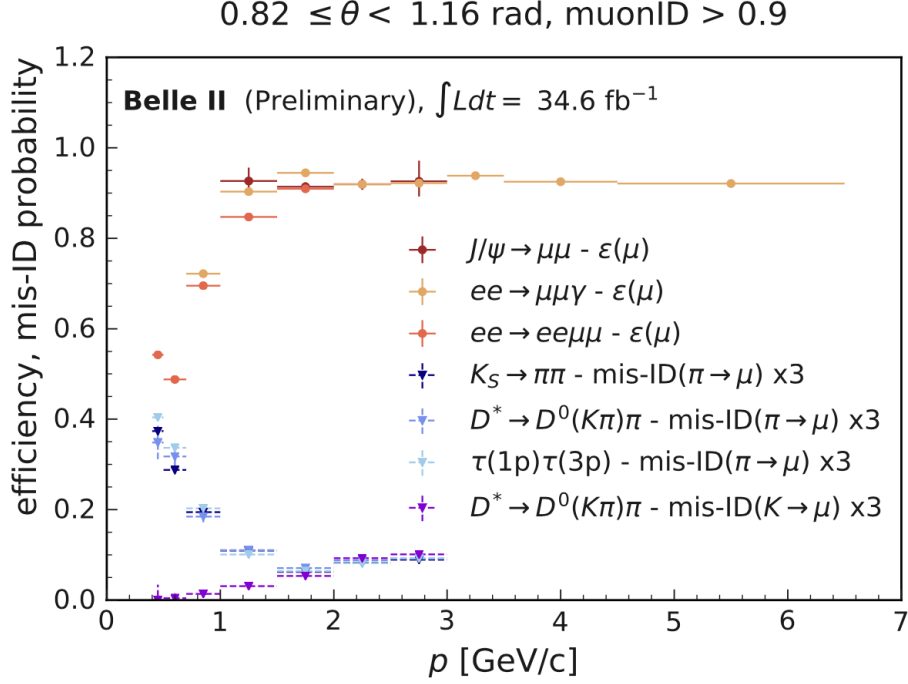


Figure 3.1: Summary of muonID efficiencies and hadron-lepton mis-ID rates in a specific BKLM  $\theta$  bin, for a threshold of 0.9. Note that the mis-ID rate was inflated by a factor 3 for illustration purposes.

The following chapter will describe in more details the muon identification algorithm based on the KLM detector and my contribution on the topic, from the software development to the physics analysis.

### 3.1 Muon identification in the KLM

The KLM sub-detector is devoted to the identification of  $K_L^0$  and muons: the optimisation of the muonID algorithm plays a crucial role in *BelleII*. The working principle is based on two major steps: track extrapolation process towards KLM and likelihood extraction for each particle hypothesis: electron,

muon, pion, kaon, proton and deuteron. A combination of the likelihoods gives the final muon probability. An important part of the algorithm concerns the usage of data-driven KLM efficiency.

### 3.1.1 Track extrapolation

Track extrapolation is provided by the Geant4 [49] toolkit designed to simulate the passage of particles through matter and complex detector geometries, making it widely used in the particle physics field. The extrapolation towards KLM of tracks reconstructed by the tracking detectors, always assumes the muon hypothesis and starts at the outermost CDC layer that detected a hit. During the extrapolation process the energy loss ( $dE/dx$ ) and the elastic multiple scattering are taken into account: the momentum of the tracks is then reduced and the elements of the covariance matrix are inflated. On the other hand, neither the particle decays in flight nor the interaction via other physics processes is allowed. The extrapolation makes use of a Kalman-filter algorithm that exploits the presence of matching 2-D hits in the KLM layers to adjust the trajectory by changing the parameters and the covariance matrix of the tracks. A 2-D hit is considered matched when it is less than  $3.5\sigma$  away from the extrapolated position, where  $\sigma$  is the sum in quadrature of the hit detection uncertainty and the extrapolation related error (see Fig. 3.2).

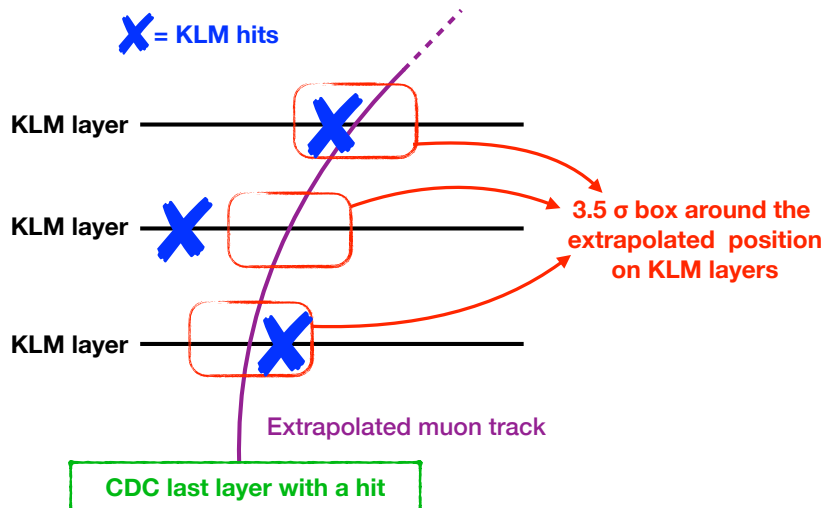


Figure 3.2: Schematic view of the track extrapolation process from CDC towards KLM with matching and non-matching hits displayed.

In case the extrapolation process reaches at least one KLM layer, the algorithm proceeds forward, otherwise the final likelihood value is set to Not A Number (*NaN*).

### 3.1.2 Likelihood determination

The likelihood value assigned to the tracks is the product of two terms: one based on the differences in the penetration depth (longitudinal probability) and the other based on the transverse shower dimension in the KLM (transverse probability). In order to compute these quantities, probability values were pre-calculated from MC and assigned to each KLM layer. From now on, this probability is called  $\text{prob}_n$  (or  $\text{prob}_n^t$ ) where  $n$  is the number of the  $n^{\text{th}}$  KLM layer. The value of  $\text{prob}_n$  (or  $\text{prob}_n^t$ ) depends on the presence of hits in the  $n^{\text{th}}$  KLM layer: the detection of a hit implies a higher probability that the track is a muon compared to other particles. Those probabilities are obtained for each particle hypothesis and, as seen from figures 3.3, 3.4, 3.5, the shape differences provide the discriminating power.

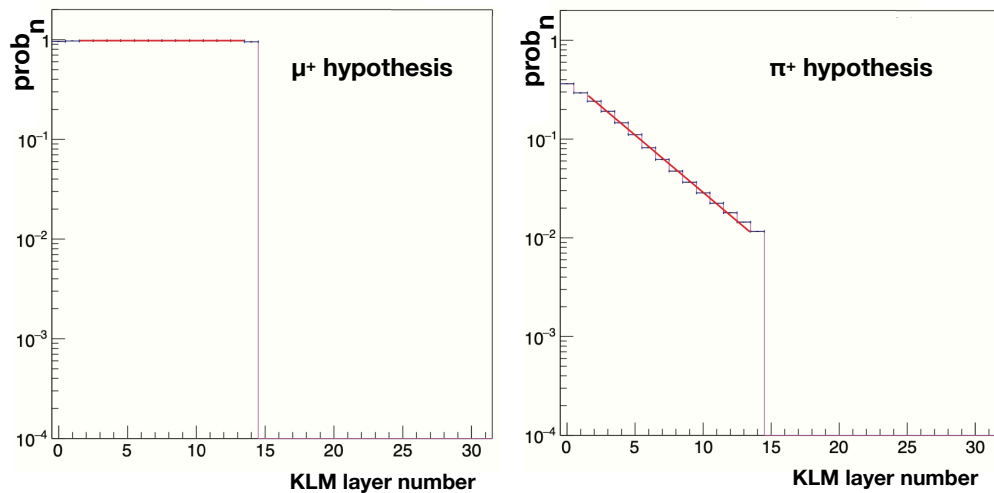


Figure 3.3: Probability  $\text{prob}_n$  dependence upon the barrel KLM layer number when a particle exits the BKLM. The muon (left) and pion (right) hypothesis cases are shown.

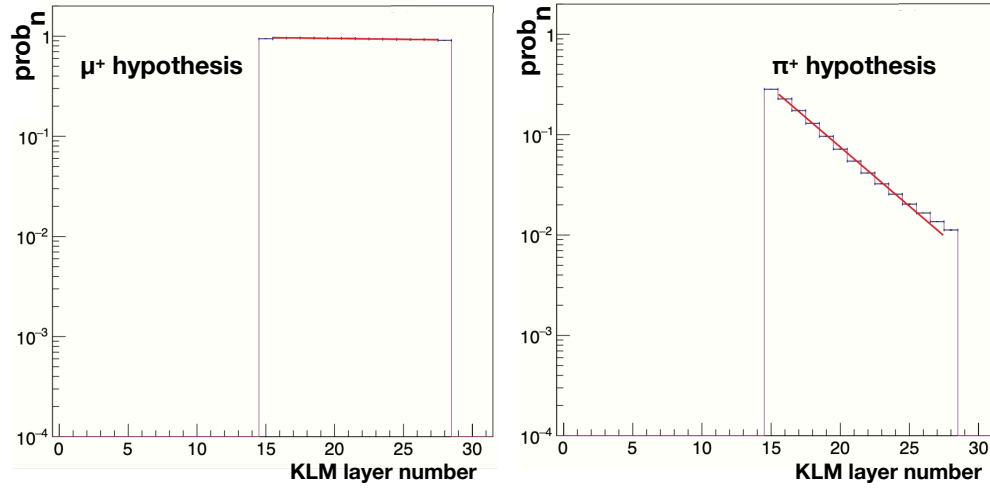


Figure 3.4: Probability  $\text{prob}_n$  dependence upon the endcap KLM layer number when a particle exits the EKLM without crossing the BKLM. The muon (left) and pion (right) hypothesis cases are shown.

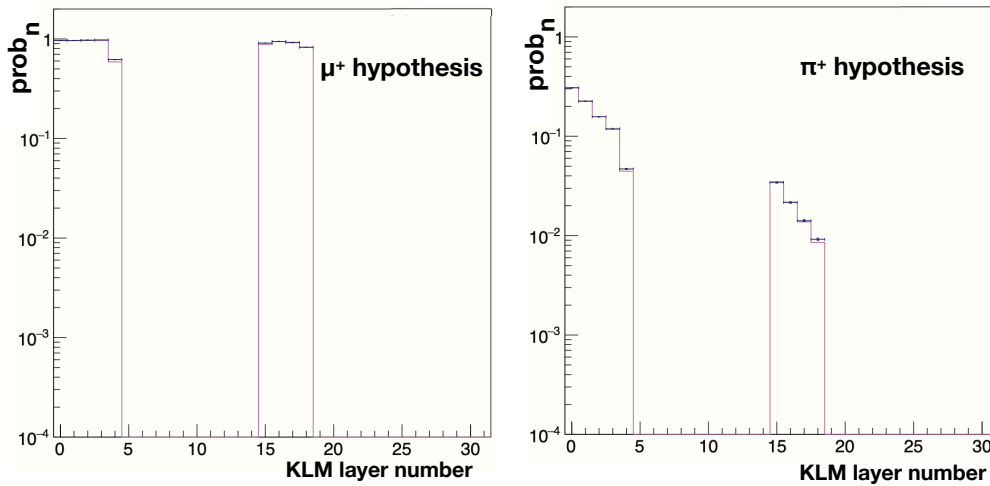


Figure 3.5: Probability  $\text{prob}_n$  dependence upon the entire KLM layer number when a particle exits the EKLM, crossing the BKLM first. The muon (left) and pion (right) hypothesis cases are shown.

The longitudinal probability has the best discriminating power and a key parameter is the outermost layer reached by the extrapolation process. The

probability assigned to the  $n^{\text{th}}$  layer ( $P_n$ ) is defines as:

$$P_n = \begin{cases} \text{prob}_n & \text{if the } n^{\text{th}} \text{ layer detects a hit} \\ 1 - \text{prob}_n \cdot \varepsilon_n & \text{if the } n^{\text{th}} \text{ layer does not detect a hit} \end{cases} \quad (3.2)$$

where  $\varepsilon_n$  is the efficiency of the  $n^{\text{th}}$  layer. Efficiencies values are typically  $\sim 95\%$  for EKLM,  $\sim 99\%$  for the RPC layers of BKLM,  $\sim 80\%$  for scintillator layers of BKLM. The usage of the efficiency in Eq. 3.2 is crucial to have good performances. If KLM layer efficiencies are considered to be 100% in the algorithm, then an inefficient layer would mimic the behaviour of a non-muon particle and the discrimination power would be reduced.

The efficiency was not a part of the algorithm before my intervention and there was no strategy on how to handle the problem of inefficient layers. The *BelleII* collaborators did not use the muonID in physics analyses, since performances were too low.

The likelihood  $\mathcal{L}_{\text{long}}$  is defined as the product of the  $P_n$  associated to the outermost extrapolated layer with the probabilities of all the previous ones.

$$\mathcal{L}_{\text{long}} = \prod_{n=0}^{\text{next}} P_n \quad (3.3)$$

where  $n_{\text{ext}}$  is the outermost extrapolated layer.

For the estimation of the transverse probability, in analogy to the longitudinal case, probabilities assigned to each KLM layers ( $\text{prob}_n^t$ ) are introduced. These are sampled according to the measurement of the  $\chi^2$  from the Kalman-filter used in the track extrapolation process. The  $\text{prob}_n^t$  for the muon hypothesis are very close to an ideal reduced  $\chi^2$  distribution for a given number of degrees of freedom (d.o.f.), corresponding to twice the number of layers with matched hits. For the remaining particle hypotheses the  $\text{prob}_n^t$  follow much broader distributions, especially for low d.o.f. (corresponding to the first KLM layers), the most likely scenario for a true non-muon. Therefore, the comparison between the  $\text{prob}_n^t$  probabilities with an ideal  $\chi^2$  distribution for a given number of d.o.f. can help in discriminating muons from all the other particles. The  $\text{prob}_n^t$  probability is tabulated as a reduced- $\chi^2$  distribution which is allowed to go up to 10. For values below a tabulated cutoff, a spline interpolation is considered, while for values above this cutoff an ad-hoc function is used, as displayed in Fig. 3.6. The transverse probability has less discriminating power with respect to the longitudinal one and it turns out to be useful in the first layers, since non-muon particles would most likely be stopped there. The corresponding likelihood is calculated as for the longitudinal case (see Eq. 3.3).

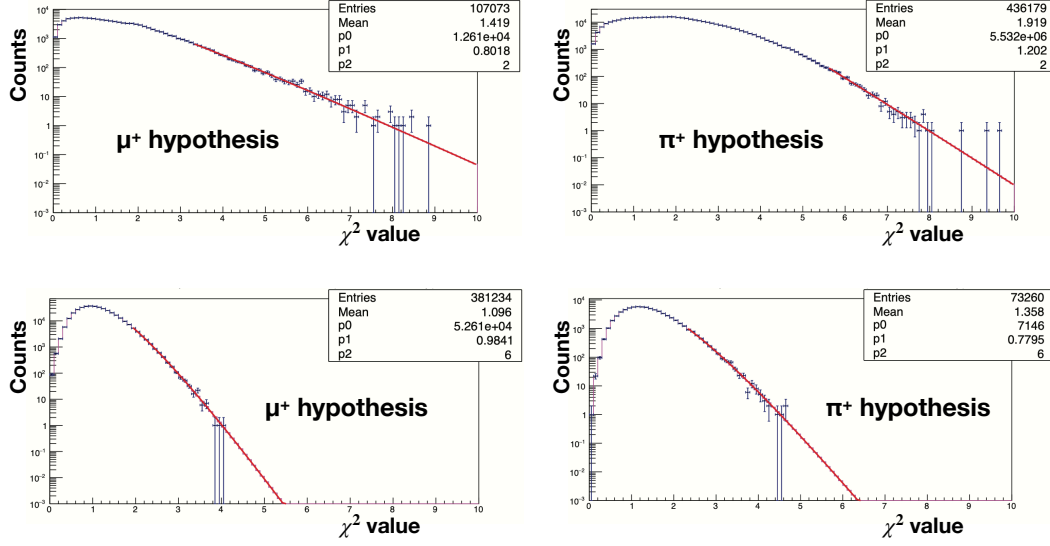


Figure 3.6: Reduced  $\chi^2$  distributions for  $\mu^+$  (left) and  $\pi^+$  (right) for 4 (top) and 12 (bottom) d.o.f.. The red line is the fit to the upper tail of the histogram.

For both longitudinal and transverse probabilities, the algorithm will assign a likelihood equal to 0 to all particle hypotheses, if the extrapolation of the tracks does not reach an active area of the KLM. In addition, layers flagged as dead (or hot) are not taken into account by the muonID algorithm.

As a last step, for each track, the algorithm provides likelihoods  $\mathcal{L}$  for all the particle hypotheses, as the product of the longitudinal and transverse probability values. The final muonID variable based on KLM ( $\mu\text{ID}^{\text{KLM}}$ ) is defined as the muon likelihood  $\mathcal{L}$  normalised to the sum of the likelihoods of all the particle hypotheses:

$$\mu\text{ID}^{\text{KLM}} = \frac{\mathcal{L}_\mu^{\text{KLM}}}{\mathcal{L}_e^{\text{KLM}} + \mathcal{L}_\mu^{\text{KLM}} + \mathcal{L}_\pi^{\text{KLM}} + \mathcal{L}_K^{\text{KLM}} + \mathcal{L}_p^{\text{KLM}} + \mathcal{L}_d^{\text{KLM}}} \quad (3.4)$$

For each particle hypothesis the final muonID variable is computed through the sum of the  $\log \mathcal{L}_\mu$  of all sub-detectors, as reported in Eq. 3.1.

## 3.2 Muon identification performances in $e^+e^- \rightarrow \mu^+\mu^-\gamma$ channel

The *BelleII* collaboration produced several performance studies of leptonID (e and  $\mu$  identification) based on different final states to check the consistency of the measurements (see Fig. 3.1). The  $e^+e^- \rightarrow \mu^+\mu^-\gamma$  channel is one of the studied ones and results are made available in bins of momentum (p) and polar angle ( $\theta$ ) [51]. For muons in particular, the KLM geometry was strictly taken into account with a careful choice of the angular bins, and with momentum bins related to the penetrating power of tracks. A summary table of the momentum and theta bins is reported in Tab. 3.1.

Table 3.1: Summary table of momentum and polar angle bins (together with the KLM sections) used to provide the muonID corrections.

p [GeV] intervals	$\theta$ (rad) intervals	KLM sections
0.5 / 0.7	0.40 / 0.64	EKLM fwd
0.7 / 1.0	0.64 / 0.82	EKLM-BKLM separation fwd
1.0 / 1.5	0.82 / 1.16	BKLM-fwd
1.5 / 2.0	1.16 / 1.46	BKLM-central
2.0 / 2.5	1.46 / 1.78	BKLM-bwd
2.5 / 3.5	1.78 / 2.13	BKLM-solenoid chimney region
3.5 / 4.5	2.13 / 2.22	EKLM-BKLM separation bwd
4.5 / 6.5	2.22/2.60	EKLM bwd

At this stage of the experiment in particular, having a good muonID is very important and data-MC correction values are crucial for several analysis works. As an example, the updated version of the first *BelleII* analysis paper (that I contributed to) on the "Search for an invisibly decaying  $Z'$  dark boson in  $e^+e^- \rightarrow \mu^+\mu^-(e^\pm\mu^\mp) + \text{missing energy}$  final states" will heavily rely on the muonID.

I focused my attention on the analysis of the  $\mu\mu(\gamma)$  channel, for which I produced the correction values used for high momentum tracks.

### 3.2.1 Efficiency definition

A tag and probe method is used for the muonID efficiency estimation in the radiative dimuon channel. The tag muon is required to have  $\text{muonID} > 0.9$  in order to define a clean muon sample. The muonID of the probe muon is

### 3.2. MUON IDENTIFICATION PERFORMANCES IN $E^+E^- \rightarrow \mu^+\mu^-\gamma$ CHANNEL 47

compared with 3 reference values: 0.5, 0.9 and 0.95. The efficiency  $\varepsilon_{\mu ID}^{data}$  is defined as follows:

$$\varepsilon_{\mu ID}^{data} = \frac{N_{probe \mu} - \sum_{i,j} N_{probe}^{bkg,i,\mu} \cdot r_{mis-id}^i \cdot r_{mis-id}^\mu}{N_{tag \mu} - \sum_i N_{tag}^{bkg,i} \cdot r_{mis-id}^i} \quad \text{with } i \in \{e, \pi, K, p, d\} \quad (3.5)$$

where  $N_{probe \mu}$  ( $N_{tag \mu}$ ) is the number of probe (tag) muons,  $N_{probe}^{bkg,i,\mu}$  is the number of probe MC background events per particle hypothesis  $i$  when the tag track is a muon,  $N_{tag}^{bkg,i}$  is the number of tag MC background events per particle hypothesis  $i$ ,  $r_{mis-id}^i$  is the mis-identification rate ratio between data and MC. At the moment  $r_{mis-id}^i$  is considered 1 and the main mis-ID contribution comes from the pion.

For the MC the efficiency  $\varepsilon_{\mu ID}^{MC}$  is evaluated as follow:

$$\varepsilon_{\mu ID}^{MC} = \frac{N_{probe \mu}}{N_{tag \mu}} \quad (3.6)$$

#### 3.2.2 Event selection

In order to provide efficiency and correction values for the dimuon radiative process, 100 fb<sup>-1</sup> of MC and 34.6 fb<sup>-1</sup> of data were used. The selection cuts applied to reconstruct the channel are:

- Tracks coming from the IP:  $dr < 2$  cm and  $-5$  cm  $< dz < 5$  cm where  $dr$  ( $dz$ ) is the radial( $z$ ) distance of the track from the IP (see Sec.4.2.1);
- Number of tracks in the event to be exactly 2;
- Photon selection:  $E > 0.5$  GeV, number of hits per ECL cluster  $> 1.5$  and  $-0.8660 < \cos \theta < 0.9563$  (ECL acceptance);
- Muon momentum:  $0.7$  GeV  $< p_\mu < 8.0$  GeV;
- Invariant mass of the  $\mu^+\mu^-\gamma$  system:  $10.2$  GeV  $< M_{\mu^+\mu^-\gamma} < 10.8$  GeV;
- One of the muon in the event (tag muon) with  $\text{muonID} > 0.9$ .

The data and MC distributions of  $M_{\mu^+\mu^-}$ ,  $p_\mu$  and  $\theta_\mu$  in the lab frame are reported in Fig. 3.7 and 3.8. The MC samples were normalized to the data-set statistics.

Results show an overall discrepancy of  $\sim 2\%$ , which increases in the KLM endcap regions and for very high momentum tracks (more than 6 GeV). These cases are correlated to the low and the high regions of the spectrum of the di-muon mass distribution, where the detector has irregular performances.

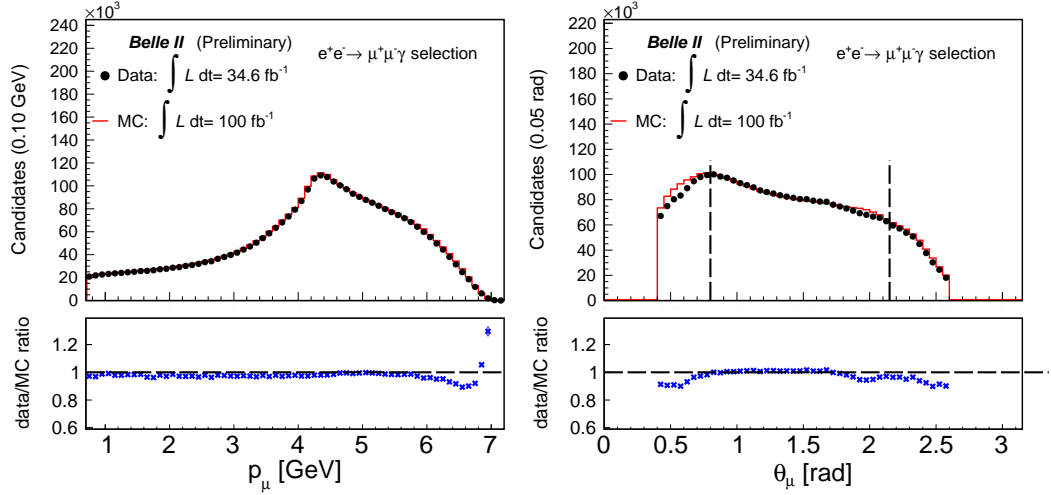


Figure 3.7: Momentum (left) and theta (right) distributions of the muons in the lab frame. The data/MC ratios are displayed on the bottom.

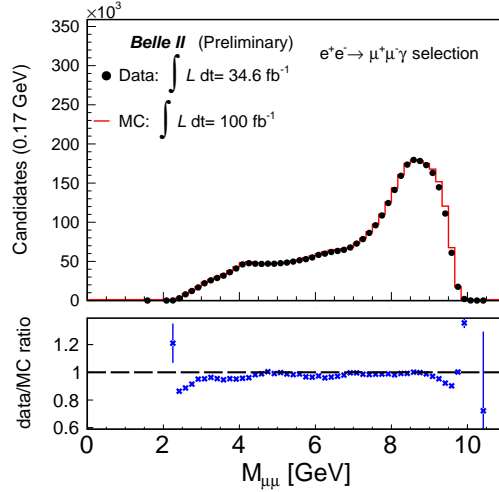


Figure 3.8: Data-MC agreement of the invariant mass distribution of the  $\mu\mu$  system.

### 3.2.3 Systematic uncertainty

The systematic error is estimated by varying  $N_{probe}^{bkg}$  ( $N_{tag}^{bkg}$ ) in Eq. 3.5 within  $0.9 \cdot N_{probe}^{bkg}$  ( $N_{tag}^{bkg}$ ) and  $1.1 \cdot N_{probe}^{bkg}$  ( $N_{tag}^{bkg}$ ). This choice is much conservative since it is based on the discrepancies observed in Fig. 3.7 and 3.8, which do not show a perfect agreement. The new efficiency value, calculated as in Eq. 3.5, is then subtracted to the original one and the absolute value of the difference is taken as the systematics.

### 3.2. MUON IDENTIFICATION PERFORMANCES IN $E^+E^- \rightarrow \mu^+\mu^-\gamma$ CHANNEL 49

The only MC samples used to estimate the contamination are listed below:

- $e^+e^- \rightarrow \tau\tau$ : 100 fb<sup>-1</sup> considering a cross section of 0.919 nb.
- $e^+e^- \rightarrow \pi\pi\gamma$  100 fb<sup>-1</sup> considering a cross section of 0.167 nb (extracted from PHOKHARA generator [52], as implemented inside the BASF2 code). This is the dominant contribution.

The  $\mu^+\mu^-\gamma$  sample is very pure as the contamination coming from the above processes is around 1%. The result on systematics is driven by the data-MC disagreement observed in the kinematic distributions. Overall, systematics of the order of 0.5%-1% are estimated. Results are shown in Tab. 4,5,6 in Appendix 6.3.

#### 3.2.4 muonID efficiency results

The muonID efficiency depends strongly on the momentum and the theta angle of the muons. Due to material energy loss, tracks with momentum up to 1.5 GeV can stop inside the KLM, meaning that not all the layers can provide information, consequently the efficiency decreases. The efficiency can go down to 70% for tracks with  $p < 1$  GeV. In Fig. 3.9 the efficiency distribution

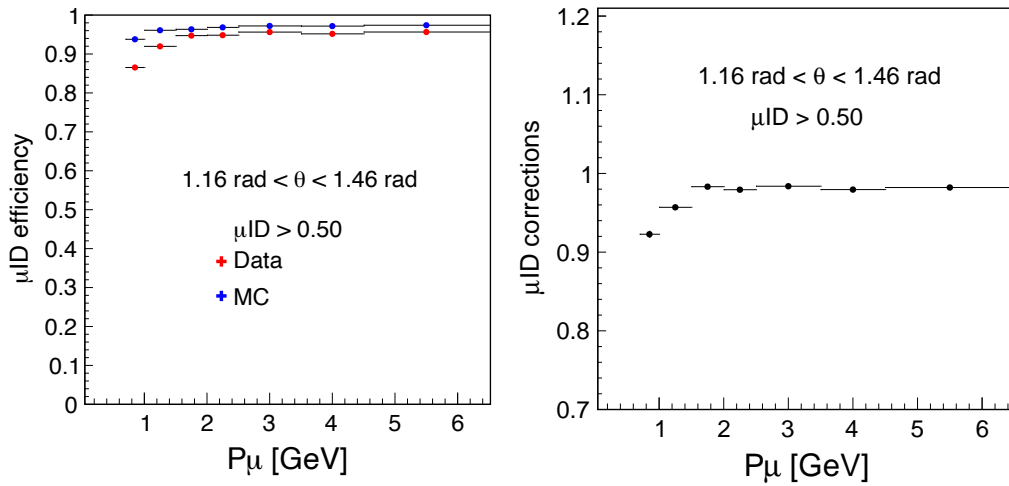


Figure 3.9: MuonID efficiency (left) and data-MC corrections (right) as a function of the momentum of tracks, for a specific BKLM region. Both plots refer to a muonID cut of 0.5.

(left) and the correction values (right) as a function of the momentum, for a specific region of the BKLM, are displayed. In both cases,  $\mu\text{ID} > 0.5$

is required. In the BKLM-EKLM separation regions, both efficiency and data-MC discrepancy worsen (see Fig. 3.10). This KLM area is not well instrumented and performances can hardly be improved.

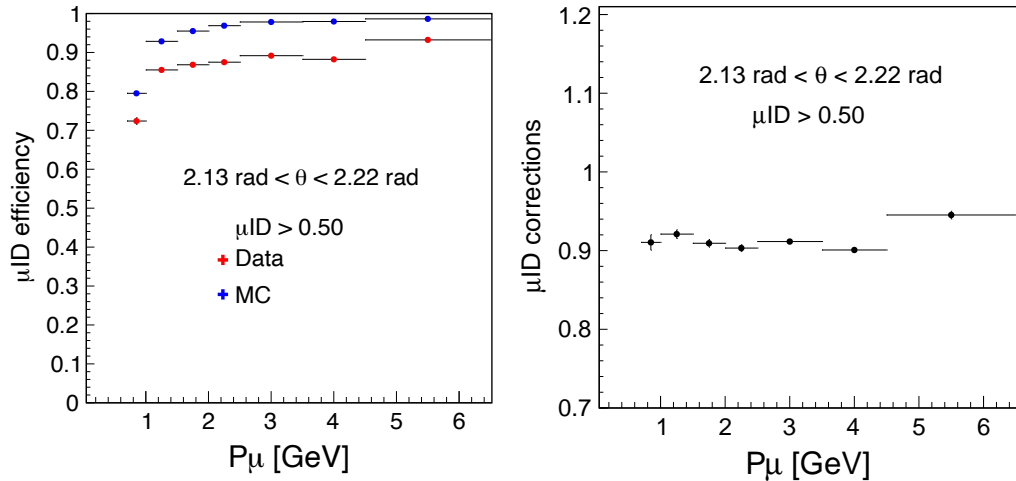


Figure 3.10: MuonID efficiency (left) and data-MC corrections (right) as a function of the momentum of tracks, for a specific EKLM-BKLM separation region in the backward side. Both plots refer to a muonID cut of 0.5.

Efficiencies appear to be more stable elsewhere with the exception of the EKLM sectors, where layer efficiencies are smaller (see Fig. 3.11).

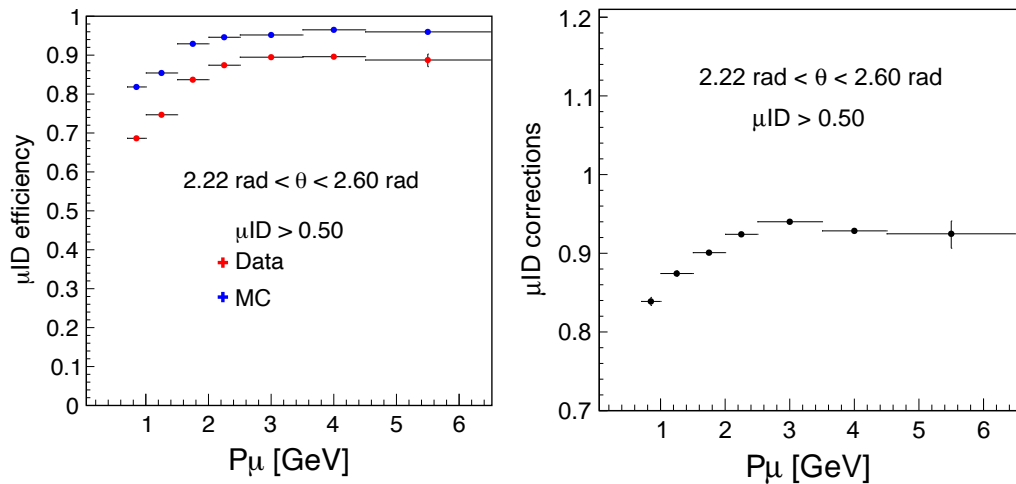


Figure 3.11: MuonID efficiency (left) and data-MC corrections (right) as a function of the momentum of tracks, for a specific EKLM region. Both plots refer to a muonID cut of 0.5.

Moreover, a not optimal modelling of B-field can contribute to the data-MC disagreement. This hypothesis is under study and will be addressed in the future by the KLM group.

The MC sample used in this study does not take into account realistic KLM efficiencies: values are set to 1 by default. The muonID algorithm takes care of the inefficient layers: no large effects with respect to the ideal conditions are expected but the discrepancies can be important if KLM detector is very inefficient.

### 3.3 Mis-identification rate from hadrons

Mis-identification rates should also be evaluated. The hadronic contribution is dominant and the focus is mostly on  $\pi \rightarrow \mu$  contamination. One of the main results come from the  $\tau \rightarrow 3\pi\nu_\tau$ , which provides a pure pion sample. The mis-ID rate is studied using a tag and probe method and the efficiency is estimated from the formula as in Eq. 3.5. Results show a  $\pi \rightarrow \mu$  mis-ID rate of the order of 5% for tracks with  $p > 1$  GeV, while it goes up to 30% for tracks with momentum below 0.7 GeV (see Fig. 3.12).

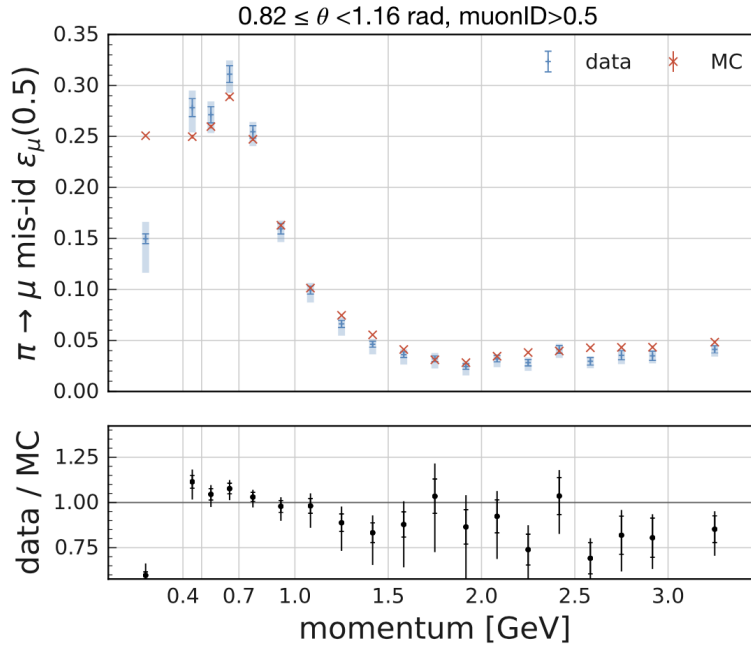


Figure 3.12: Data and MC mis-ID rates comparison as a function of the momentum of tracks, relatively to a part of the BKLM region. The plot refers to the  $\tau \rightarrow 3\pi\nu_\tau$  channel and a muonID cut of 0.5.

The  $\pi \rightarrow \mu$  mis-ID data-MC discrepancies, in bins of momentum and polar angle, were provided: such corrections will be used in the analysis of  $\tau \rightarrow 3\mu$  decay (see Chap. 4), since the kinematics of the two decays are similar. The pionID efficiency corrections were also estimated and used in the studies of systematics.

# Chapter 4

## Analysis strategy of the $\tau^\pm \rightarrow \mu^\pm \mu^\mp \mu^\pm$ decay

The decay channel studied in this thesis is one of the two golden channels, together with  $\tau \rightarrow l\gamma$ , in the context of the LFV studies in the  $\tau$  sector. At present, several measurements of  $\tau^\pm \rightarrow \mu^\pm \mu^\mp \mu^\pm$  [34],[35],[36],[53],[54],[55] were already performed and no signal events were observed. From these analysis, upper limit estimations of the BF were provided. This thesis work aims to perform the measurement following an optimised approach, different from the one used by the BaBar and Belle experiments. The work follows a blinded strategy: the analyser can not look directly at the data in the signal sensitive region before having validated the MC with a data-set that best approximate the signal.

Once the *BelleII* experiment will have collected an amount of statistics similar to Belle and BaBar, the new proposed method would provide a better limit estimation in the hypotheses of 0 observed event.

This chapter describes the analysis strategy, from the data-set selection to the optimisation procedure used to perform the measurement.

### 4.1 Analysis strategy in short

The analysis data-set consists of tau3x1 ( $\tau_{\text{sig}}[\rightarrow 3\mu]$   $\tau_{\text{tag}}[\rightarrow 1\text{prong}]$ ) events selected with initial pre-selection cuts (see Sec. 4.2). Events are split into two hemispheres: signal side and tag side. Events are further restricted in a signal region, defined in the  $M_{3\mu}$  and  $\Delta E_{3\mu} = E_{3\mu} - E_{\text{beam}}$  plane (see Sec. 4.2.2). Thereafter several variables were chosen for an optimisation procedure, divided in two main steps, in order to further reduce the

background contributions inside the signal region. The variables considered are:  $M_{\tau_{tag}}$ ,  $\Delta E_{\tau_{tag}}$ , Thrust and muonID (see Sec. 4.3.1). The most discriminating one is the muonID associated to the three muons coming from the signal decay of one  $\tau$ , that was optimised with a special treatment. The latter consists in defining three different momentum ranges for each track, reflecting the muonID performances. Tracks falling into distinct momentum regions are subject to different selections: three different cuts are thus used (see Sec. 4.3.2). The first step of the optimisation process consists in varying the muonID cut values, within certain intervals, with pre-defined steps. For each combination of cuts, the Punzi figure of merit was calculated and the combination corresponding to the maximum value was chosen. For this first step, the remaining variables were used to loosely constraint the sample, so that figure of merit maximisation is not entirely done on the muonID. The second optimisation step consist in fixing the optimised cuts on the muonID and let the remaining variables vary within pre-determined intervals. The best combination, according to the Punzi figure of merit, is chosen (see Sec. 4.3.3). Moreover, additional hand made selections are applied using many other variables. These cuts are chosen by looking at the signal distribution only, with the intent of keeping the efficiency up to  $\sim 90\%$  (see Sec. 4.3.4). The optimised cuts were applied to a different statistically uncorrelated data-set; both the efficiency and the number of survived background events were extracted and used later on for the limit estimation.

A systematic study were also performed using the control sample  $e^+e^- \rightarrow \tau[\rightarrow 3\pi\nu_\tau] \tau[\rightarrow 1prong]$  (see Chap. 5). Different procedures were used for signal and background. For the former, the systematic sources were investigated singularly and it emerged that the tracking efficiency and the muonID provide the highest contributions. For the latter, an inclusive approach was pursued. Before proceeding with the un-blinding of the data in the signal region, an additional test on the side-bands was done, in order to check the number of data and MC events surviving the analysis selections (see Sec. 6.1.1). Thereafter, the selection was applied on the final data-set inside the signal region (see Sec. 6.1.2). The number of observed events was then used to extrapolate the upper limit on the BF of the  $\tau^\pm \rightarrow \mu^\pm \mu^\mp \mu^\pm$  decay (see Sec. 6.3). This is done using a Bayesian procedure, numerically implemented with the BAT software that manages the statistical and systematic uncertainties on the key parameters entering the calculation (see Sec. 6.2.1).

## 4.2 Data-set description

A MC sample of  $e^+e^- \rightarrow \tau[\rightarrow 3\mu] \tau[\rightarrow 1prong]$  was used since the  $\tau \rightarrow 1prong$  process has the highest BF ( $\sim 85\%$ ) among the possible  $\tau$  decay channels. The decay topology with 1 prong coming from a  $\tau$  and 3 prongs from the other one is, from now on, defined as tau3x1. The total number of tracks in the event is therefore four, making the sample cleaner with respect, for example, to the six track case where contamination from  $q\bar{q}$  events would become important. From now on, the  $\tau$  decaying into  $3\mu$  will be denoted as  $\tau_{sig}$  while the  $\tau$  decaying into 1 prong will be  $\tau_{tag}$ .

A signal data-set of 200K events, produced with KKMC and Pythia [48] generators, was used. The sample is generated with no assumptions on the decay kinematics, thus the final state particles are produced according to pure phase space distributions. The analysis is conducted as a model independent search in order to have a generic result used to constrain any of the theoretical models described in Chap. 1 Sec. 1.1.2.2.

The MC background samples can be divided in three main categories:

- Continuum events:  $u\bar{u}$ ,  $d\bar{d}$ ,  $c\bar{c}$  and  $s\bar{s}$ . The equivalent of  $5 \text{ ab}^{-1}$  integrated luminosity is used;
- Tau-pair events:  $\tau^+\tau^-$ . The equivalent of  $5 \text{ ab}^{-1}$  integrated luminosity is used;
- Low multiplicity samples:  $4\mu$ ,  $ee\mu\mu$  and  $\mu\mu\gamma$ . The equivalent integrated luminosities of  $5 \text{ ab}^{-1}$  for the former and  $1 \text{ ab}^{-1}$  for the remaining two sources are used.

Events are weighted according to the integrated luminosities.

### 4.2.1 Event reconstruction criteria

Events are reconstructed, as represented in Fig.4.1, requiring the following pre-selection cuts:

- Exactly 4 tracks in the event coming from the proximity of the IP. These are selected through  $dz$ , which is the longitudinal signed distance, and  $dr$ , which is the distance in the  $r-\phi$  plane between the origin (simulated fixed position of the IP) and Point Of Closest Approach (POCA) of the track. In detail:  $-3.0 \text{ cm} < dz < 3.0 \text{ cm}$  and  $dr < 1.0 \text{ cm}$ ;
- Both  $\tau$  pointing to opposite hemispheres: the cosine of the polar angle between the thrust and each of the candidates ( $\cos ToThrust_{candidate}$ )

is introduced so that  $\cos\text{ToThrust}_{\tau_{sig}^{cand}} \cdot \cos\text{ToThrust}_{\tau_{tag}^{cand}} < 0$  where  $\tau_{sig}^{cand}$  and  $\tau_{tag}^{cand}$  are the signal side and tag side  $\tau$  candidate respectively;

- Signal side tracks identified as muons with  $\text{muonID} > 0.5$ ;
- Photons pointing inside the ECL acceptance:  $-0.8660 < \cos\theta_\gamma < 0.9563$ , with energy  $E_\gamma > 0.2$  GeV and number of hits per cluster  $> 1.5$ .
- Neutral pions are reconstructed from pair of photons with invariant mass within  $0.115 \text{ GeV} < M_{\gamma\gamma} < 0.152 \text{ GeV}$ . The photons used to reconstruct the  $\pi^0$  are defined as the photons in the previous item, but with an energy cut set at 100 MeV. Photons associated to a  $\pi^0$  are removed from the previous list.

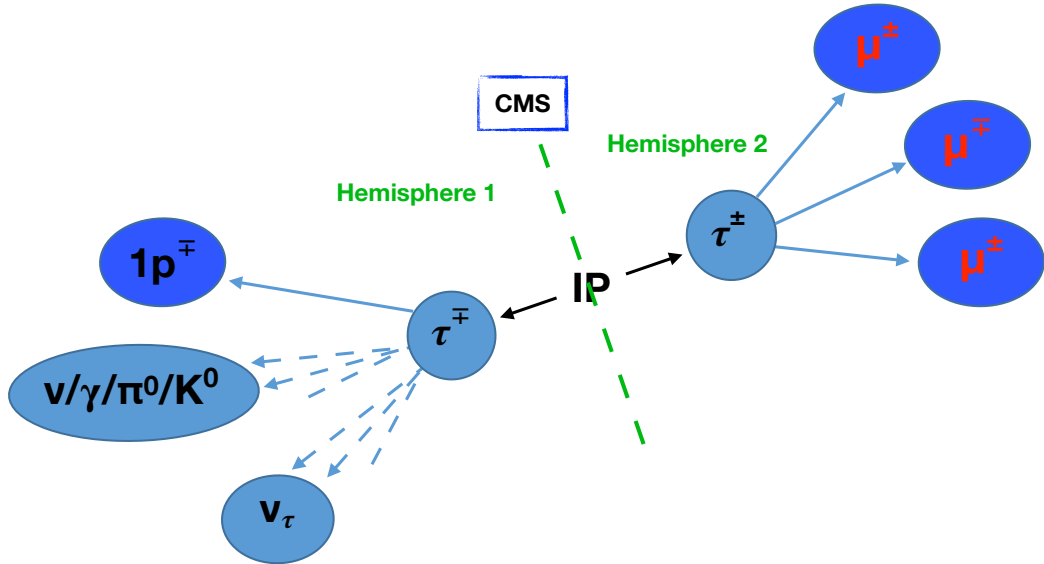


Figure 4.1: Event selection scheme overview. The two taus point to opposite directions: one is decaying into 3 muons and the other into 1prong. Tracks are coming from the IP region.

Two different tag side track cases are used, relying on PID requirements. The hadronic tag case is identified by  $\text{hadronID} > 0.5$ , where  $\text{hadronID} = 1 - \text{electronID} - \text{muonID}$ , while the leptonic tag case is identified by  $(\text{electronID} \text{ or } \text{muonID}) > 0.5$ . Different systematic studies, depending on the three tag cases (electron, muon and pion), are performed as described in Chap. 5.

### 4.2.2 Signal region definition

The signal region was defined using  $\Delta E_{3\mu} = E_{3\mu} - E_{beam}$  and  $M_{3\mu}$  (invariant mass of the 3 muon system) variables. The signal side kinematics is closed since no neutrinos are expected to be produced: the energy and mass of the  $\tau_{sig}$  are well defined. These variables are particularly convenient since they can well discriminate the LFV channels from all the SM processes, where neutrinos are always present.

#### 4.2.2.1 $M_{3\mu}$ and $\Delta E_{3\mu}$ correlation study

As visible from Fig.4.3,  $\Delta E_{3\mu}$  and  $M_{3\mu}$  are correlated: they can be de-correlated, providing a better signal region definition, with a rotation (as in Eq. 4.1).

$$\begin{pmatrix} M'_{3\mu} \\ \Delta E'_{3\mu} \end{pmatrix} = \begin{pmatrix} \cos\theta & \sin\theta \\ -\sin\theta & \cos\theta \end{pmatrix} \begin{pmatrix} M_{3\mu} \\ \Delta E_{3\mu} \end{pmatrix} \quad (4.1)$$

The angle  $\theta$  is found to be  $76.69^\circ$  (1.34 rad), extracted from the Y profile distribution of the 2-D graph in Fig. 4.3 left. As shown in Fig. 4.2, a linear fit is performed to extract the  $\theta$  rotation angle in the region where most of the statistics is present:  $-0.01 \text{ GeV} < \Delta E_{3\mu} < 0.01 \text{ GeV}$ . The choice of

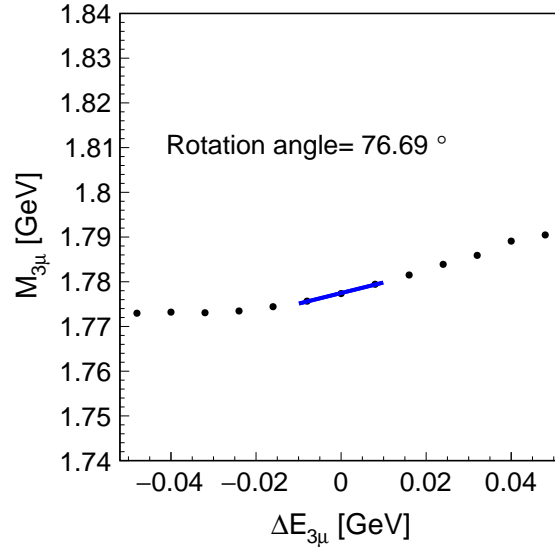


Figure 4.2:  $M_{3\mu}$  and  $\Delta E_{3\mu}$  correlation plot. The correlation angle is extracted from the poll fit (blue line).

this interval is not crucial since it is used to define the signal region, which represents the starting point of the analysis. The new rotated variables are  $M'_{3\mu}$  and  $\Delta E'_{3\mu}$  and their de-correlated distribution is reported in Fig 4.3 right. The long tilted component corresponds to the tail in the original  $\Delta E_{3\mu}$  distribution, as a consequence of the fact that the rotation is fitted in the signal region only.

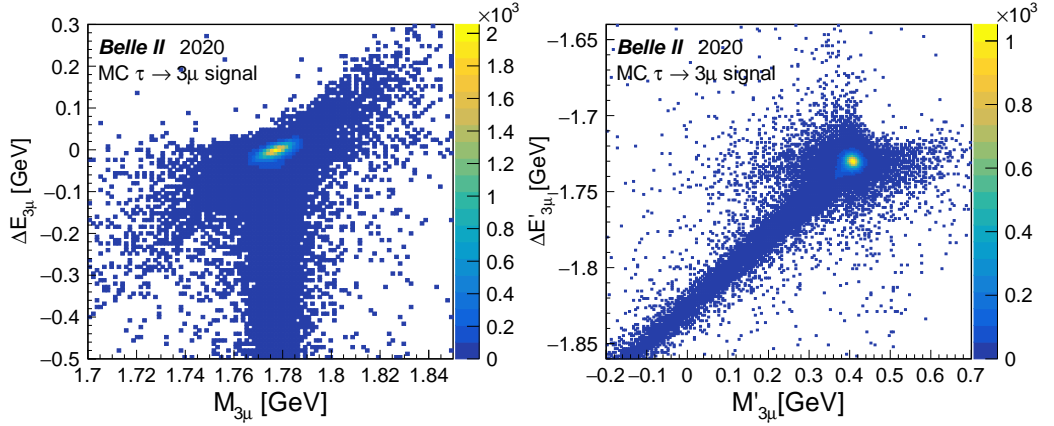


Figure 4.3: On the left, the  $M_{3\mu}$ - $\Delta E_{3\mu}$  2D plot is shown to underline the correlation. On the right, the same plot with de-correlated variables is reported.

#### 4.2.2.2 $M_{3\mu}$ and $\Delta E_{3\mu}$ fit

In order to define the signal region, independent fits of  $M'_{3\mu}$  and  $\Delta E'_{3\mu}$  were performed and the corresponding widths used as reference. For both fits, two Cristal-Ball (CB) and one Gaussian functions were used. Results are shown in Fig.4.4, where the CBs are displayed in blue (both shares the same mean but one has a right tail while the other has a left tail), the Gaussian in green and the total fit function in red. The total  $\sigma$  value overlaid in the figure comes from the weighted average of the single  $\sigma$ s with the number of events underneath each function.

The signal region is chosen to be a window within  $\pm 3\sigma$  around the central values of  $M'_{3\mu}$  and  $\Delta E'_{3\mu}$  (the dashed pink lines identify these boundaries):  $0.449 < M'_{3\mu} < 0.369$  and  $-1.719 < \Delta E'_{3\mu} < -1.740$ .

This definition is the starting point of the analysis: all the following studies were done inside this region, if not stated otherwise.

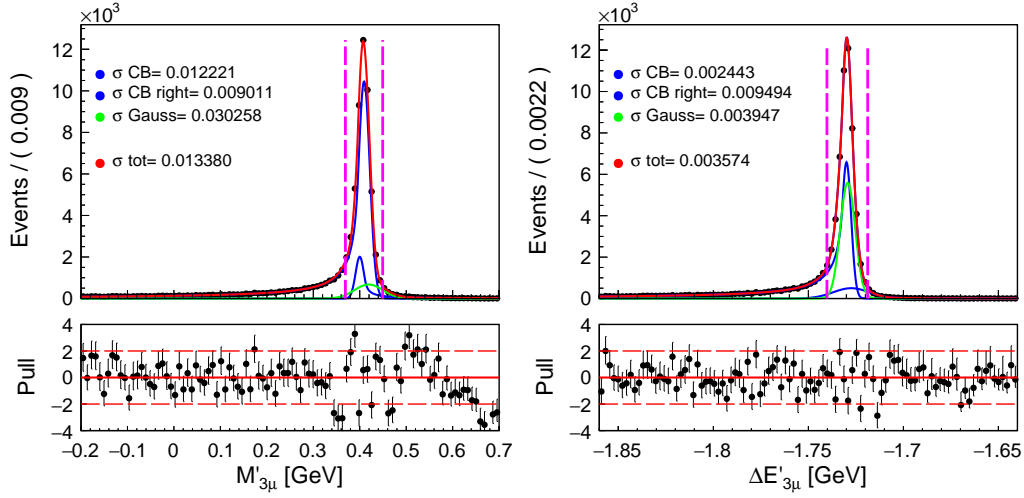


Figure 4.4: On the left (right) the fit on  $M_{3\mu}$  ( $\Delta E'_{3\mu}$ ) is reported. The 2 CB functions are in blue, the Gaussian in green and the total fit in red. The dashed pink lines represent the  $3\sigma$  interval around the mean. The pulls are shown at the bottom of the plots, where the dashed red lines represent the boundaries at  $\pm 2$  while the solid line indicates the null value.

## 4.3 Background rejection

The most important part of the analysis is the background suppression: the choice of the most signal-background discriminant variables is crucial. As shown in Fig.4.5 a small amount of background events enter the signal region area: these are the hardest to reject.

The idea is to reduce the contamination as much as possible in order to have an expected number of events close to 0. Even few events would cause large statistical uncertainties in the final results.

### 4.3.1 Discriminating variable description

In order to reduce the majority of the background contributions, the following variables were considered and optimized specifically:

- $M_{\tau_{tag}}$ : this mass is defined taking into account tracks and neutral clusters associated to the  $\tau_{tag}$ ;
- $\Delta E_{\tau_{tag}}$ : this is defined as  $E_{\tau_{tag}} - E_{beam}$ ;

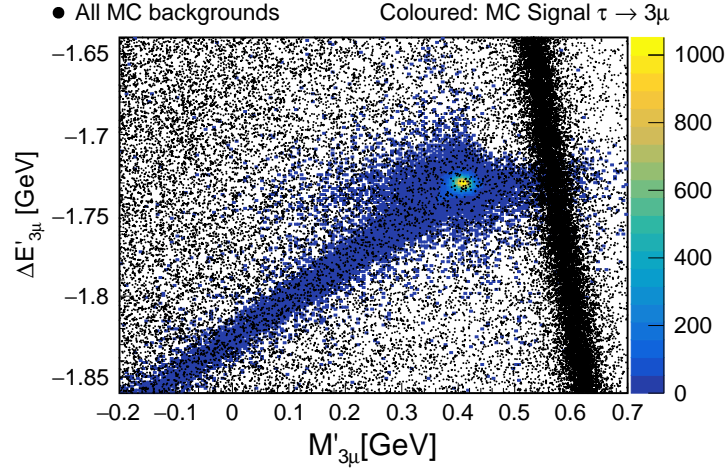


Figure 4.5:  $\Delta E'_{3\mu} - M'_{3\mu}$  scatter plot for signal (coloured points) and background (black dots) MC.

- Thrust: the thrust value is calculated from the thrust axis  $\hat{n}_{thrust}$  which is defined such that the Thrust value is maximized:

$$\text{Thrust} = \sum_i^{\#tracks} \frac{|\vec{p}_i^{CMS} \cdot \hat{n}_{thrust}|}{\sum_i^{\#tracks} p_i^{CMS}} \quad (4.2)$$

where  $\vec{p}_i^{CMS}$  is the momentum in the CMS of the  $i^{th}$  track in the event. In the CMS the decay products of the two  $\tau$ s are well separated in two opposite hemispheres defined by the plane perpendicular to the thrust axis. Thrust is computed considering the pion mass hypothesis for all the 4 tracks in the event;

- muonID: this is described more in detail in Sec. 4.3.2.

Two different samples were considered (see Sec.4.2.1): leptonic tag case and hadronic tag case. This is an important differentiation since some of the variables, and consequently the selections based on them, can change a lot between the two cases. The distributions of most of the discriminating variables, for signal and background, are reported in Fig.4.6 and several others in Fig.4.7.

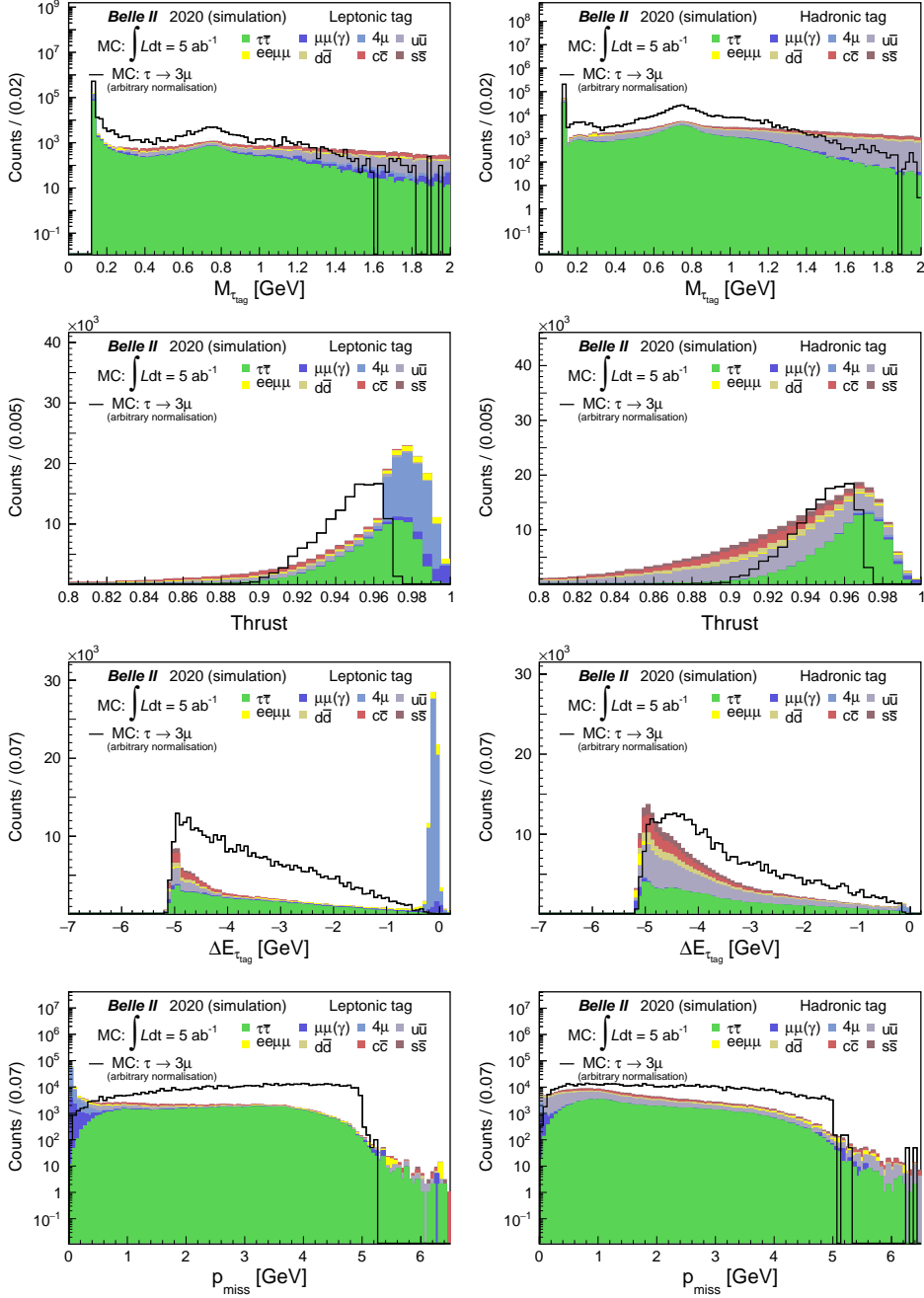


Figure 4.6: On the left (right) starting from the top there are the distributions of  $M_{\tau_{tag}}$ , Thrust,  $\Delta E_{\tau_{tag}}$  and  $p_{miss}$  for the leptonic (hadronic) tag case.

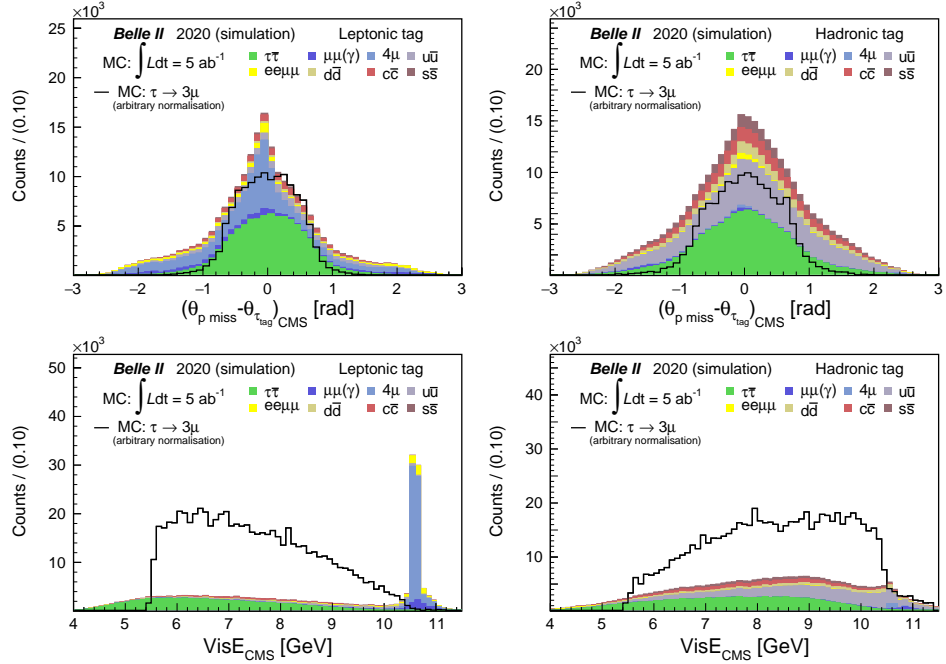


Figure 4.7: On the left (right) starting from the top there are the distributions of  $(\theta_{p_{miss}} - \theta_{\tau_{tag}})_{CMS}$  and  $VisE^{CMS}$  for the leptonic (hadronic) tag case.

### 4.3.2 MuonID optimisation procedure

A special treatment was devised for the optimisation of the muon identification selection. Since the performances depend a lot on the track momentum (see Fig.3.1), different cuts are provided for different momentum ranges. The KLM detector participates to muonID performances with the dominant contribution: momentum ranges are chosen according to the following considerations:

- $p_\mu < 0.7$  GeV. Tracks do not reach KLM and the muon identification has the lowest performances;
- $0.7$  GeV  $< p_\mu < 1.0$  GeV. Tracks do reach KLM, but cross only few layers, and a small amount of information is provided. Performances are not yet optimal;
- $p_\mu > 1.0$  GeV. Tracks do reach KLM and many layers are crossed. The best performances are achieved.

### 4.3.3 Analysis optimisation procedure

After applying the signal region selection (see Sec. 4.2.2), a cut based optimisation procedure was setup, by maximising a well defined Figure Of Merit (FOM). For this specific case, the Punzi FOM [56] is used:

$$FOM_{Punzi} = \frac{\varepsilon_{sig}}{\alpha/2 + \sqrt{N_{BKG}}} \quad (4.3)$$

where  $\varepsilon_{sig}$  is the total signal efficiency of the final selection,  $\alpha$  is a constant to be chosen according to the desire level of exclusion and  $N_{BKG}$  is the number of background events that survived the selection:  $\alpha=1.64$  was chosen, corresponding to 90% CL. This FOM is very useful if the cross section of the studied process is not known.

The optimisation is done by independently varying the values of the cuts within pre-determined intervals, and building the Punzi FOM for each combination of cuts. The intervals are chosen accordingly to the distributions in Fig. 4.6, with the goal of keeping a high signal retention. The corresponding values are reported in Tab. 4.1.

Table 4.1: Summary table of the intervals used during the optimisation procedure.

Interval	$M_{\tau_{tag}}$	$\Delta E_{\tau_{tag}}$	Thrust	muonID
Lower limit	1.30	-0.80	0.960	0.5
Upper limit	1.52	-0.20	0.982	0.95
Number of steps	12	12	11	10
Value of each step	0.02 GeV	0.05 GeV	0.02	0.05

The optimisation procedure is performed for leptonic and hadronic tag cases separately, in two steps; first, only the muonID is optimised, while loose cuts are applied on the remaining 4 variables, see Tab.4.2. The 3 muonID cut values are extracted and applied.

Table 4.2: Initialisation value for Thrust,  $M_{\tau_{tag}}$  and  $\Delta E_{\tau_{tag}}$  used in the first optimisation step.

Tag case	Thrust	$M_{\tau_{tag}}$ [GeV]	$\Delta E_{\tau_{tag}}$ [GeV]
Leptonic	<0.98	<1.6	<-0.1
Hadronic	<0.98	<1.6	<-0.1

In the final step, the optimisation on the remaining 4 variables on the sample surviving the muonID selection is performed.

This strategy allows to let both muonID and the additional variables to play a role in the maximisation of the Punzi FOM. In fact, having one inclusive optimisation in one step would let the sample be constrained a lot by the most discriminant variables only. The stability of the method is checked by repeating the procedure on 4 different sub-samples, in bunches of  $2 \text{ ab}^{-1}$  (the total reference is  $5 \text{ ab}^{-1}$ ). These are defined as:  $1^{\text{st}}$  sample from 0 to  $2 \text{ ab}^{-1}$ ,  $2^{\text{nd}}$  sample from 1 to  $3 \text{ ab}^{-1}$ ,  $3^{\text{rd}}$  sample from 2 to  $4 \text{ ab}^{-1}$ ,  $4^{\text{th}}$  sample from 3 to  $5 \text{ ab}^{-1}$ . In this way, it is also possible to understand if the optimisation process, whose performances are determined by only a few background events, is affected by over-training effects. The 6 cut values are then obtained for the 4 different sub-samples and reported in Tab.4.3.

Table 4.3: Cut values obtained with the optimisation procedure where r1 refers to tracks with  $p < 0.7 \text{ GeV}$ , r2 to  $0.7 \text{ GeV} < p < 1.0 \text{ GeV}$  and r3 to  $p > 1 \text{ GeV}$ . The 4 sample used for the optimisations, from the top to the bottom, are defined as:  $1^{\text{st}}$  sample from 0 to  $2 \text{ ab}^{-1}$ ,  $2^{\text{nd}}$  sample from 1 to  $3 \text{ ab}^{-1}$ ,  $3^{\text{rd}}$  sample from 2 to  $4 \text{ ab}^{-1}$ ,  $4^{\text{th}}$  sample from 3 to  $5 \text{ ab}^{-1}$ . Leptonic and hadronic tag cases are displayed as Lep and Had.

$1^{\text{st}}$ sample	$\mu\text{ID r1}$	$\mu\text{ID r2}$	$\mu\text{ID r3}$	Thrust	$M_{\tau_{\text{tag}}}[\text{GeV}]$	$\Delta E_{\tau_{\text{tag}}}[\text{GeV}]$
Lep	$>0.90$	$>0.50$	$>0.65$	$<0.976$	$<1.52$	$<-0.25$
Had	$>0.75$	$>0.50$	$>0.95$	$<0.968$	$<1.52$	$<-0.35$
$2^{\text{nd}}$ sample	$\mu\text{ID r1}$	$\mu\text{ID r2}$	$\mu\text{ID r3}$	Thrust	$M_{\tau_{\text{tag}}}[\text{GeV}]$	$\Delta E_{\tau_{\text{tag}}}[\text{GeV}]$
Lep	$>0.90$	$>0.50$	$>0.65$	$<0.976$	$<1.52$	$<-0.25$
Had	$>0.75$	$>0.95$	$>0.70$	$<0.976$	$<1.52$	$<-0.25$
$3^{\text{rd}}$ sample	$\mu\text{ID r1}$	$\mu\text{ID r2}$	$\mu\text{ID r3}$	Thrust	$M_{\tau_{\text{tag}}}[\text{GeV}]$	$\Delta E_{\tau_{\text{tag}}}[\text{GeV}]$
Lep	$>0.50$	$>0.95$	$>0.65$	$<0.976$	$<1.52$	$<-0.25$
Had	$>0.70$	$>0.95$	$>0.75$	$<0.976$	$<1.38$	$<-0.25$
$4^{\text{th}}$ sample	$\mu\text{ID r1}$	$\mu\text{ID r2}$	$\mu\text{ID r3}$	Thrust	$M_{\tau_{\text{tag}}}[\text{GeV}]$	$\Delta E_{\tau_{\text{tag}}}[\text{GeV}]$
Lep	$>0.90$	$>0.50$	$>0.65$	$<0.962$	$<1.50$	$<-0.30$
Had	$>0.65$	$>0.50$	$>0.95$	$<0.980$	$<1.38$	$<-0.50$

The results show that there are some differences between the leptonic and the hadronic tag cases, as expected. The major source of difference concerns the muonID: for the hadronic tag sample the cuts are tighter as most of the background composition comes from  $q\bar{q}$  events, where a smaller amount of real muons (with respect to the leptonic tag case) is present. The only background events surviving the selections come from the hadronic tag case, more in detail from the  $u\bar{u}$  sample.

#### 4.3.4 Additional hand made selection

The MC signal distributions were checked after the application of the optimised cuts and, in addition, some hand made cuts were applied to have further control on the sample. The variables are:

- $M_{\text{miss}}^2$ : missing mass of the event. The signal sample is expected to have, in average, a missing mass closer to 0 with respect to the SM channels;
- $p_{\text{miss}}$ : missing momentum of the event. The signal sample is expected to have, in average, a missing momentum closer to 0 with respect to the SM channels;
- Track momentum: background events are populated, in average, by tracks with low momentum;
- $n_\gamma$  tag (sig) side: number of photons in the tag (sig) side. This is higher for the hadronic tag case with respect to the leptonic one due to physical background sources;
- $n_{\pi^0}$  tag (sig) side: number of  $\pi^0$  in the tag (sig) side. This quantity differs significantly between the leptonic and the hadronic tag cases. For the latter, there can be one or more  $\pi^0$  produced in association with the  $\pi^\pm$  from real physics processes;
- $(\theta_{p_{\text{miss}}} - \theta_{\tau_{\text{tag}}})_{\text{CMS}}$ : difference of the  $\theta$  angle in the CMS between the missing momentum and the tag side  $\tau$ . In signal events the missing momentum is expected to point to the tag side direction, due to the absence of neutrinos in the  $\tau^\pm \rightarrow \mu^\pm \mu^\mp \mu^\pm$  decay;
- Thrust (see Sec. 4.3.1): the optimisation process fixes a higher cut for this variable. Here the possibility to set a lower cut value is investigated;

- $\text{VisE}_{\text{CMS}}$ : visible energy in the CMS (charged plus neutral particles)  
This introduces not negligible differences between the leptonic and hadronic tag side cases. For the latter, there can be one or more  $\pi^0$  produced in association with the  $\pi^\pm$ , so enhancing  $\text{VisE}_{\text{CMS}}$ .

The cuts are chosen so that the final retention on signal is  $\sim 90\%$ . The remaining background at this stage is not displayed in order to avoid any biases introduced by the analyst. The distributions are shown in figures 4.8, 4.9, 4.10, 4.11. Here the chosen cuts are superimposed, while a summary list is given in Tab 4.4.

Table 4.4: List of the hand made cuts to be applied to the data-sample.

Variables:	Leptonic tag cuts	Hadronic tag cuts
$M_{\text{miss}}^2$ [ $\text{GeV}^2/c^4$ ]	$>-2.5$ AND $<3.0$	$>-3.0$ AND $<3.0$
$p_{1\text{prong}}$ [GeV]	$>0.1$	$>0.1$
$p_{\text{miss}}$ [GeV]	$>0.5$	$>0.3$
$p_{3\text{prong}}$ [GeV]	$>0.2$	$>0.2$
$n_\gamma$ tag	$<2$	$<3$
$n_\gamma$ sig	$<2$	$<2$
$n_{\pi^0}$ tag	$<2$	$<4$
$n_{\pi^0}$ sig	$<1$	$<1$
$(\theta_{p_{\text{miss}}} - \theta_{\tau_{\text{tag}}})_{\text{CMS}}$ [rad]	$>-1.3$ AND $<1.3$	$>-1.4$ AND $<1.3$
Thrust	$>0.89$	$>0.89$
$\text{VisibleE}_{\text{CMS}}$ [GeV]	$<9.6$	$<11$

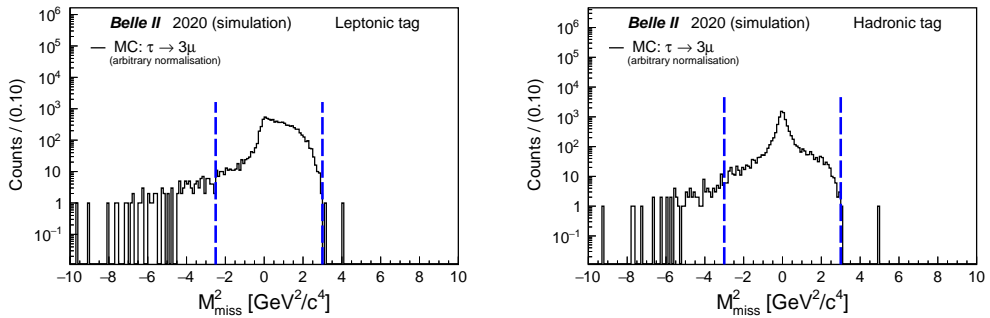


Figure 4.8: On the left (right) there is the distribution of  $M_{\text{miss}}^2$  for the leptonic (hadronic) tag case. The dashed blue lines indicate the hand made cuts chosen.

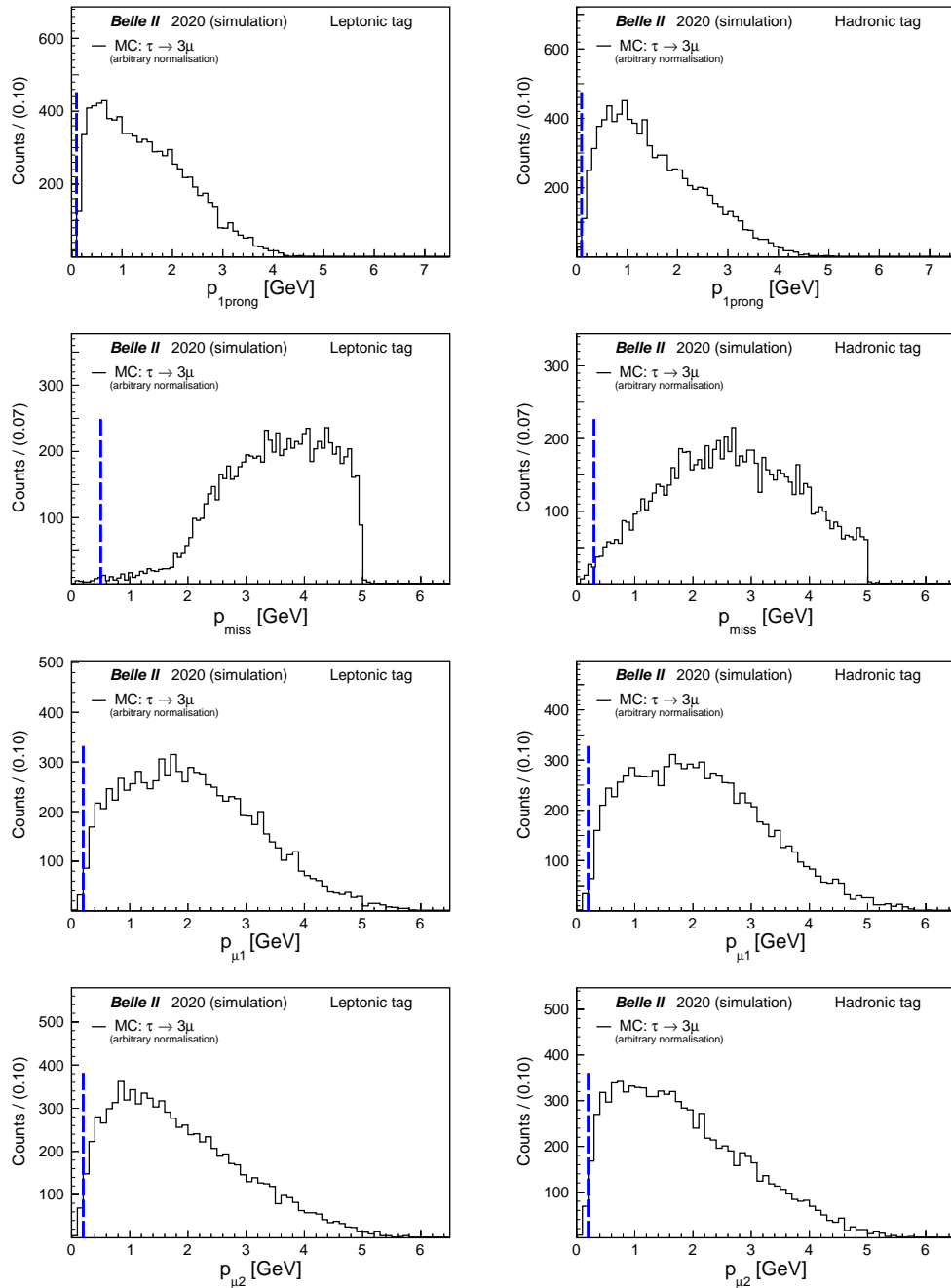


Figure 4.9: On the left (right) starting from the top there are the distributions of  $p$  of the track in tag side,  $p_{\text{miss}}$ ,  $p$  of track1 in sig side and  $p$  of track2 in sig side for the leptonic (hadronic) tag case. The dashed blue lines indicate the hand made cuts chosen.

68 CHAPTER 4. ANALYSIS STRATEGY OF THE  $\tau^\pm \rightarrow \mu^\pm \mu^\mp \mu^\pm$  DECAY

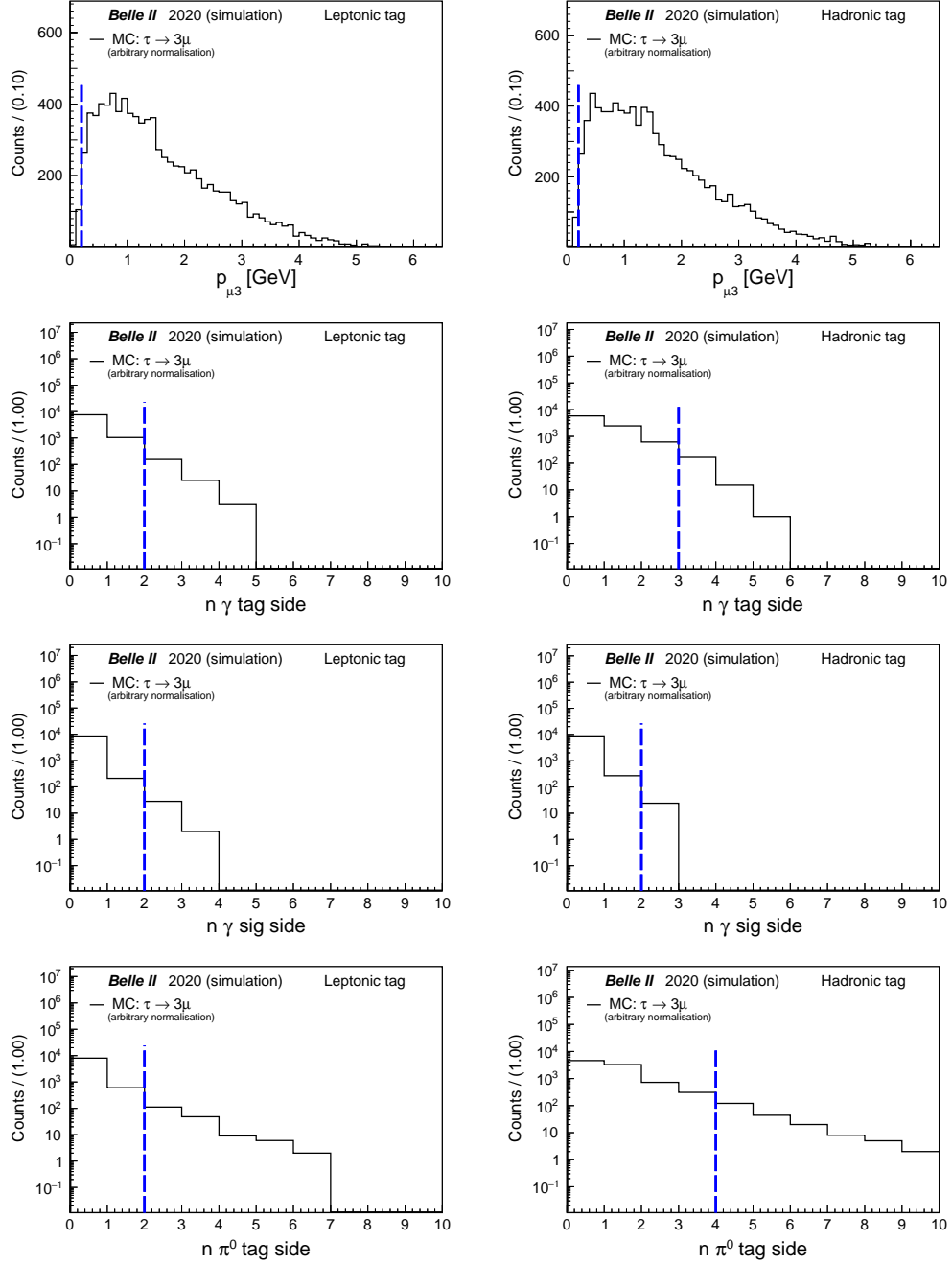


Figure 4.10: On the left (right) starting from the top there are the distributions of  $p$  of track3 in sig side,  $n_\gamma$  tag side,  $n_\gamma$  sig side and  $n_{\pi^0}$  tag side for the leptonic (hadronic) tag case. The dashed blue lines indicate the hand made cuts chosen.

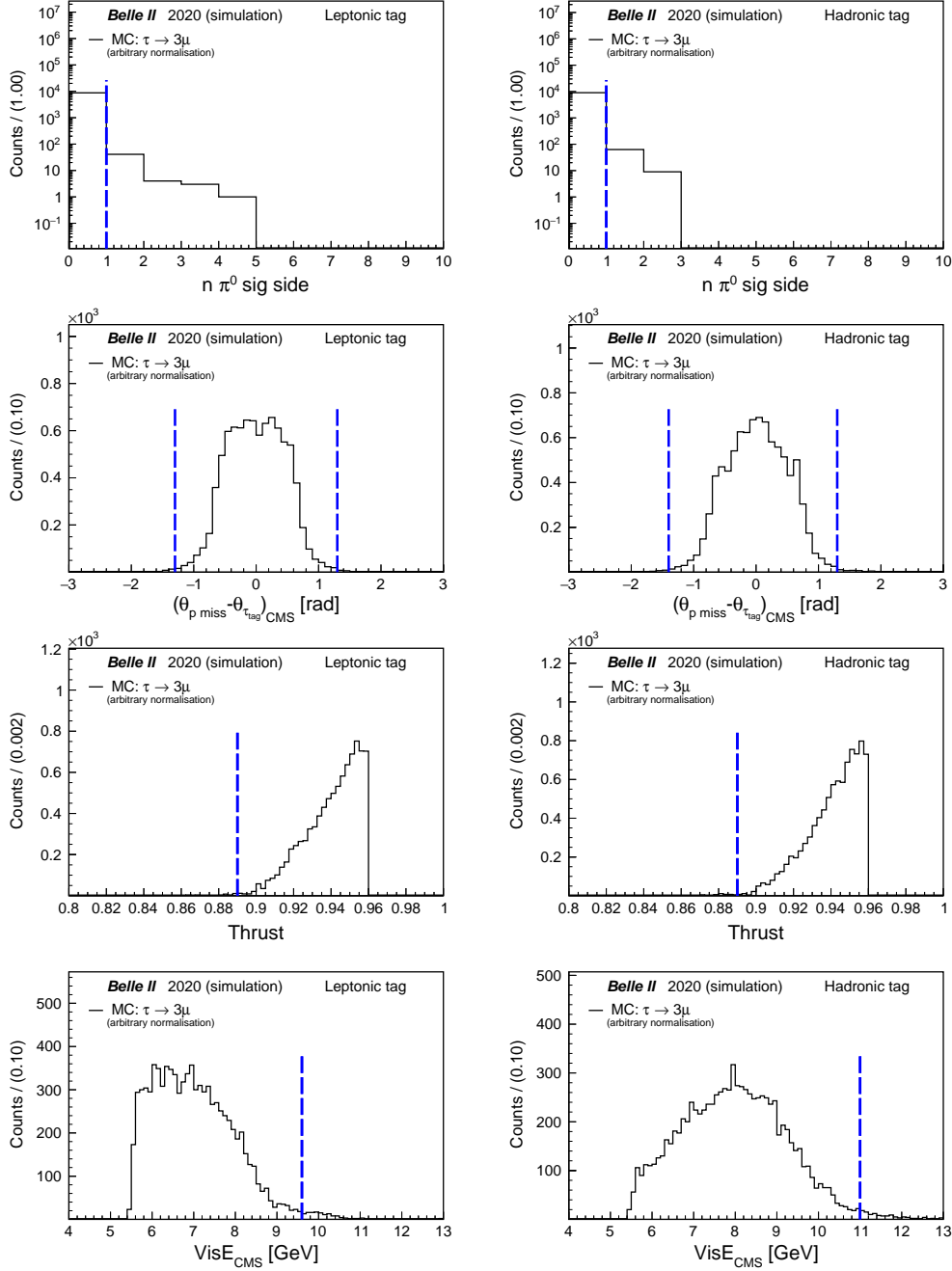


Figure 4.11: On the left (right) starting from the top there are the distributions of  $n_{\pi^0}$  sig side,  $(\theta_{p_{\text{miss}}} - \theta_{\tau_{\text{tag}}})_{\text{CMS}}$ , Thrust and VisibleE<sub>CMS</sub> for the leptonic (hadronic) tag case. The dashed blue lines indicate the hand made cuts chosen.

## 4.4 Analysis comparison with previous results

The presented analysis work can be directly compared with the ones performed by the BaBar and Belle experiments. Specifically for the muonID efficiency, results are slightly improved while some more development is needed for the muon mis-ID rate from hadrons.

The analysis strategy adopted is a major factor of improvement: the signal region has been chosen as a first step, so that the optimised cuts have been performed on a sample very similar to the signal. This served as a starting point of the optimisation process. The application of the muonID cuts has been improved a lot, since it is a crucial aspect of the analysis: the choice of using different cuts depending on the momentum of tracks allowed to enhance the efficiency selection.

The performances of the *BelleII* detector, reflecting for example on the tau mass and energy resolutions, are already comparable with the one from Belle and BaBar.

In Sec. 6.3 a brief description of further improvement is given.

# Chapter 5

## Data-MC corrections and evaluation of systematic uncertainties

In order to have reliable MC samples, correction factors should be applied to MC (and data) data-sets used in the analysis of  $\tau^\pm \rightarrow \mu^\pm \mu^\mp \mu^\pm$ . The study of the systematic effects was performed for the signal and the background separately. For the signal, the most important sources were considered singularly, while for the background an inclusive approach was followed.

The quantities more sensitive to data-MC discrepancies, for which detailed studies are necessary, are the trigger and the muonID. The muonID corrections are provided by the *BelleII* leptonID group as a result of the study of several final states, as described in Chap.3. Corrections referring to a muonID cut of 0.5 are applied to tracks with  $\text{muonID} < 0.75$ , while corrections referring to a muonID cut of 0.9 are applied to tracks with  $\text{muonID} \geq 0.75$ . Efficiency corrections for the electronID and pionID were also applied, for tracks identified as electrons and pions respectively.

The combined results from the  $e^+e^- \rightarrow e^+e^-\mu^+\mu^-$ , four-lepton two-photon final states, (covering the low momentum spectrum) and the  $\mu\mu\gamma$  processes (covering the high momentum spectrum) were used. At the same time, mis-ID corrections should be applied: these are estimated from the  $\tau \rightarrow 3\pi\nu_\tau$  study.

The rest of the chapter describes the control sample used to estimate the systematics uncertainties for the background and the signal separately, and the most relevant triggers involved. Moreover, an overview of all the systematic sources is given together with the corresponding effects.

## 5.1 Control sample description

The evaluation of the systematic uncertainties for the  $\tau^\pm \rightarrow \mu^\pm \mu^\mp \mu^\pm$  was carried with the control channel  $\tau \rightarrow 3\pi\nu$  in the tau3x1 topology, using an integrated luminosity of  $34.6 \text{ fb}^{-1}$ . The same cuts as for the analysis (see Tab.4.4 and 4.3.3) were applied, with the exception of the muonID and the signal region requirements. The signal region was enlarged ( $-0.20 \text{ GeV} < M'_{3\mu} < 0.70 \text{ GeV}$  and  $-2.00 \text{ GeV} < \Delta E'_{3\mu} < -1.65 \text{ GeV}$ ) in order to have access to more statistics, while the muonID requirement on signal side tracks were replaced with pionID>0.5. The data-MC corrections for the pionID efficiency, provided by the *BelleII* collaboration, were implemented too. Hypothetical signal events entering the selection due to  $\mu \rightarrow \pi$  fake-rates are of the order of  $10^{-5}$  and thus considered negligible. A momentum scale factor is also applied to tracks in order to have a better agreement with MC (the value is provided by the *BelleII* collaboration).

## 5.2 Trigger definitions

The Level 1 trigger system was designed to cover a broad range of physics signatures 2.2.7. For the purpose of this work, three main categories are considered: CDC, ECL and KLM triggers.

The track reconstruction performed by the CDC triggers is based on the so-called track segments, which are produced by an algorithm at CDC super-layer level. The 2D tracks are identified in the  $r$ - $\phi$  space, through a Hough transformation [57], by combining track segments. Two different classes of tracks are defined: "full tracks" and "short tracks". The former are required to pass through all the axial super-layers in the barrel region. The latter pass through the first 5 super-layers and correspond to tracks that curl inside the CDC barrel volume or are in the endcap region. Short tracks at trigger level were introduced to improve the performances for low momentum particles and to enlarge the angular trigger acceptance.

The ECL trigger decision is based on cells of 4x4 crystals and provide the energy signature for both neutral and charged particles. Two approaches are taken into account by the *BelleII* trigger system, based on the total energy and on an isolated cluster counting. Additional lines are provided specifically for the low-multiplicity processes. The ECL is also used to select and eventually reject Bhabha events.

The KLM trigger lines are the most recent and are based on the hit information in KLM layers and the corresponding matching with the tracks found in the CDC.

The most relevant triggers for this analysis are defined as:

- Bhabha:  $165^\circ < \sum \theta_{CMS} < 190^\circ$ , where  $\sum \theta_{CMS}$  is sum of polar angles of 2 clusters in the CMS,  $160^\circ < \Delta\phi_{CMS} < 200^\circ$ , where  $\sum \phi_{CMS}$  is difference of phi angles of 2 clusters in the CMS, two ECL clusters with  $E_{CMS} > 3$  GeV and at least one with  $E_{CMS} > 4.5$  GeV;
- ffo:  $\geq 2$  full tracks, at least one track pair with  $\Delta\phi > 90^\circ$  and ECL Bhabha veto;
- fff:  $\geq 3$  full tracks;
- hie:  $> 1$  GeV total energy in ECL and Bhabha veto;
- lml0:  $\geq 3$  ECL clusters with at least one having  $E^* > 300$  MeV,  $12.4^\circ < \theta < 154.7^\circ$  (entire ECL coverage) and ECL Bhabha veto;
- lml12:  $\geq 3$  ECL clusters with at least one having  $E^* > 500$  MeV,  $18.5^\circ < \theta < 139.3^\circ$  and ECL Bhabha veto.
- cdcklmX, where X (from 1 to 4) is the number of CDC tracks matched with fired BKLM sectors. These are mutually exclusive lines thus, for instance, cdcklm1 corresponds to exactly one match. For cdcklm4 the number of tracks is equal or greater than 4. A BKLM sector is considered fired when at least eight layers have hits, not necessarily contiguous.

## 5.3 Signal systematics

The systematic sources considered for the  $\tau^\pm \rightarrow \mu^\pm \mu^\mp \mu^\pm$  signal are: beam energy shift, tracking efficiency, momentum resolution, trigger efficiency and muonID. All of them are investigated one by one in the following of this section.

### 5.3.1 Beam energy shift

For the beam energy shift an uncertainty of 1.5 MeV was considered, as it was for the Belle experiment. The preliminary value from the *BelleII* experiment are better, of the order of 0.5 MeV, but a conservative approach was preferred. The inclusion of this effect is done by summing and subtracting 1.5 MeV separately to the CM energy ( $\sqrt{s}/2$ ). In simulated events, the largest induced difference in the signal efficiency is estimated to be 0.03%, chosen as the systematic contribution associated to this source.

### 5.3.2 Tracking efficiency

The tracking efficiency is taken from an existing study within the *BelleII* collaboration where a per track discrepancy of the efficiency is found to be  $0.13 \pm 0.16(stat) \pm 0.89(syst)\%$ . Since exactly 4 tracks are required, losing even one track would cause the event to be discarded. For this reason, the data-MC efficiency correction has to be multiplied by 4 while the associated systematics uncertainty is propagated in quadrature 4 times, taking into account both statistic and systematic errors (as reported in Eq.5.1).

$$\text{syst} = \sqrt{4 \cdot (0.13^2 + 0.89^2)} \quad (5.1)$$

The final systematics is thus evaluated to be 1.80%, while the correction factor 0.52%.

### 5.3.3 Momentum resolution

The momentum resolution, specifically studied within the *BelleII* group, was provided as a function of momentum, being affected by a non negligible dependency. Based on those studies, the largest difference observed in the momentum spectrum is considered as a constant systematic uncertainty. The maximum contribution is quantified in  $\sigma_p/p = 0.3\%$ . In order to evaluate the impact on the signal efficiency, the momentum of the MC signal tracks was changed by summing and subtracting that contribution separately. The largest induced difference in the signal efficiency is the systematic uncertainty due to this source and evaluated to be 0.01%.

### 5.3.4 Trigger

The trigger efficiency can not be estimated directly from Monte Carlo since the trigger simulation is not accurate yet. The  $\tau \rightarrow 3\pi\nu_\tau$  control sample channel is used to estimate the efficiency of several trigger lines (see Sec. 5.2). The fff and lml0 turned out to be the most suitable for this analysis. The fff trigger efficiency ( $\varepsilon_{fff}$ ) is calculated using an orthogonal trigger as reference, hie, based on ECL:

$$\varepsilon_{fff} = \frac{\#hie \text{ and } \#fff}{\#hie} \quad (5.2)$$

where  $\#hie$  ( $\#fff$ ) is the number of events triggered by hie (fff). For the same reasons, the lml0 efficiency ( $\varepsilon_{lml0}$ ) is obtained using fff trigger as reference:

$$\varepsilon_{lml0} = \frac{\#fff \text{ and } \#lml0}{\#fff} \quad (5.3)$$

Their efficiencies, as a function of  $\Delta E$ , are shown in Fig.5.1, for the three different tag cases: electron, muon and pion (identified by  $\text{electronID} > 0.5$ ,

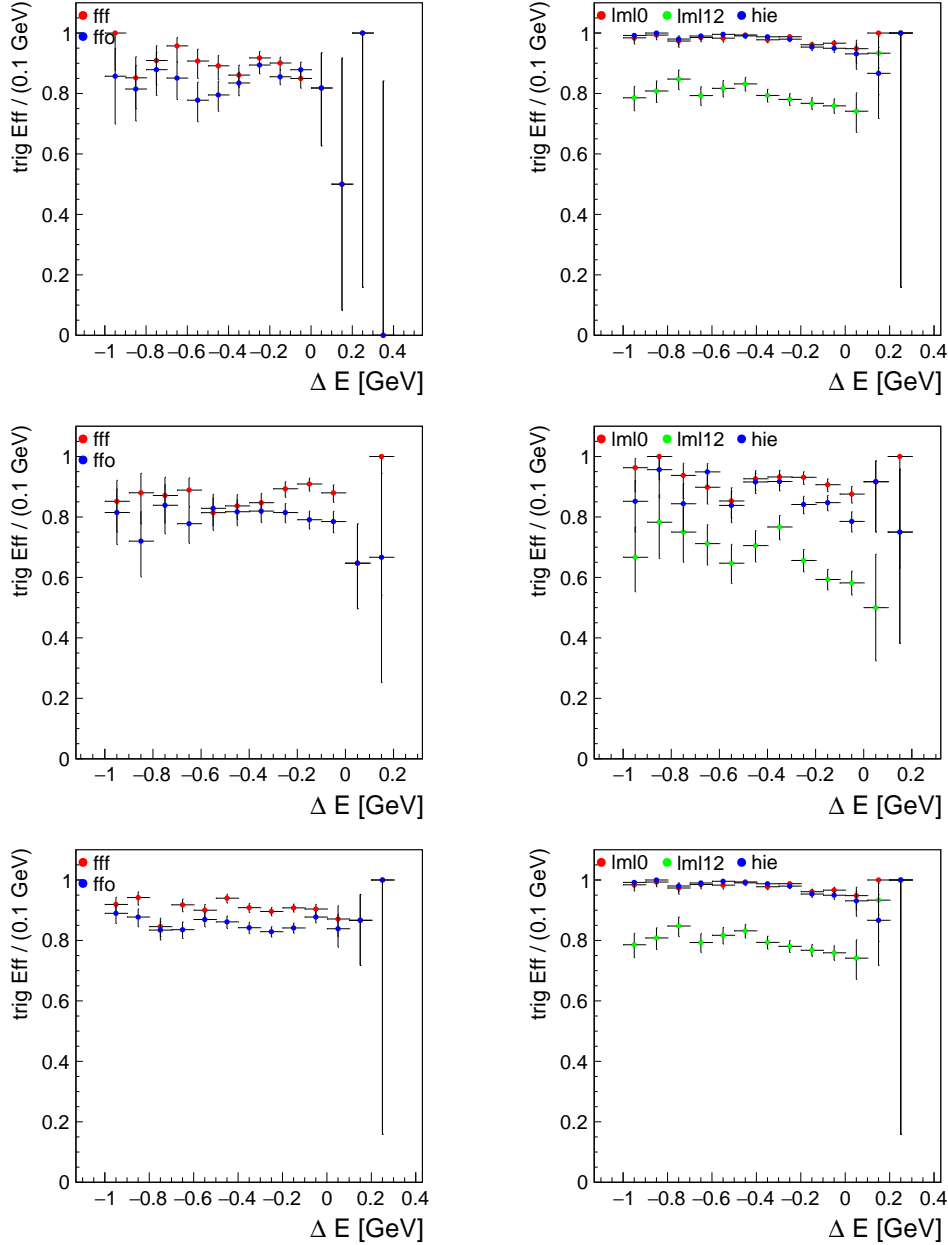


Figure 5.1: Trigger efficiencies of fff, ffo (left column) and hie, lml0, lml12 (right column) upon  $\Delta E$  for the electron (top), muon (middle) and pion (bottom) tag track cases.

muonID>0.5 and pionID>0.5 respectively). The efficiencies of lml0 and fff are extracted with a pol0 fit (see Fig. 5.2, 5.3) on these distributions, since they are considered flat in the signal region ( $\Delta E$  close to 0). The associated systematic error would be therefore the error of the fit.

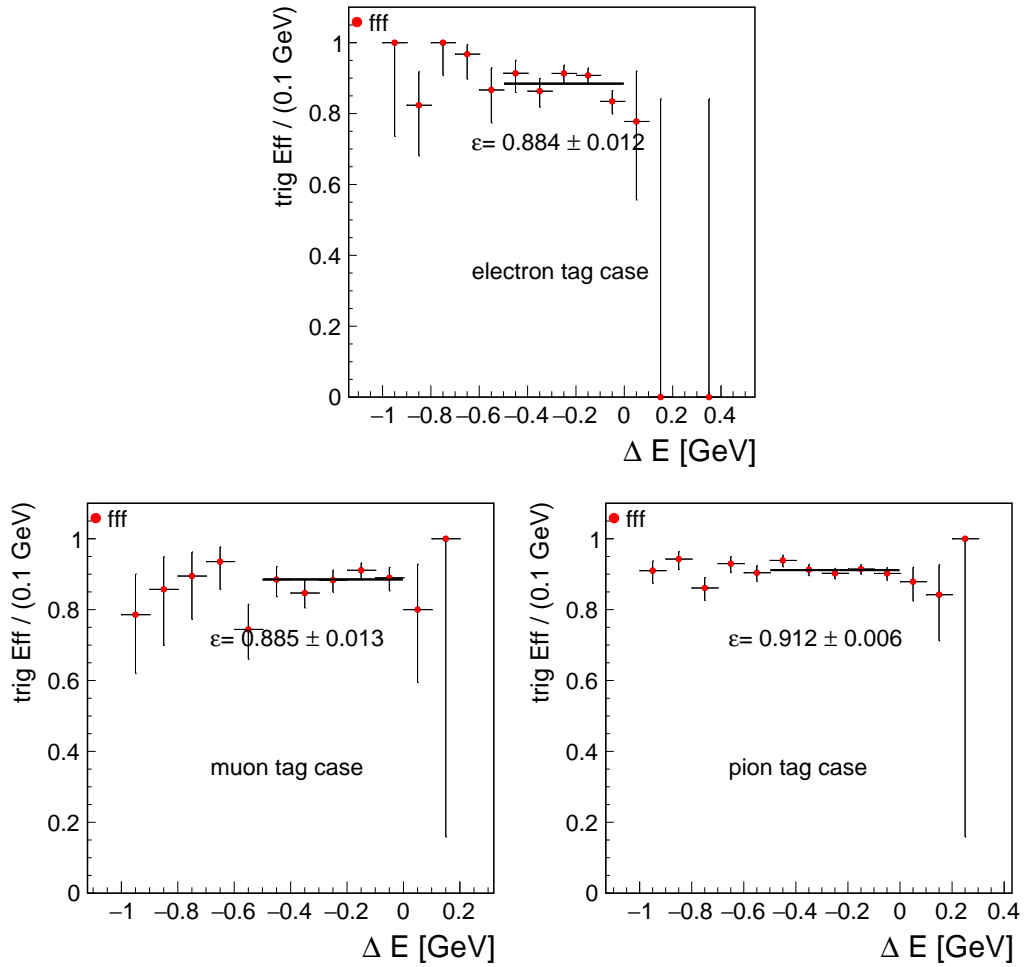


Figure 5.2: Trigger efficiency of fff as a function of  $\Delta E$ . On top the electron case, on bottom left the muon case and on bottom right the pion case are displayed.

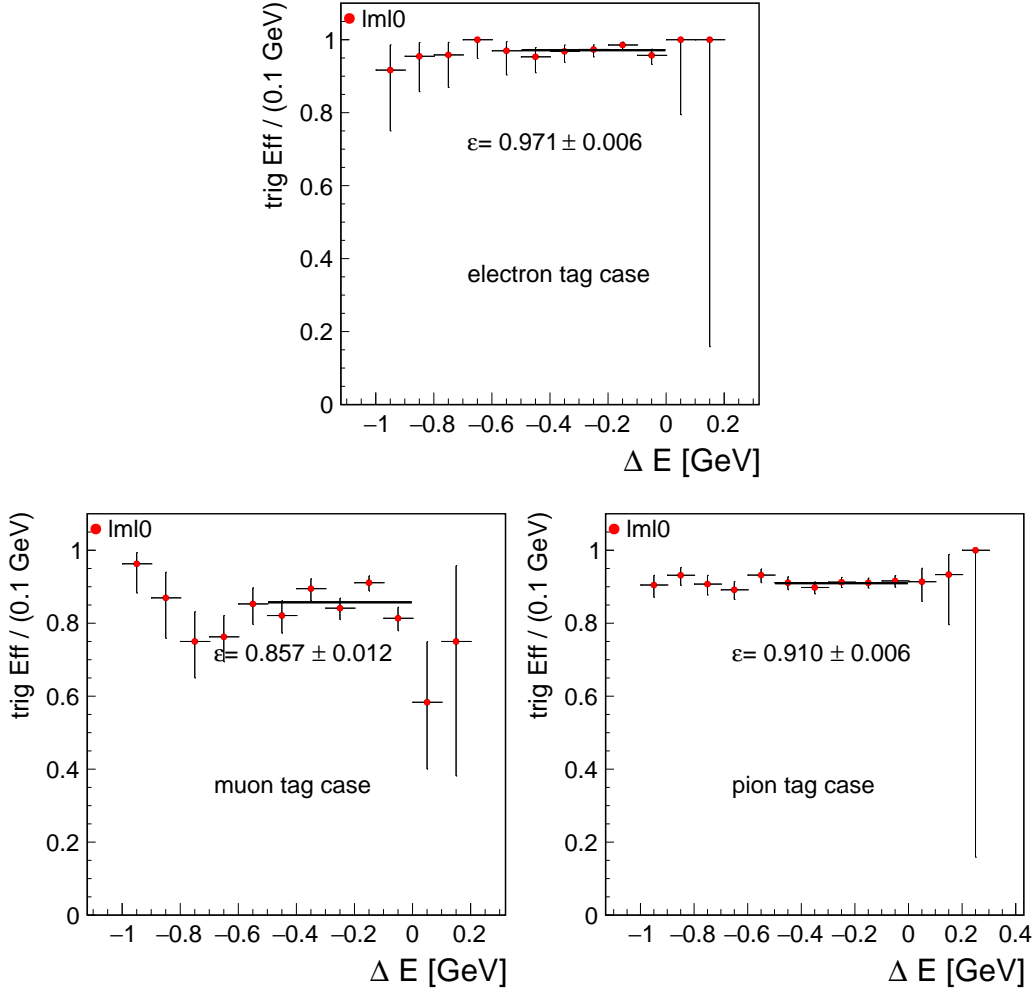


Figure 5.3: Trigger efficiency of `lml0` as a function of  $\Delta E$ . On top the electron, on bottom left the muon and on bottom right the pion tag cases are displayed.

These triggers were combined in data with the logical OR of the `lml0` and `fff` bits and in MC as follows:

$$\epsilon_{\text{trigger}}^{\text{MC}} = 1 - (1 - \epsilon_{\text{lml0}}) \cdot (1 - \epsilon_{\text{fff}}) \quad (5.4)$$

The combined efficiency is evaluated to be 99.68%, 98.21% and 99.17% for the electron, muon and pion tag cases respectively.

The correlation between the triggers is considered negligible because of the orthogonal detector information used by `fff` and `lml0`. Moreover, the total efficiencies are close to 100% and thus the systematic uncertainties are automatically limited.

Unfortunately, for the  $\tau^\pm \rightarrow \mu^\pm \mu^\mp \mu^\pm$  analysis it is not possible to use the lml0 efficiency results since pions behave differently with respect to muons in terms of energy deposition in the calorimeter. Figure 5.4 shows the ECL cluster energy deposition of muons (on the left) and pions (on the right), obtained from the track in the tag-side (selected using particle ID). In order to have a reliable lml0 efficiency for the three muon case, data from the  $\tau \rightarrow 3\pi\nu$  control sample were treated: the ECL energy depositions of pions were replaced with those of muons, randomly extracted cluster by cluster according to the distribution in Fig.5.4 (left).

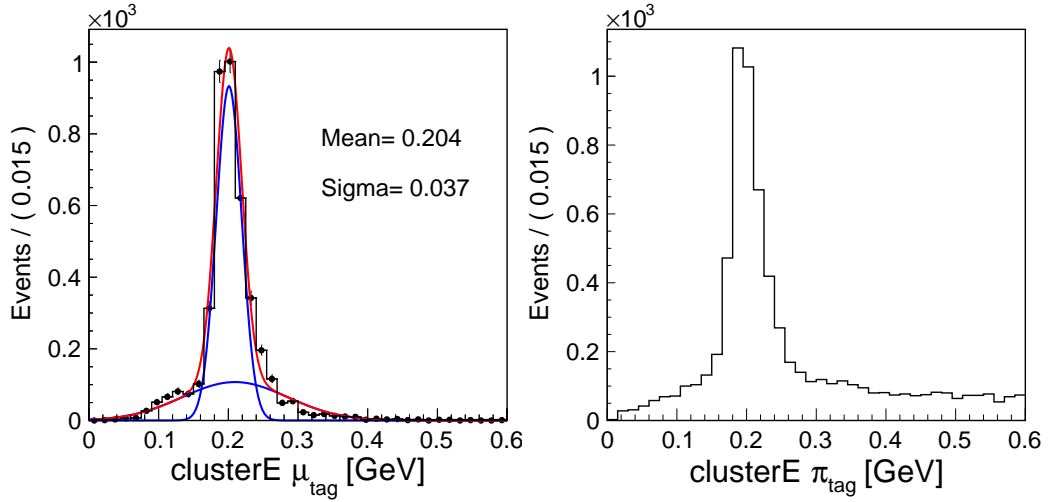


Figure 5.4: Cluster energy deposition of muons (left) and pions (right) obtained from MC. The fit on the muon distribution is made with the sum of 2 gaussian functions and the total  $\sigma$  is weighted with the integrals of each gaussian.

In this case, rather than requiring the trigger bit fired, in data trigger conditions were evaluated event by event based on the new cluster energy values, reproducing the lml0 requirements. The results show that the lml0 efficiency is substantially lower in the muon and pion tag cases with respect to the electron one.

The efficiency of each trigger is obtained by fitting fff and lml0 corresponding distributions at the end of the  $\Delta E$  spectrum, from -0.5 GeV to 0 GeV, and the fit error is assumed as the systematic uncertainty.

The fit results are reported in Fig.5.2 and Fig. 5.5, while the final numbers are summarised in Tab.5.1.

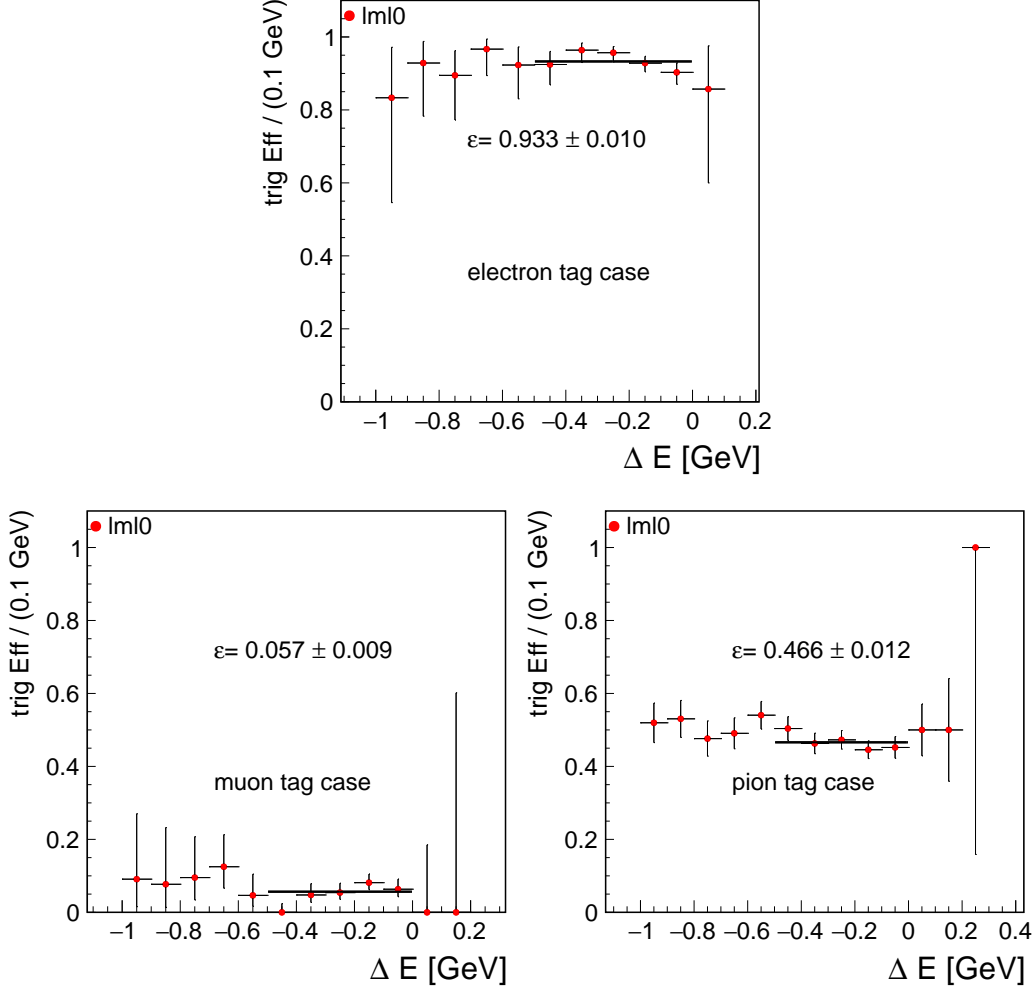


Figure 5.5: Trigger efficiency of *lml0* as a function of  $\Delta E$ , when the cluster energy of the 3 pions are the same as for muons. On top the electron case, on bottom left the muon case and on bottom right the pion case are displayed.

Trigger type	$\epsilon$ electron tag (%)	$\epsilon$ muon tag (%)	$\epsilon$ pion tag (%)
fff	$88.5 \pm 1.1$	$87.5 \pm 1.2$	$90.8 \pm 0.6$
<i>lml0</i>	$90.4 \pm 1.1$	$6.2 \pm 0.8$	$46.7 \pm 1.1$

Table 5.1: Summary of the trigger efficiency  $\epsilon$  results followed by the uncertainties which indicate the systematics.

The additional trigger lines considered for the  $\tau^\pm \rightarrow \mu^\pm \mu^\mp \mu^\pm$  channel rely on the system CDC-KLM. The minimal required selection is to have at least one triggered muon in the event: the logical OR of cdcklm1-4 is thus used (see Sec. 5.2). The efficiency of cdcklm1 was studied by the *BelleII* collaboration using a sample of  $l\mu$  events mostly coming from  $\tau\tau$  in  $1\times 1$  topology. They estimated a single muon efficiency of 87.77% in a wide BKLM angular and momentum acceptance, used to extrapolate the overall CDC-KLM trigger performances for the  $\tau^\pm \rightarrow \mu^\pm \mu^\mp \mu^\pm$  channel. The probability of having at least one muon firing the cdcklm trigger is:

$$\varepsilon_{\text{CDC-KLM}}^{\text{sig}} = 1 - (1 - \varepsilon_{\text{cdcklm1}})^{n_{\text{cdcklm}}} \quad (5.5)$$

where  $\varepsilon_{\text{cdcklm1}}$  is the single muon efficiency and  $n_{\text{cdcklm}}$  is the number of tracks per event identified as muons in the CDC-KLM momentum and angle acceptance. The final signal efficiency is evaluated as the mean value of the event trigger probability: 73% for the electron, 79% for the muon and 75% for the pion tag case. In Fig.5.6, the distribution of the efficiency (left), together with the corresponding mean values, and  $n_{\text{cdcklm}}$  (right) are shown for the 3 tag cases.

The systematics assigned on this efficiency is propagated from Eq.5.5, where a 5.9% systematics of the single muon cdcklm trigger is assumed. The average value is reported in Fig.5.7 and results are divided for different tag cases: 3.48% for electron 2.51% for muon and 3.42% for pion tag case.

The final trigger selection is the logical OR of lml0, fff and cdcklm. This is evaluated in MC as the probability that none of those triggers fire, subtracted to 1, averaged over all signal events:

$$\varepsilon_{\text{trigger}} = 1 - [(1 - \varepsilon_{\text{cdcklm1}})^{n_{\text{cdcklm}}} \cdot (1 - \varepsilon_{\text{lml0}}) \cdot (1 - \varepsilon_{\text{fff}})] \quad (5.6)$$

The corresponding distributions are displayed in Fig.5.8.

The event trigger systematics is propagated from Eq. 5.6 and the corresponding distributions are reported in Fig.5.9. The final systematics uncertainty are the mean values of these distributions, which are extracted for the electron, muon and pion tag case and they count respectively: 3.81%, 2.89% and 3.64%.

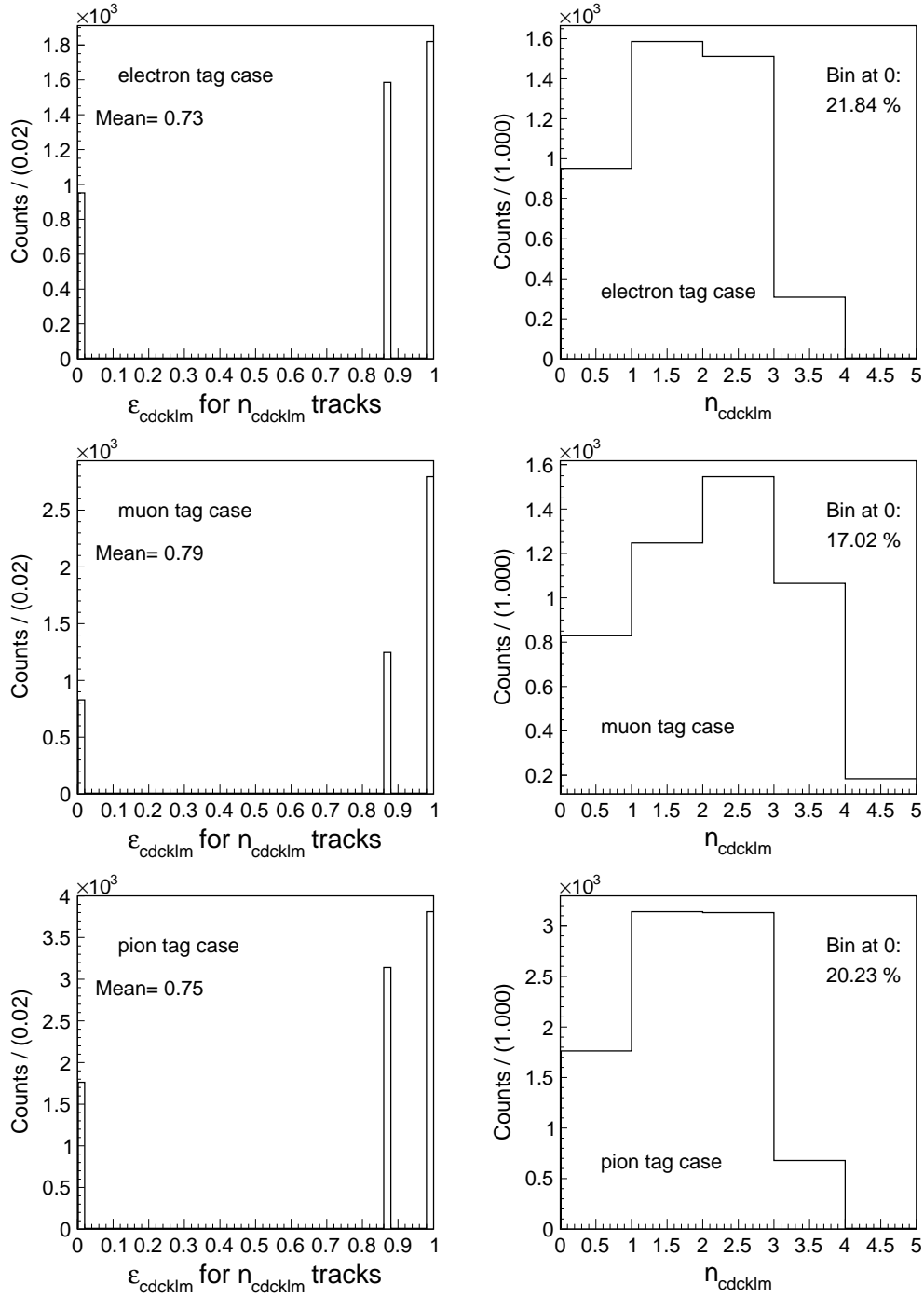


Figure 5.6: Trigger efficiency of cdcklm (left column) and  $n_{\text{cdcklm}}$  (right column) for the  $\tau^\pm \rightarrow \mu^\pm \mu^\mp \mu^\pm$  case. Electron (top), muon (middle) and pion (bottom) tag cases are displayed.

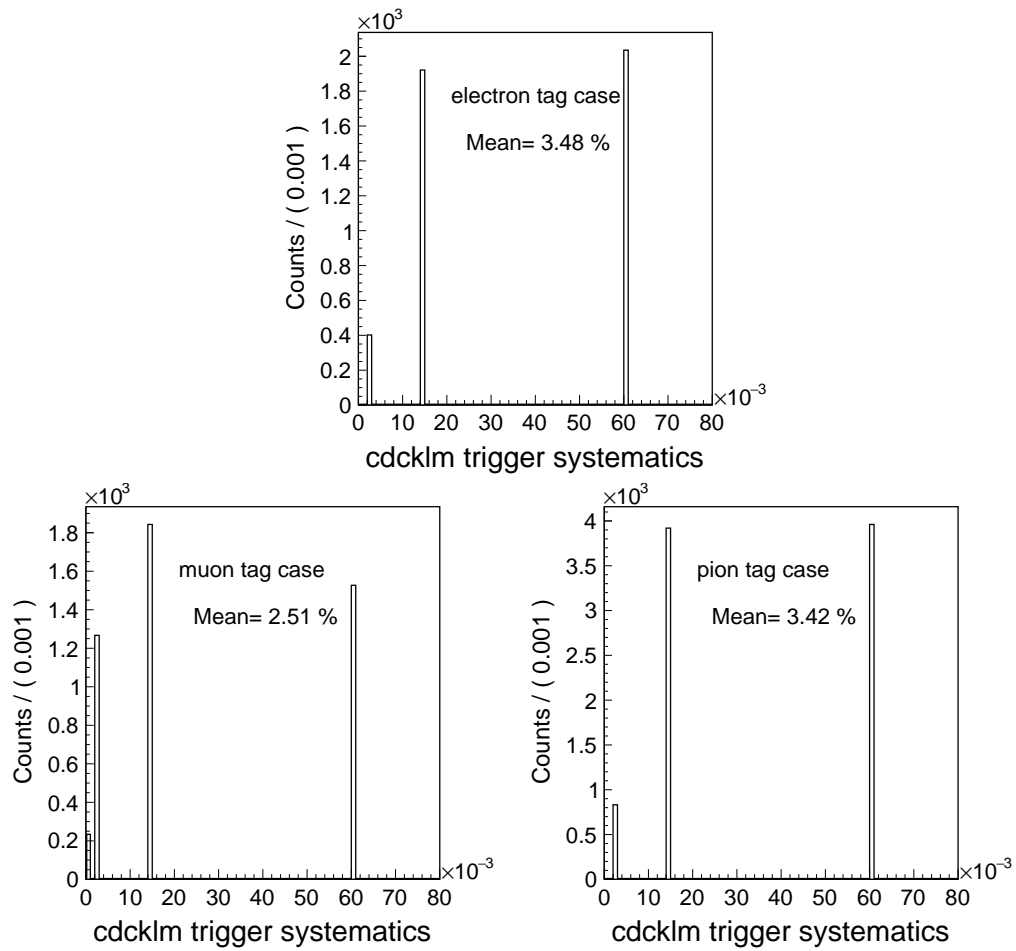


Figure 5.7: Trigger efficiency systematics of cdcklm event per event for the electron, muon and pion tag track cases. The mean value corresponds to the systematics uncertainty.

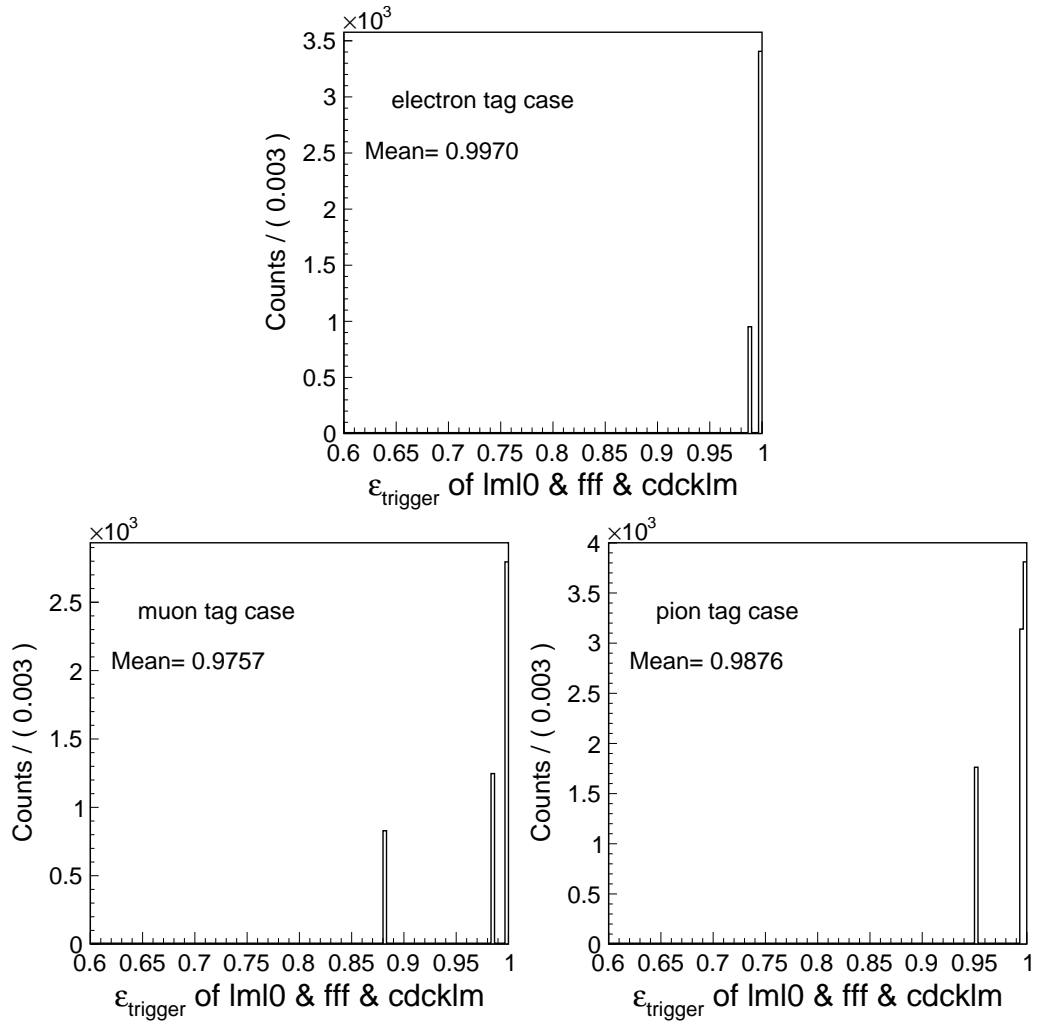


Figure 5.8: Final trigger efficiency selection for the  $\tau^\pm \rightarrow \mu^\pm \mu^\mp \mu^\pm$  analysis. Electron (top), muon (left) and pion (right) tag cases are displayed.

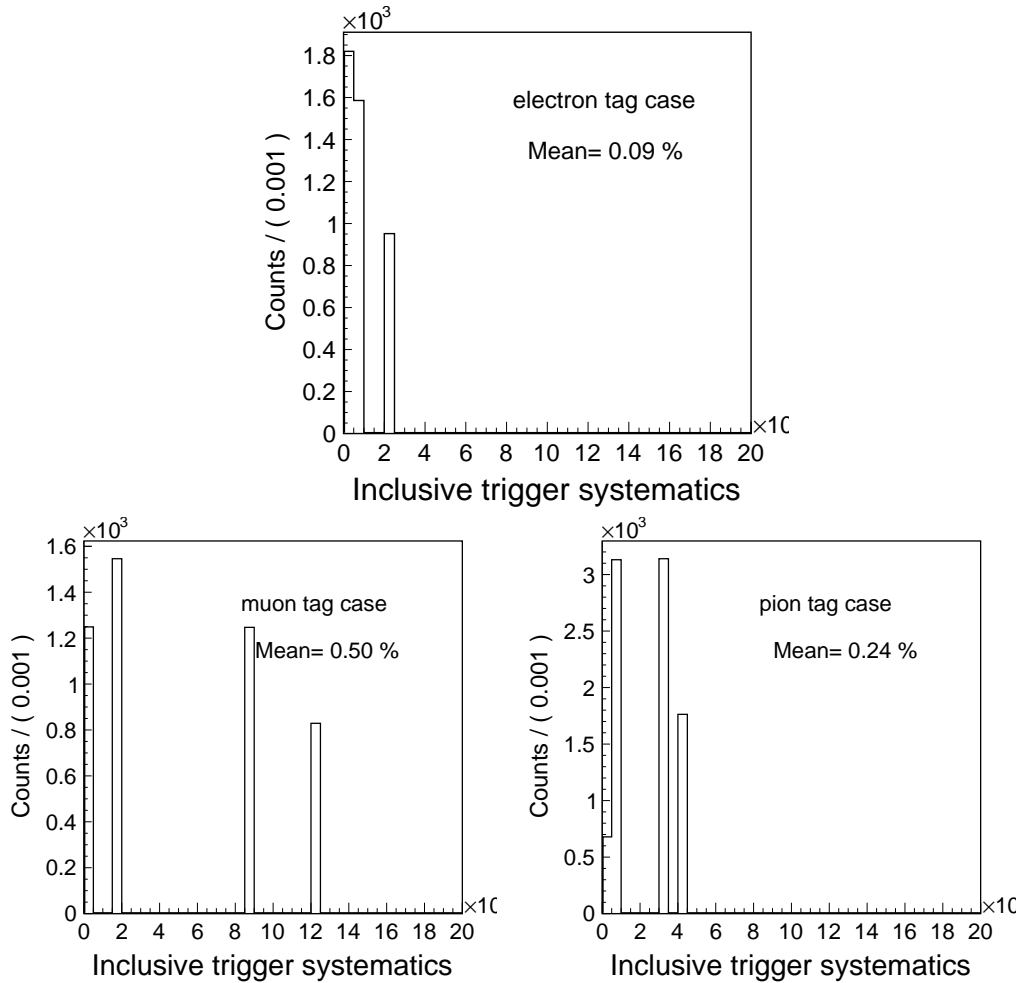


Figure 5.9: Trigger efficiency systematics event by event for the electron (top), muon (middle left) and pion (middle right) tag track cases. The mean value corresponds to the systematics uncertainty.

### 5.3.5 MuonID

In order to compute the systematics for the muonID, the uncertainties (statistics and systematics summed in quadrature), provided in terms of momentum and polar angle bins by the leptonID group, are used. When corrections are not available for some bins, a constant systematics equal to the average value among the available bins is considered. For each of the signal side muons gaussian random numbers with sigma equal to the systematics were generated. The distribution of the product of the three numbers (one per muon) was fitted with a double gaussian function. The average weighted sigma (using the integrals of each gaussian as weight) is

assumed to be the systematic uncertainty associated to the muonID. The result is shown in Fig.5.10, where a total systematic uncertainty of 2.6% is extracted.

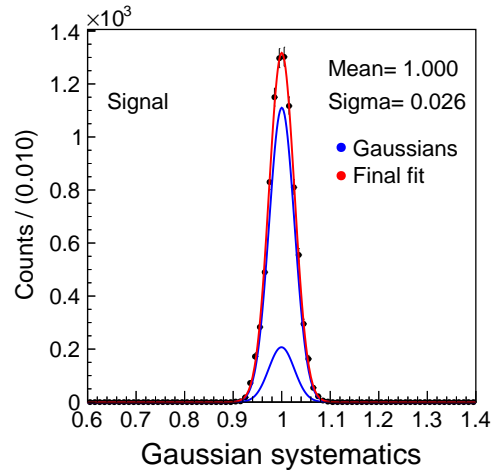


Figure 5.10: Systematics gaussian including muonID efficiency systematics for each muon in the signal side. A double gaussian fit with the results are superimposed.

A summary of the signal-related systematic sources and the final combination is reported in Tab.5.2. The overall systematics used on the final result is assumed to be the highest within the three different cases: 3.2%.

Table 5.2: Summary table of the signal systematic uncertainties. Electron, muon and pion tag cases are considered for the trigger systematics (el, mu and pi, respectively). The total uncertainty is reported at the bottom.

Source	Systematics (%)
Beam energy shift	0.033
Tracking efficiency	1.8
Momentum resolution	0.014
Trigger efficiency	0.09(el), 0.50(mu), 0.24(pi)
muonID	2.6
Total	3.16(el), 3.20(mu), 3.17(pi)

## 5.4 Background systematics

In order to study the background systematics, the control sample described in Sec. 5.1 was used, with a trigger selection applied. The required trigger is

the logical OR of `lml0` and `fff`, whose correction factors were estimated from results in Sec.5.3.4. Several distributions were checked for potential data-MC discrepancies. This is a crucial study, since the background is reduced by several orders of magnitude by the analysis selection, keeping only a very tiny fraction of the initial phase space: small data-MC discrepancies can easily reflect in large final disagreements. Results are shown in figures 5.11, 5.12, 5.13, where the  $\tau^\pm \rightarrow \mu^\pm \mu^\mp \mu^\pm$  signal contribution is superimposed with an arbitrary normalisation, for shape comparison. At the bottom of the plots, data-MC ratios, with a `pol0` fit superimposed, are shown.

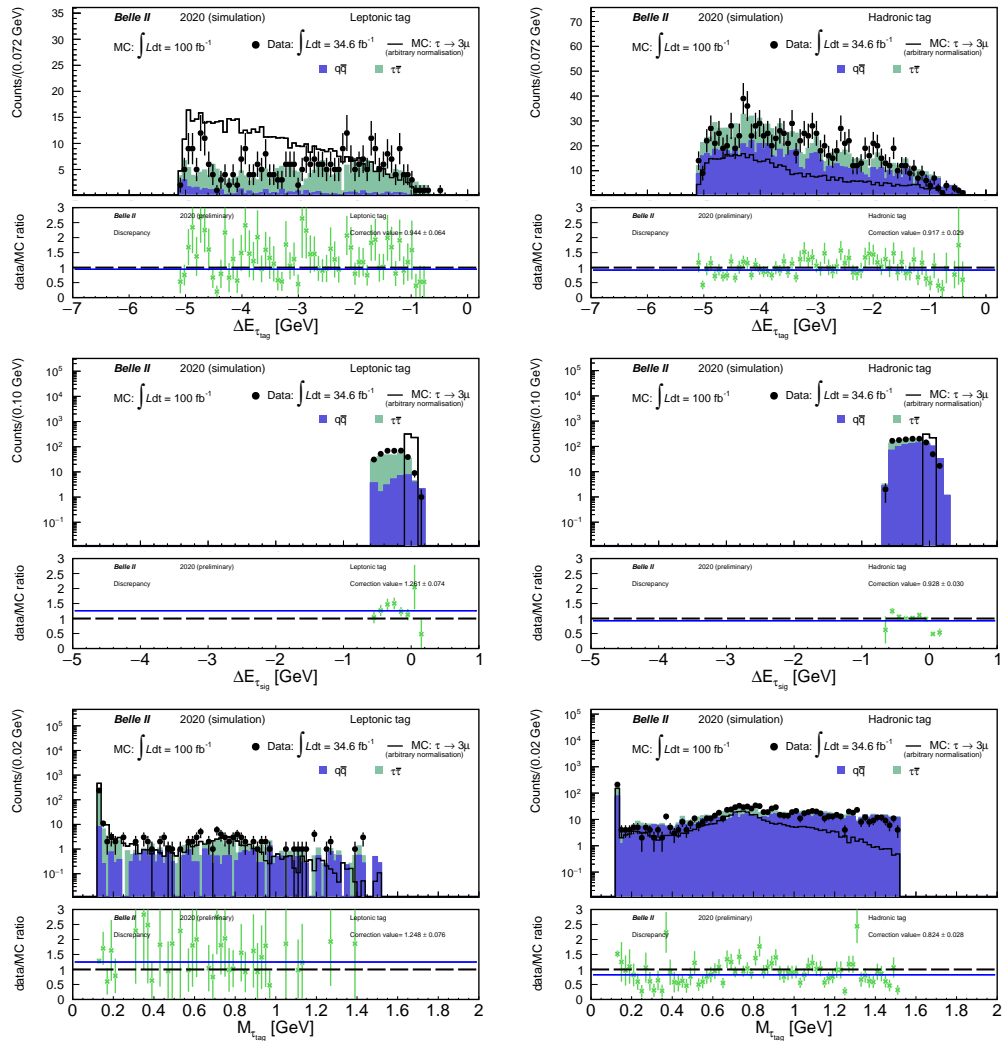


Figure 5.11: On the left (right) starting from the top there are the distributions of  $\Delta E_{\tau_{tag}}$ ,  $\Delta E_{\tau_{sig}}$  and  $M_{\tau_{tag}}$  for the leptonic (hadronic) tag case.

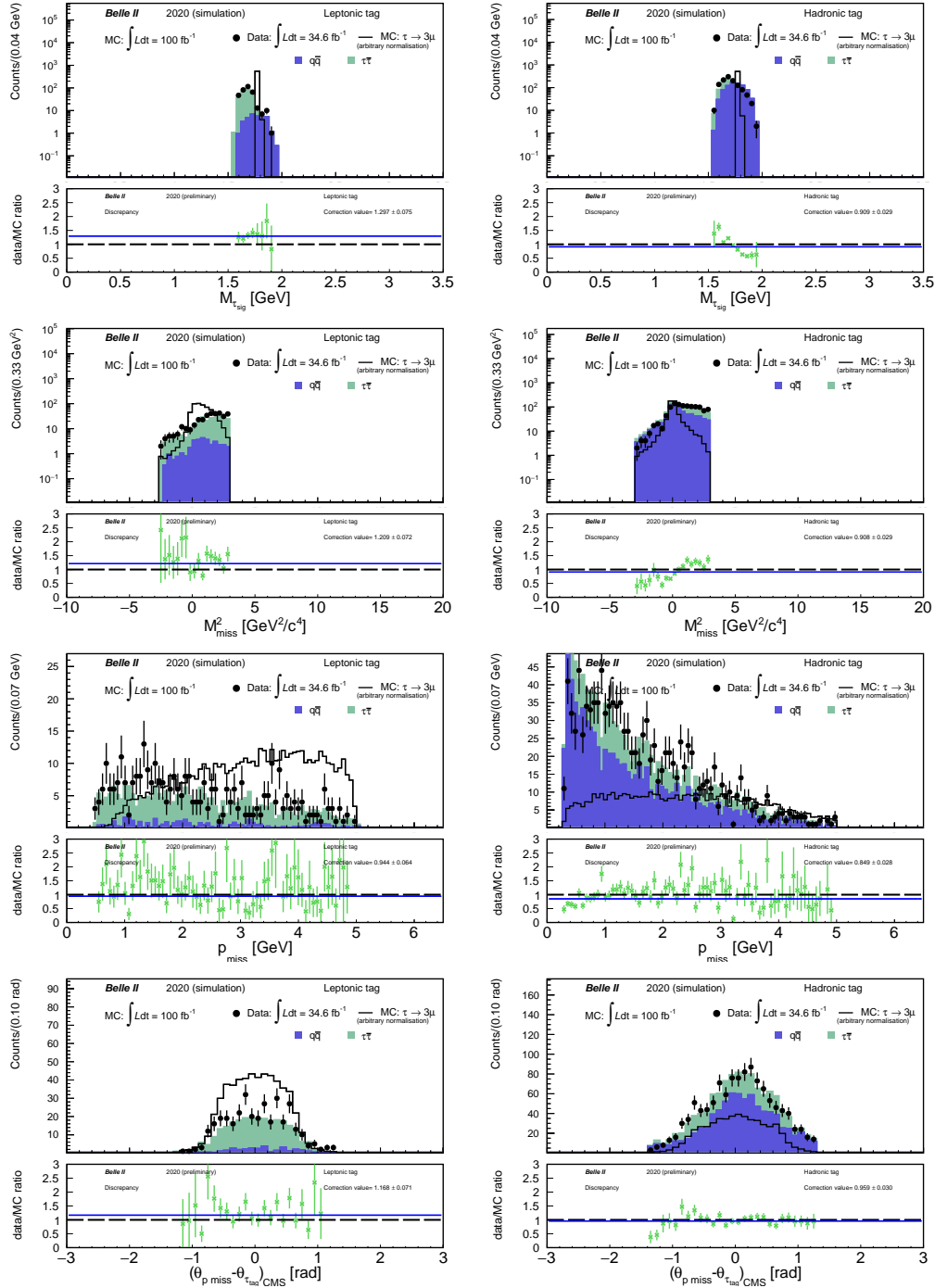


Figure 5.12: On the left (right) starting from the top there are the distributions of  $M_{\tau_{sig}}$ ,  $M_{miss}^2$ ,  $p_{miss}$  and  $(\theta_{p_{miss}} - \theta_{\tau_{tag}})_{CMS}$  for the leptonic (hadronic) tag case.

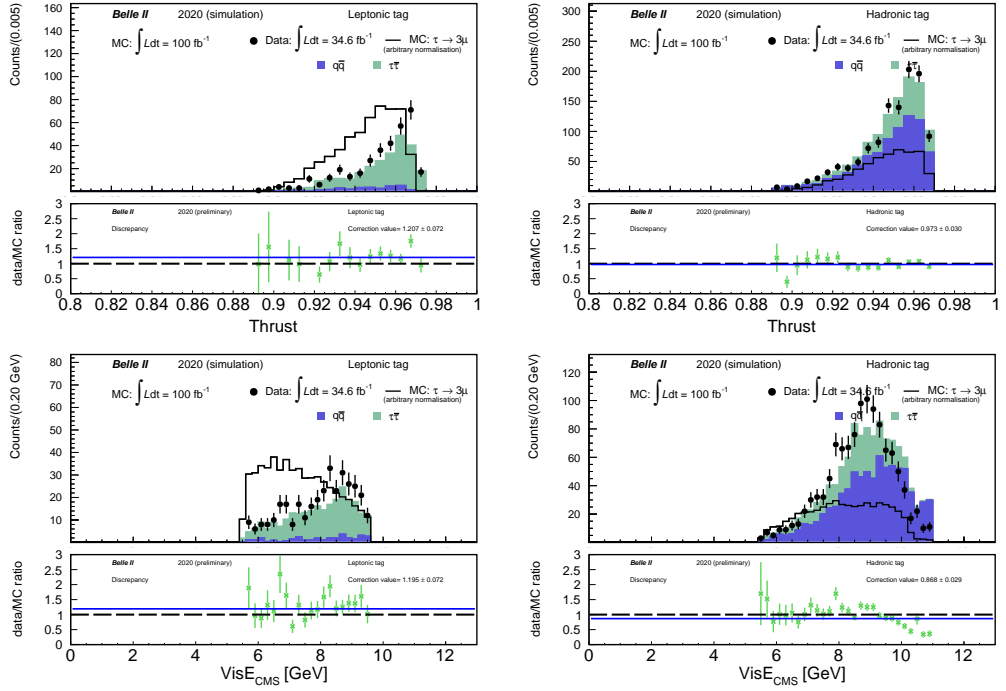


Figure 5.13: On the left (right) starting from the top there are the distributions of Thrust and VisibleEnergy<sub>CMS</sub> for the leptonic (hadronic) tag case.

For each variable, an overall integral discrepancy is computed as the average of the bin by bin data-MC ratio with weights  $1/\sigma^2$ , where  $\sigma$  is the error in the bin (see Fig.5.14 top). For several distributions the signal and background shapes are very different. In the final measurement, after all the selections, the background will unavoidably have shapes very close to those of the signal. In order to produce a background evaluation as realistic as possible, a new overall integral discrepancy is defined by further weighting the data-MC ratios for each variable according to the signal shapes. For this purpose  $W_{bin}$  was defined for all the bins as in Eq.5.7.

$$W_{bin} = N_{bin}^{sig}/N_{tot}^{sig} \quad (5.7)$$

Here,  $N_{bin}^{sig}$  is the number of signal entries per bin, while  $N_{tot}^{sig}$  is the total number of entries of the MC signal sample.

The final results are shown in Fig 5.14 (bottom), with a pol0 fit superimposed.

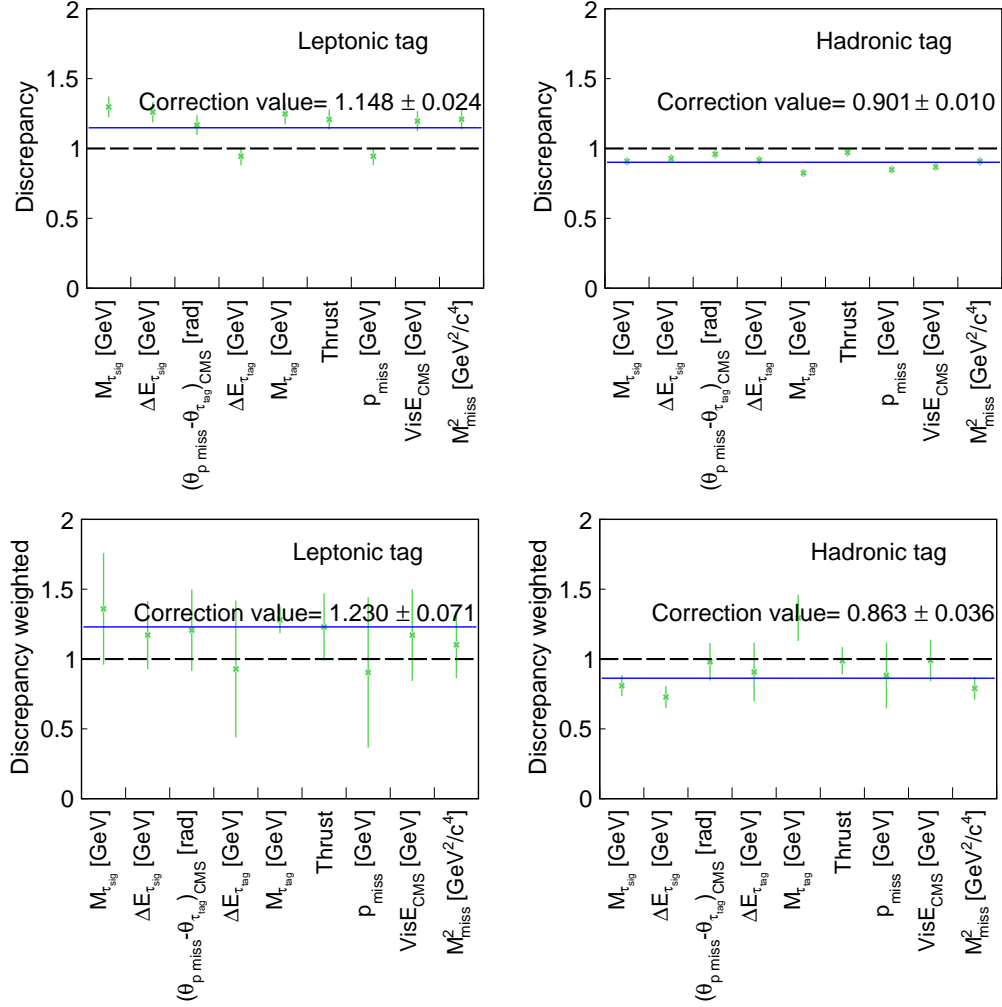


Figure 5.14: Data-MC discrepancies extracted from several variables not weighted (top) and weighted (bottom) to the signal shape. A pol0 fit with the corresponding error is superimposed.

These results can be implemented in the analysis in two different ways:

1. Correct the MC background by the mean value of the fit (1.230 for the leptonic and 0.863 for the hadronic tag case) and use the error of the fit (7.1% for the leptonic and 3.6% for the hadronic tag case) as the corresponding systematic uncertainty;
2. Not apply any correction on the background and assign the discrepancy itself as the corresponding systematic uncertainty: 23.0% for the leptonic and 13.7% for the hadronic tag case.

Since the final background after the analysis selections is predicted to be very small (close to 0), the limit estimate on the branching fraction is expected not to be heavily affected by the related systematics, being dominated by statistical fluctuations. The final choice was number 2.

### 5.4.1 MuonID

The muonID contribution to the systematics is estimated with the same strategy as in Sec.5.3.5 with the only difference that the true and the fake muons were distinguished using the MC truth information. If the track is a true muon the systematics related to the muonID efficiency were implemented, otherwise the systematics related to the  $\pi \rightarrow \mu$  mis-ID rate were used.

The gaussian distribution including the systematics of all 3 signal side tracks is reported in Fig.5.15. When there are no available corrections for the momentum-theta bins, a systematics of 10% is considered since it is the average systematics among all the available bins. The final result shows an effect of 14.2%.

The overall systematics on the background is derived as a sum in quadrature of the inclusive estimation contribution and the muonID one: 27.03% for the leptonic tag case and 19.73% for the hadronic tag case. Since the only backgrounds surviving the analysis selection are appearing in the hadronic tag case, the corresponding uncertainty is the only one considered in the limit estimation (see Sec. 6.2).

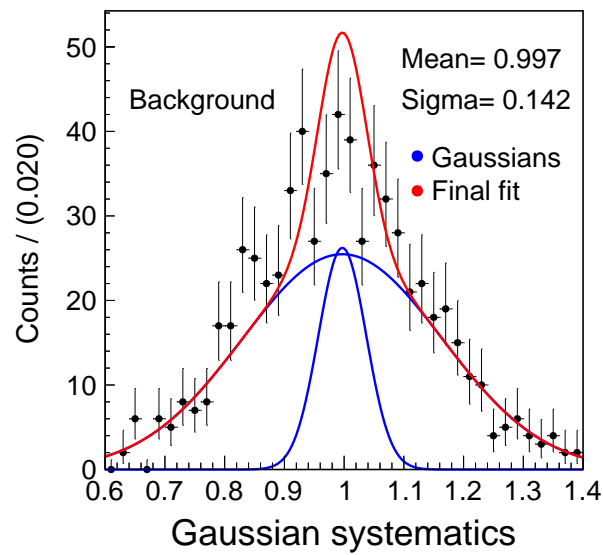


Figure 5.15: Systematics gaussian including muonID efficiency and misID systematics for each track in the signal side. The double gaussian fit result is superimposed.



# Chapter 6

## Results

In this chapter the optimised procedure and the systematics studies described in Chapters 4, 5 were used to extract the final results, which consist in the signal efficiency value and the number of background event surviving the final selection. After an additional check on data in the side-bands, the un-blinding of the final data-set inside the signal region was performed. The number of observed events together with the efficiency and the survived background events, were used as inputs for the limit estimation, described in the last part.

### 6.1 Analysis results

Since four different samples of  $2 \text{ ab}^{-1}$  integrated luminosity were considered during the optimisation process, in order to check the stability of the proposed approach, the same strategy was undertaken here. Therefore the optimised cuts (see Tab. 4.3.3, together with the additional hand made cuts (see Tab. 4.4), were applied on a sample of  $3 \text{ ab}^{-1}$  to obtain the final efficiency and the background retention of the  $\tau^\pm \rightarrow \mu^\pm \mu^\mp \mu^\pm$  search.

For the cut application procedure, the following corrections to MC samples (see Chap.5) were implemented: corrections related to trigger efficiencies for both signal and backgrounds (they differ between the two samples), tracking efficiency and PID corrections. The results of efficiency and background retention are shown in Tab.6.1. The number of background events were scaled to  $500 \text{ fb}^{-1}$ , to have a direct comparison with the BaBar results. BaBar (Belle) efficiency was found to be 6.6% (7.3%) along with 0.44 (0.13) surviving background events. The proposed approach has  $\sim 2$  times more efficiency than BaBar/Belle and comparable background contributions.

Table 6.1: Results of efficiency and number of background events passing the optimised and additional hand made cuts. Binomial statistical error is added for the signal while a Poisson one is considered for the background as a reference, since it does not enter the limit computation. Results are given for the leptonic and hadronic tag cases.

$1^{st} sample$	Bkg events	$\varepsilon_{sig}$ [%]	$2^{nd} sample$	Bkg events	$\varepsilon_{sig}$ [%]
Lep	0	6.21	Lep	0	6.19
Had	0.23	5.81	Had	0.31	6.06
Total	$0.23 \pm 0.20$	$12.02 \pm 0.10$	Total	$0.31 \pm 0.23$	$12.25 \pm 0.10$

$3^{rd} sample$	Bkg events	$\varepsilon_{sig}$ [%]	$4^{th} sample$	Bkg events	$\varepsilon_{sig}$ [%]
Lep	0.19	6.87	Lep	0	5.29
Had	0.32	6.06	Had	0.31	6.44
Total	$0.52 \pm 0.29$	$12.94 \pm 0.10$	Total	$0.31 \pm 0.23$	$11.73 \pm 0.099$

### 6.1.1 Data-MC side-band checks

Before proceeding with the data un-blinding, a side-band study was performed, as a further check. This is crucial since here the full muonID procedure is used, differently from the systematic studies in Chap 5, where the pionID was applied to the  $\tau \rightarrow 3\pi\nu$  control sample. The side-band is chosen to be between  $10\sigma$  and  $20\sigma$  away from the center of the signal region described in Sec. 4.2.2, where the  $\sigma$ s are taken from the  $\Delta E'_{3\mu}$  and  $M'_{3\mu}$  fits performed there. The number of events surviving the final analysis selection in the  $\Delta E'_{3\mu}$ - $M'_{3\mu}$  plane was checked for both data and MC. The MC sample of  $5 \text{ ab}^{-1}$ , weighted down to the data statistics of  $52.2 \text{ fb}^{-1}$ , counts 1.53 events while in data none of the events survived. Comparing the same numbers without the application of the hand made cuts (see Tab. 4.4), the MC counts 5.33 events while in data 6 events survived. This is a nice agreement, considering the very low number of events involved. A summary of the results is reported in Tab. 6.2.

Table 6.2: Comparison between data and MC yields outside the signal region, between  $10\sigma$  and  $20\sigma$ . The statistical errors for the MC selection are showed.

<i>Side-band comparison</i>	MC events	Data events
Before hand made cuts	$5.33 \pm 0.24$	6
After all cuts	$1.53 \pm 0.13$	0

### 6.1.2 Data un-blinding

The final un-blinding is performed on  $52.2 \text{ fb}^{-1}$  and resulted in 0 observed events inside the signal region. This is in agreement with the MC expectations and, considering the data statistics available at *BelleII*, with previous results obtained by the Belle and BaBar experiments. In fact 0 events were observed for both the experiments that relied on  $782 \text{ fb}^{-1}$  and  $486 \text{ fb}^{-1}$  respectively.

## 6.2 Limit estimation

The main goal of a typical data analysis is to compare model predictions with results from data, to draw conclusions on the validity of the considered model and to extract the allowed values of parameters within a specific theoretical framework. In this analysis a model independent limit on the BF is estimated. *BelleII* expected results are reported in Fig. 6.1, where a comparison with several other experiments is made for most of the LFV channels in the  $\tau$  sector.

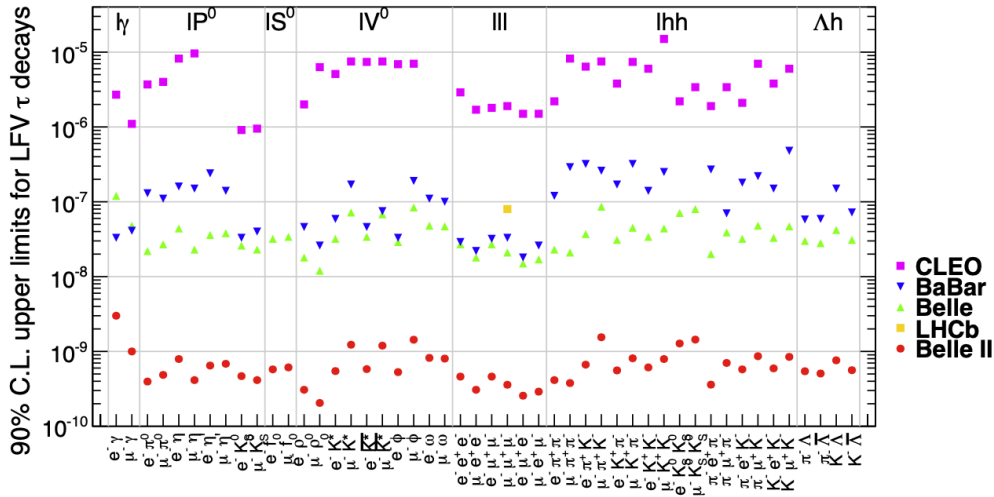


Figure 6.1: Summary of the 90% CL upper limits for the BF of  $\tau$  LFV decays obtained in the CLEO (purple boxes), BaBar (blue inverted triangles), Belle experiments (green triangles) and LHCb (yellow boxes). The red circles indicate the *BelleII* expectations, extrapolated from Belle results to an integrated luminosity of  $50 \text{ ab}^{-1}$ .

### 6.2.1 Upper limit settings implementation

The estimate of a 90% CL upper limit on the  $\tau^\pm \rightarrow \mu^\pm \mu^\mp \mu^\pm$  BF is done following the equation:

$$UL_{90\%}(BF : \tau^\pm \rightarrow \mu^\pm \mu^\mp \mu^\pm) = \frac{N_{UL}^{90\%}}{2 \cdot \varepsilon_{sig} \cdot \mathcal{L}_{int}^{data} \cdot \sigma_{\tau\tau}} \quad (6.1)$$

where  $\varepsilon_{sig}$  is the signal efficiency,  $\mathcal{L}_{int}^{data}$  is the data integrated luminosity,  $\sigma_{\tau\tau}$  is the tau-pair production cross section and  $N_{UL}^{90\%}$  is the 90% CL upper limit on the number of signal events.

The BF limit is estimated assuming the likelihood of the observed number of events to be Poissonian. The same assumption holds for the expected number of MC events for each background source and the signal. The final likelihood is the sum of those contributions. The background sources considered in the limit are:  $q\bar{q}$ ,  $\tau\tau$  and  $4\mu$ .

A flat prior is assumed for the BF between 0 and  $10^{-7}$ . Additional parameters were considered during the calculation, as described below:

- Data luminosity: a gaussian prior was used for both parameters between  $\pm 3\sigma$ : 5% for the MC and 0.054% for the data. The latter was estimated by the *BelleII* collaboration;
- Efficiency of each background source: flat priors for the backgrounds were used between 0 and  $10^{-9}$ . This interval is chosen accordingly to the expected number of events surviving the final selection;
- Signal efficiency: a gaussian prior was used between  $\pm 5\sigma$ , where the  $\sigma$  is the statistical uncertainty only;
- Cross section of the background sources: gaussian priors were used between  $\pm 5\sigma$ , where  $\sigma$  is assumed to be 5%. The value for the  $4\mu$  sample is 0.34 pb [58] while the remaining ones are summarised in Tab. 2.1;
- Systematics: gaussian priors were used between  $\pm 5\sigma$ , where  $\sigma$  are the uncertainties estimated in Chap. 5.

### 6.2.2 The Bayesian Analysis Toolkit

The limit estimate was computed numerically using the Bayesian Analysis Toolkit (BAT) [59]. BAT is developed to evaluate the posterior probability distribution for models and their parameters. The machinery is based on the

Bayes' Theorem and exploits Markov Chain Monte Carlo [60], giving access to the posterior probability results. This enables straightforward parameter estimation, limit setting and uncertainty propagation.

The BAT framework is implemented in C++ and it is interfaced to software packages like ROOT [50], Minuit [61] and RooStats [62]. A set of predefined models are already implemented, allowing to cover several common statistical problems. Furthermore, it can be manipulated to define more complicated models with ease.

### 6.3 Limit results

The results are extracted from a marginalization process done using the Metropolis algorithm (see [63] for more details). The precision used by the calculator was set to High which is the maximum within the possible choices. The result was calculated 10 times and averaged in order to have a better idea on the final outcome.

The BF limit is  $8.30 \pm_{0.04}^{0.02} \cdot 10^{-8}$  where the errors indicate the maximum discrepancy between the mean and the highest and lowest value obtained by running the calculator. The corresponding distribution is reported in Fig. 6.2. Here, the y axis reports the so-called marginalized distribution<sup>1</sup>.

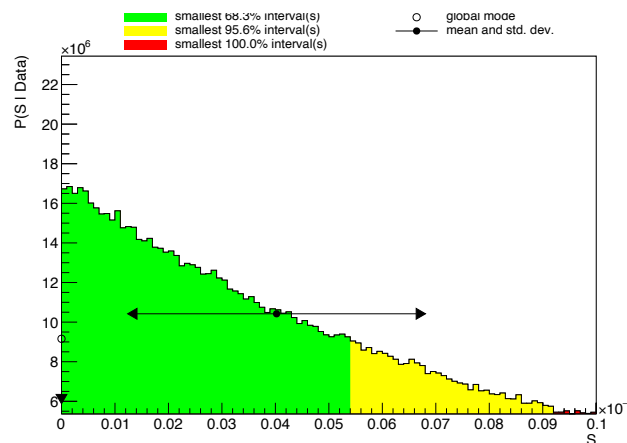


Figure 6.2: Distribution of the limit value ( $S$ ) provided by BAT. The 90% of the statistics is below  $8.30 \cdot 10^{-8}$ .

<sup>1</sup>It represents the posterior Probability Density Function (PDF) of a single parameter of a model given the data when all other parameters are integrated over [64]

An additional check was made in order to compare the result of the analysis presented in this thesis with the current best results obtained by the Belle and BaBar experiments. The check is performed considering the number of expected background events scaled with the considered luminosity. Moreover, 0 observed events are assumed and the same signal efficiency and systematics uncertainties are used. In Tab. 6.3 a summary of the final values is shown, indicating an improvement of a factor  $\sim 2$  at *BelleII* with respect to Belle and BaBar.

	<i>BelleII</i> w/ 782 fb <sup>-1</sup>	Belle	<i>BelleII</i> w/ 486 fb <sup>-1</sup>	BaBar
Upper limit	1.28	2.1	2.1	3.3

Table 6.3: Summary upper limit results for the  $\tau^\pm \rightarrow \mu^\pm \mu^\mp \mu^\pm$  BF. Values are reported in terms of  $10^{-8}$ .

As soon as the *BelleII* experiment will collect a sufficient amount of data, the analysis will undergo towards publication. During 2021, the integrated luminosity is expected to exceed that of BaBar and Belle (see Fig. 2.4).

# Conclusions and future prospects

In this thesis work the search of the LFV decay  $\tau^\pm \rightarrow \mu^\pm \mu^\mp \mu^\pm$ , one of the golden channels in the  $\tau$  sector, at *BelleII* was presented. Previous searches did not observe any signal and upper limit estimations of the BF were already provided: the best limits are holding by the Belle and BaBar experiments. An optimised approach was presented and results were provided on a data-sample of  $\sim 52 \text{ fb}^{-1}$ , collected during 2019 and part of 2020. No data excess was observed and a 90% CL upper limit on the BF was estimated to be  $8.30 \cdot 10^{-8}$ . A comparison with the best previous results was done to test the goodness of the analysis strategy. Extrapolating to the same integrated luminosity of the Belle Experiment, a limit of  $1.28 \cdot 10^{-8}$  is expected: an improvement of a factor  $\sim 1.5$  is thus foreseen.

Since this analysis is statistically limited, the inclusion of future data, hopefully in sizeable amount, will lead to a journal publication. As shown in Fig. 2.4, the same statistics as of BaBar is expected to be collected within the summer of 2021. Since the performances of the *BelleII* detector can be improved by that time, the analysis results would further benefit too. More in detail, the estimation of systematic uncertainties will benefit from the usage of a larger data sample and a deeper knowledge of the detector responses. In addition, the MC samples will rely on data-driven backgrounds allowing the data-MC agreement to improve and providing more reliable results. Further improvements are expected also on muonID performances, mostly on the muon mis-ID rate from hadrons: preliminary studies are already being performed within the *BelleII* collaboration. The main upgrade of the analysis concerns the usage of a larger data sample. The current search is performed with a MC sample of  $5 \text{ ab}^{-1}$ , showing that the background contribution will still be compatible with 0 up to a data sample equivalent to  $1 \text{ ab}^{-1}$ . For this reason, the analysis strategy described in this work can be revised in the future, once the background contamination exceeds the unit. The final sensitivity of this search is

subject to future upgrades of the detector, presently under discussion.

# Appendices



## Appendix: muonID data-MC correction table in the $e^+e^- \rightarrow \mu^+\mu^-\gamma$ channel

Table 4: Summary table of the data and MC efficiencies and the final correction values. Results are provided for  $\mu\text{ID}>0.5$  and the uncertainties reported are statistical and systematical.

p bin [GeV]	$\theta$ bin [rad]	Data efficiency	MC efficiency	Correction
0.70-1.00	0.40-0.64	0.8295 <sup>+0.0052</sup> <sub>-0.0053</sub>	0.8935 <sup>+0.0024</sup> <sub>-0.0024</sub>	0.9284 <sup>+0.0147</sup> <sub>-0.0147</sub>
1.00-1.50	0.40-0.64	0.8469 <sup>+0.0036</sup> <sub>-0.0037</sub>	0.9240 <sup>+0.0015</sup> <sub>-0.0015</sub>	0.9165 <sup>+0.0195</sup> <sub>-0.0195</sub>
1.50-2.00	0.40-0.64	0.8745 <sup>+0.0032</sup> <sub>-0.0033</sub>	0.9391 <sup>+0.0013</sup> <sub>-0.0013</sub>	0.9312 <sup>+0.0246</sup> <sub>-0.0246</sub>
2.00-2.50	0.40-0.64	0.9049 <sup>+0.0027</sup> <sub>-0.0028</sub>	0.9510 <sup>+0.0011</sup> <sub>-0.0011</sub>	0.9515 <sup>+0.0253</sup> <sub>-0.0254</sub>
2.50-3.50	0.40-0.64	0.9199 <sup>+0.0016</sup> <sub>-0.0017</sub>	0.9570 <sup>+0.0007</sup> <sub>-0.0007</sub>	0.9613 <sup>+0.0231</sup> <sub>-0.0231</sub>
3.50-4.50	0.40-0.64	0.9222 <sup>+0.0014</sup> <sub>-0.0014</sub>	0.9637 <sup>+0.0005</sup> <sub>-0.0005</sub>	0.9569 <sup>+0.0140</sup> <sub>-0.0140</sub>
4.50-6.50	0.40-0.64	0.9429 <sup>+0.0005</sup> <sub>-0.0005</sub>	0.9720 <sup>+0.0002</sup> <sub>-0.0002</sub>	0.9701 <sup>+0.0030</sup> <sub>-0.0030</sub>
0.70-1.00	0.64-0.82	0.6896 <sup>+0.0067</sup> <sub>-0.0068</sub>	0.8135 <sup>+0.0032</sup> <sub>-0.0032</sub>	0.8477 <sup>+0.0129</sup> <sub>-0.0129</sub>
1.00-1.50	0.64-0.82	0.8472 <sup>+0.0038</sup> <sub>-0.0039</sub>	0.9302 <sup>+0.0015</sup> <sub>-0.0015</sub>	0.9109 <sup>+0.0214</sup> <sub>-0.0214</sub>
1.50-2.00	0.64-0.82	0.9021 <sup>+0.0030</sup> <sub>-0.0031</sub>	0.9585 <sup>+0.0011</sup> <sub>-0.0012</sub>	0.9411 <sup>+0.0271</sup> <sub>-0.0271</sub>
2.00-2.50	0.64-0.82	0.9026 <sup>+0.0029</sup> <sub>-0.0029</sub>	0.9566 <sup>+0.0011</sup> <sub>-0.0011</sub>	0.9436 <sup>+0.0311</sup> <sub>-0.0311</sub>
2.50-3.50	0.64-0.82	0.9092 <sup>+0.0018</sup> <sub>-0.0018</sub>	0.9637 <sup>+0.0007</sup> <sub>-0.0007</sub>	0.9435 <sup>+0.0235</sup> <sub>-0.0235</sub>
3.50-4.50	0.64-0.82	0.9063 <sup>+0.0015</sup> <sub>-0.0015</sub>	0.9653 <sup>+0.0005</sup> <sub>-0.0005</sub>	0.9389 <sup>+0.0134</sup> <sub>-0.0134</sub>
4.50-6.50	0.64-0.82	0.8933 <sup>+0.0007</sup> <sub>-0.0007</sub>	0.9741 <sup>+0.0002</sup> <sub>-0.0002</sub>	0.9171 <sup>+0.0021</sup> <sub>-0.0021</sub>
0.70-1.00	0.82-1.16	0.7958 <sup>+0.0040</sup> <sub>-0.0041</sub>	0.8815 <sup>+0.0019</sup> <sub>-0.0019</sub>	0.9027 <sup>+0.0104</sup> <sub>-0.0105</sub>
1.00-1.50	0.82-1.16	0.8918 <sup>+0.0023</sup> <sub>-0.0024</sub>	0.9543 <sup>+0.0009</sup> <sub>-0.0009</sub>	0.9344 <sup>+0.0170</sup> <sub>-0.0170</sub>
1.50-2.00	0.82-1.16	0.9380 <sup>+0.0017</sup> <sub>-0.0018</sub>	0.9610 <sup>+0.0008</sup> <sub>-0.0008</sub>	0.9760 <sup>+0.0210</sup> <sub>-0.0210</sub>
2.00-2.50	0.82-1.16	0.9372 <sup>+0.0016</sup> <sub>-0.0017</sub>	0.9602 <sup>+0.0008</sup> <sub>-0.0008</sub>	0.9761 <sup>+0.0182</sup> <sub>-0.0182</sub>
2.50-3.50	0.82-1.16	0.9429 <sup>+0.0010</sup> <sub>-0.0010</sub>	0.9637 <sup>+0.0005</sup> <sub>-0.0005</sub>	0.9784 <sup>+0.0137</sup> <sub>-0.0137</sub>
3.50-4.50	0.82-1.16	0.9416 <sup>+0.0008</sup> <sub>-0.0008</sub>	0.9634 <sup>+0.0004</sup> <sub>-0.0004</sub>	0.9774 <sup>+0.0059</sup> <sub>-0.0059</sub>
4.50-6.50	0.82-1.16	0.9440 <sup>+0.0004</sup> <sub>-0.0004</sub>	0.9662 <sup>+0.0002</sup> <sub>-0.0002</sub>	0.9770 <sup>+0.0013</sup> <sub>-0.0013</sub>
0.70-1.00	1.16-1.46	0.8653 <sup>+0.0036</sup> <sub>-0.0037</sub>	0.9378 <sup>+0.0015</sup> <sub>-0.0015</sub>	0.9227 <sup>+0.0094</sup> <sub>-0.0095</sub>
1.00-1.50	1.16-1.46	0.9196 <sup>+0.0021</sup> <sub>-0.0022</sub>	0.9609 <sup>+0.0009</sup> <sub>-0.0009</sub>	0.9570 <sup>+0.0138</sup> <sub>-0.0138</sub>
1.50-2.00	1.16-1.46	0.9472 <sup>+0.0017</sup> <sub>-0.0017</sub>	0.9634 <sup>+0.0008</sup> <sub>-0.0008</sub>	0.9832 <sup>+0.0174</sup> <sub>-0.0174</sub>
2.00-2.50	1.16-1.46	0.9483 <sup>+0.0016</sup> <sub>-0.0016</sub>	0.9683 <sup>+0.0007</sup> <sub>-0.0007</sub>	0.9793 <sup>+0.0152</sup> <sub>-0.0152</sub>
2.50-3.50	1.16-1.46	0.9563 <sup>+0.0009</sup> <sub>-0.0009</sub>	0.9721 <sup>+0.0004</sup> <sub>-0.0004</sub>	0.9838 <sup>+0.0094</sup> <sub>-0.0094</sub>
3.50-4.50	1.16-1.46	0.9517 <sup>+0.0007</sup> <sub>-0.0007</sub>	0.9717 <sup>+0.0003</sup> <sub>-0.0003</sub>	0.9795 <sup>+0.0039</sup> <sub>-0.0039</sub>

4.50-6.50	1.16-1.46	0.9565	$\begin{matrix} +0.0004 \\ -0.0004 \end{matrix}$	0.9739	$\begin{matrix} +0.0002 \\ -0.0002 \end{matrix}$	0.9821	$\begin{matrix} +0.0007 \\ -0.0007 \end{matrix}$
0.70-1.00	1.46-1.78	0.8978	$\begin{matrix} +0.0031 \\ -0.0031 \end{matrix}$	0.9459	$\begin{matrix} +0.0013 \\ -0.0013 \end{matrix}$	0.9491	$\begin{matrix} +0.0128 \\ -0.0129 \end{matrix}$
1.00-1.50	1.46-1.78	0.9308	$\begin{matrix} +0.0019 \\ -0.0019 \end{matrix}$	0.9631	$\begin{matrix} +0.0008 \\ -0.0008 \end{matrix}$	0.9665	$\begin{matrix} +0.0171 \\ -0.0172 \end{matrix}$
1.50-2.00	1.46-1.78	0.9499	$\begin{matrix} +0.0015 \\ -0.0016 \end{matrix}$	0.9653	$\begin{matrix} +0.0008 \\ -0.0008 \end{matrix}$	0.9840	$\begin{matrix} +0.0183 \\ -0.0183 \end{matrix}$
2.00-2.50	1.46-1.78	0.9476	$\begin{matrix} +0.0015 \\ -0.0015 \end{matrix}$	0.9685	$\begin{matrix} +0.0007 \\ -0.0007 \end{matrix}$	0.9784	$\begin{matrix} +0.0152 \\ -0.0152 \end{matrix}$
2.50-3.50	1.46-1.78	0.9569	$\begin{matrix} +0.0008 \\ -0.0008 \end{matrix}$	0.9732	$\begin{matrix} +0.0004 \\ -0.0004 \end{matrix}$	0.9833	$\begin{matrix} +0.0087 \\ -0.0087 \end{matrix}$
3.50-4.50	1.46-1.78	0.9535	$\begin{matrix} +0.0005 \\ -0.0006 \end{matrix}$	0.9716	$\begin{matrix} +0.0003 \\ -0.0003 \end{matrix}$	0.9814	$\begin{matrix} +0.0032 \\ -0.0032 \end{matrix}$
4.50-6.50	1.46-1.78	0.9563	$\begin{matrix} +0.0005 \\ -0.0005 \end{matrix}$	0.9740	$\begin{matrix} +0.0002 \\ -0.0002 \end{matrix}$	0.9819	$\begin{matrix} +0.0005 \\ -0.0005 \end{matrix}$
0.70-1.00	1.78-2.13	0.8341	$\begin{matrix} +0.0036 \\ -0.0036 \end{matrix}$	0.8894	$\begin{matrix} +0.0017 \\ -0.0017 \end{matrix}$	0.9378	$\begin{matrix} +0.0162 \\ -0.0163 \end{matrix}$
1.00-1.50	1.78-2.13	0.8982	$\begin{matrix} +0.0021 \\ -0.0022 \end{matrix}$	0.9352	$\begin{matrix} +0.0010 \\ -0.0010 \end{matrix}$	0.9604	$\begin{matrix} +0.0216 \\ -0.0216 \end{matrix}$
1.50-2.00	1.78-2.13	0.9141	$\begin{matrix} +0.0019 \\ -0.0019 \end{matrix}$	0.9394	$\begin{matrix} +0.0009 \\ -0.0009 \end{matrix}$	0.9731	$\begin{matrix} +0.0208 \\ -0.0208 \end{matrix}$
2.00-2.50	1.78-2.13	0.9187	$\begin{matrix} +0.0017 \\ -0.0017 \end{matrix}$	0.9421	$\begin{matrix} +0.0008 \\ -0.0008 \end{matrix}$	0.9751	$\begin{matrix} +0.0185 \\ -0.0185 \end{matrix}$
2.50-3.50	1.78-2.13	0.9250	$\begin{matrix} +0.0009 \\ -0.0009 \end{matrix}$	0.9454	$\begin{matrix} +0.0004 \\ -0.0005 \end{matrix}$	0.9785	$\begin{matrix} +0.0099 \\ -0.0099 \end{matrix}$
3.50-4.50	1.78-2.13	0.9133	$\begin{matrix} +0.0006 \\ -0.0006 \end{matrix}$	0.9442	$\begin{matrix} +0.0003 \\ -0.0003 \end{matrix}$	0.9672	$\begin{matrix} +0.0020 \\ -0.0020 \end{matrix}$
4.50-6.50	1.78-2.13	0.9391	$\begin{matrix} +0.0008 \\ -0.0008 \end{matrix}$	0.9626	$\begin{matrix} +0.0004 \\ -0.0004 \end{matrix}$	0.9756	$\begin{matrix} +0.0009 \\ -0.0009 \end{matrix}$
0.70-1.00	2.13-2.22	0.7239	$\begin{matrix} +0.0086 \\ -0.0088 \end{matrix}$	0.7950	$\begin{matrix} +0.0043 \\ -0.0044 \end{matrix}$	0.9105	$\begin{matrix} +0.0180 \\ -0.0181 \end{matrix}$
1.00-1.50	2.13-2.22	0.8552	$\begin{matrix} +0.0050 \\ -0.0052 \end{matrix}$	0.9285	$\begin{matrix} +0.0021 \\ -0.0021 \end{matrix}$	0.9210	$\begin{matrix} +0.0233 \\ -0.0233 \end{matrix}$
1.50-2.00	2.13-2.22	0.8684	$\begin{matrix} +0.0046 \\ -0.0047 \end{matrix}$	0.9550	$\begin{matrix} +0.0016 \\ -0.0016 \end{matrix}$	0.9093	$\begin{matrix} +0.0252 \\ -0.0252 \end{matrix}$
2.00-2.50	2.13-2.22	0.8750	$\begin{matrix} +0.0041 \\ -0.0042 \end{matrix}$	0.9688	$\begin{matrix} +0.0012 \\ -0.0012 \end{matrix}$	0.9032	$\begin{matrix} +0.0212 \\ -0.0212 \end{matrix}$
2.50-3.50	2.13-2.22	0.8917	$\begin{matrix} +0.0021 \\ -0.0021 \end{matrix}$	0.9783	$\begin{matrix} +0.0006 \\ -0.0006 \end{matrix}$	0.9115	$\begin{matrix} +0.0108 \\ -0.0108 \end{matrix}$
3.50-4.50	2.13-2.22	0.8823	$\begin{matrix} +0.0013 \\ -0.0013 \end{matrix}$	0.9795	$\begin{matrix} +0.0003 \\ -0.0003 \end{matrix}$	0.9008	$\begin{matrix} +0.0017 \\ -0.0017 \end{matrix}$
4.50-6.50	2.13-2.22	0.9323	$\begin{matrix} +0.0046 \\ -0.0049 \end{matrix}$	0.9863	$\begin{matrix} +0.0012 \\ -0.0013 \end{matrix}$	0.9453	$\begin{matrix} +0.0048 \\ -0.0051 \end{matrix}$
0.70-1.00	2.22-2.60	0.6864	$\begin{matrix} +0.0047 \\ -0.0047 \end{matrix}$	0.8183	$\begin{matrix} +0.0022 \\ -0.0022 \end{matrix}$	0.8388	$\begin{matrix} +0.0117 \\ -0.0117 \end{matrix}$
1.00-1.50	2.22-2.60	0.7468	$\begin{matrix} +0.0032 \\ -0.0033 \end{matrix}$	0.8542	$\begin{matrix} +0.0014 \\ -0.0015 \end{matrix}$	0.8743	$\begin{matrix} +0.0199 \\ -0.0199 \end{matrix}$
1.50-2.00	2.22-2.60	0.8369	$\begin{matrix} +0.0026 \\ -0.0026 \end{matrix}$	0.9291	$\begin{matrix} +0.0010 \\ -0.0010 \end{matrix}$	0.9008	$\begin{matrix} +0.0236 \\ -0.0236 \end{matrix}$
2.00-2.50	2.22-2.60	0.8741	$\begin{matrix} +0.0022 \\ -0.0022 \end{matrix}$	0.9459	$\begin{matrix} +0.0008 \\ -0.0008 \end{matrix}$	0.9241	$\begin{matrix} +0.0190 \\ -0.0190 \end{matrix}$
2.50-3.50	2.22-2.60	0.8947	$\begin{matrix} +0.0011 \\ -0.0011 \end{matrix}$	0.9518	$\begin{matrix} +0.0004 \\ -0.0004 \end{matrix}$	0.9400	$\begin{matrix} +0.0138 \\ -0.0138 \end{matrix}$
3.50-4.50	2.22-2.60	0.8960	$\begin{matrix} +0.0008 \\ -0.0008 \end{matrix}$	0.9650	$\begin{matrix} +0.0003 \\ -0.0003 \end{matrix}$	0.9285	$\begin{matrix} +0.0012 \\ -0.0012 \end{matrix}$
4.50-6.50	2.22-2.60	0.8875	$\begin{matrix} +0.0153 \\ -0.0172 \end{matrix}$	0.9597	$\begin{matrix} +0.0057 \\ -0.0065 \end{matrix}$	0.9247	$\begin{matrix} +0.0179 \\ -0.0198 \end{matrix}$

Table 5: Summary table of the data and MC efficiencies and the final correction values. Results are provided for  $\mu\text{ID}>0.9$  and the uncertainties reported are statistical and systematical.

p bin [GeV]	$\theta$ bin [rad]	Data efficiency	MC efficiency	Correction
0.70-1.00	0.40-0.64	0.7136 <sup>+0.0063</sup> <sub>-0.0064</sub>	0.7869 <sup>+0.0032</sup> <sub>-0.0032</sub>	0.9070 <sup>+0.0143</sup> <sub>-0.0143</sub>
1.00-1.50	0.40-0.64	0.7587 <sup>+0.0043</sup> <sub>-0.0044</sub>	0.8510 <sup>+0.0020</sup> <sub>-0.0020</sub>	0.8915 <sup>+0.0186</sup> <sub>-0.0186</sub>
1.50-2.00	0.40-0.64	0.8357 <sup>+0.0036</sup> <sub>-0.0036</sub>	0.9194 <sup>+0.0014</sup> <sub>-0.0015</sub>	0.9089 <sup>+0.0240</sup> <sub>-0.0240</sub>
2.00-2.50	0.40-0.64	0.8731 <sup>+0.0031</sup> <sub>-0.0031</sub>	0.9333 <sup>+0.0013</sup> <sub>-0.0013</sub>	0.9355 <sup>+0.0248</sup> <sub>-0.0248</sub>
2.50-3.50	0.40-0.64	0.8816 <sup>+0.0019</sup> <sub>-0.0020</sub>	0.9325 <sup>+0.0008</sup> <sub>-0.0008</sub>	0.9454 <sup>+0.0225</sup> <sub>-0.0225</sub>
3.50-4.50	0.40-0.64	0.8858 <sup>+0.0016</sup> <sub>-0.0016</sub>	0.9345 <sup>+0.0007</sup> <sub>-0.0007</sub>	0.9479 <sup>+0.0137</sup> <sub>-0.0137</sub>
4.50-6.50	0.40-0.64	0.9066 <sup>+0.0006</sup> <sub>-0.0006</sub>	0.9414 <sup>+0.0003</sup> <sub>-0.0003</sub>	0.9630 <sup>+0.0030</sup> <sub>-0.0030</sub>
0.70-1.00	0.64-0.82	0.5190 <sup>+0.0073</sup> <sub>-0.0073</sub>	0.7216 <sup>+0.0037</sup> <sub>-0.0037</sub>	0.7193 <sup>+0.0114</sup> <sub>-0.0114</sub>
1.00-1.50	0.64-0.82	0.7928 <sup>+0.0043</sup> <sub>-0.0043</sub>	0.9118 <sup>+0.0017</sup> <sub>-0.0017</sub>	0.8695 <sup>+0.0207</sup> <sub>-0.0207</sub>
1.50-2.00	0.64-0.82	0.8756 <sup>+0.0033</sup> <sub>-0.0034</sub>	0.9532 <sup>+0.0012</sup> <sub>-0.0012</sub>	0.9187 <sup>+0.0267</sup> <sub>-0.0267</sub>
2.00-2.50	0.64-0.82	0.8643 <sup>+0.0033</sup> <sub>-0.0034</sub>	0.9466 <sup>+0.0012</sup> <sub>-0.0012</sub>	0.9131 <sup>+0.0300</sup> <sub>-0.0300</sub>
2.50-3.50	0.64-0.82	0.8624 <sup>+0.0021</sup> <sub>-0.0022</sub>	0.9525 <sup>+0.0007</sup> <sub>-0.0008</sub>	0.9055 <sup>+0.0226</sup> <sub>-0.0226</sub>
3.50-4.50	0.64-0.82	0.8544 <sup>+0.0018</sup> <sub>-0.0018</sub>	0.9521 <sup>+0.0006</sup> <sub>-0.0006</sub>	0.8974 <sup>+0.0129</sup> <sub>-0.0129</sub>
4.50-6.50	0.64-0.82	0.8327 <sup>+0.0008</sup> <sub>-0.0008</sub>	0.9598 <sup>+0.0002</sup> <sub>-0.0002</sub>	0.8676 <sup>+0.0020</sup> <sub>-0.0020</sub>
0.70-1.00	0.82-1.16	0.6879 <sup>+0.0046</sup> <sub>-0.0047</sub>	0.8300 <sup>+0.0022</sup> <sub>-0.0022</sub>	0.8288 <sup>+0.0100</sup> <sub>-0.0100</sub>
1.00-1.50	0.82-1.16	0.8731 <sup>+0.0025</sup> <sub>-0.0025</sub>	0.9476 <sup>+0.0010</sup> <sub>-0.0010</sub>	0.9213 <sup>+0.0167</sup> <sub>-0.0167</sub>
1.50-2.00	0.82-1.16	0.9250 <sup>+0.0019</sup> <sub>-0.0019</sub>	0.9559 <sup>+0.0008</sup> <sub>-0.0009</sub>	0.9676 <sup>+0.0209</sup> <sub>-0.0209</sub>
2.00-2.50	0.82-1.16	0.9231 <sup>+0.0018</sup> <sub>-0.0018</sub>	0.9505 <sup>+0.0009</sup> <sub>-0.0009</sub>	0.9711 <sup>+0.0182</sup> <sub>-0.0182</sub>
2.50-3.50	0.82-1.16	0.9262 <sup>+0.0011</sup> <sub>-0.0011</sub>	0.9529 <sup>+0.0005</sup> <sub>-0.0005</sub>	0.9720 <sup>+0.0136</sup> <sub>-0.0136</sub>
3.50-4.50	0.82-1.16	0.9237 <sup>+0.0009</sup> <sub>-0.0009</sub>	0.9516 <sup>+0.0004</sup> <sub>-0.0004</sub>	0.9707 <sup>+0.0059</sup> <sub>-0.0059</sub>
4.50-6.50	0.82-1.16	0.9227 <sup>+0.0004</sup> <sub>-0.0004</sub>	0.9502 <sup>+0.0002</sup> <sub>-0.0002</sub>	0.9711 <sup>+0.0013</sup> <sub>-0.0013</sub>
0.70-1.00	1.16-1.46	0.7997 <sup>+0.0042</sup> <sub>-0.0043</sub>	0.9116 <sup>+0.0017</sup> <sub>-0.0018</sub>	0.8772 <sup>+0.0093</sup> <sub>-0.0093</sub>
1.00-1.50	1.16-1.46	0.9054 <sup>+0.0023</sup> <sub>-0.0023</sub>	0.9552 <sup>+0.0009</sup> <sub>-0.0010</sub>	0.9478 <sup>+0.0138</sup> <sub>-0.0138</sub>
1.50-2.00	1.16-1.46	0.9404 <sup>+0.0018</sup> <sub>-0.0018</sub>	0.9603 <sup>+0.0008</sup> <sub>-0.0009</sub>	0.9793 <sup>+0.0174</sup> <sub>-0.0174</sub>
2.00-2.50	1.16-1.46	0.9409 <sup>+0.0017</sup> <sub>-0.0017</sub>	0.9653 <sup>+0.0008</sup> <sub>-0.0008</sub>	0.9747 <sup>+0.0153</sup> <sub>-0.0153</sub>
2.50-3.50	1.16-1.46	0.9481 <sup>+0.0010</sup> <sub>-0.0010</sub>	0.9684 <sup>+0.0004</sup> <sub>-0.0005</sub>	0.9791 <sup>+0.0094</sup> <sub>-0.0094</sub>
3.50-4.50	1.16-1.46	0.9425 <sup>+0.0007</sup> <sub>-0.0007</sub>	0.9669 <sup>+0.0003</sup> <sub>-0.0003</sub>	0.9748 <sup>+0.0039</sup> <sub>-0.0039</sub>
4.50-6.50	1.16-1.46	0.9460 <sup>+0.0004</sup> <sub>-0.0004</sub>	0.9682 <sup>+0.0002</sup> <sub>-0.0002</sub>	0.9771 <sup>+0.0007</sup> <sub>-0.0007</sub>
0.70-1.00	1.46-1.78	0.8551 <sup>+0.0036</sup> <sub>-0.0036</sub>	0.9272 <sup>+0.0015</sup> <sub>-0.0015</sub>	0.9223 <sup>+0.0129</sup> <sub>-0.0129</sub>
1.00-1.50	1.46-1.78	0.9230 <sup>+0.0020</sup> <sub>-0.0020</sub>	0.9590 <sup>+0.0009</sup> <sub>-0.0009</sub>	0.9624 <sup>+0.0172</sup> <sub>-0.0172</sub>

1.50-2.00	1.46-1.78	0.9428	$\begin{matrix} +0.0016 \\ -0.0017 \end{matrix}$	0.9629	$\begin{matrix} +0.0008 \\ -0.0008 \end{matrix}$	0.9792	$\begin{matrix} +0.0182 \\ -0.0182 \end{matrix}$
2.00-2.50	1.46-1.78	0.9414	$\begin{matrix} +0.0016 \\ -0.0016 \end{matrix}$	0.9657	$\begin{matrix} +0.0007 \\ -0.0007 \end{matrix}$	0.9748	$\begin{matrix} +0.0152 \\ -0.0152 \end{matrix}$
2.50-3.50	1.46-1.78	0.9489	$\begin{matrix} +0.0009 \\ -0.0009 \end{matrix}$	0.9696	$\begin{matrix} +0.0004 \\ -0.0004 \end{matrix}$	0.9786	$\begin{matrix} +0.0087 \\ -0.0087 \end{matrix}$
3.50-4.50	1.46-1.78	0.9433	$\begin{matrix} +0.0006 \\ -0.0006 \end{matrix}$	0.9662	$\begin{matrix} +0.0003 \\ -0.0003 \end{matrix}$	0.9763	$\begin{matrix} +0.0032 \\ -0.0032 \end{matrix}$
4.50-6.50	1.46-1.78	0.9458	$\begin{matrix} +0.0005 \\ -0.0005 \end{matrix}$	0.9674	$\begin{matrix} +0.0002 \\ -0.0002 \end{matrix}$	0.9777	$\begin{matrix} +0.0006 \\ -0.0006 \end{matrix}$
0.70-1.00	1.78-2.13	0.7539	$\begin{matrix} +0.0041 \\ -0.0042 \end{matrix}$	0.8385	$\begin{matrix} +0.0020 \\ -0.0020 \end{matrix}$	0.8991	$\begin{matrix} +0.0157 \\ -0.0158 \end{matrix}$
1.00-1.50	1.78-2.13	0.8711	$\begin{matrix} +0.0024 \\ -0.0024 \end{matrix}$	0.9178	$\begin{matrix} +0.0011 \\ -0.0011 \end{matrix}$	0.9492	$\begin{matrix} +0.0213 \\ -0.0213 \end{matrix}$
1.50-2.00	1.78-2.13	0.8912	$\begin{matrix} +0.0021 \\ -0.0021 \end{matrix}$	0.9227	$\begin{matrix} +0.0010 \\ -0.0010 \end{matrix}$	0.9659	$\begin{matrix} +0.0204 \\ -0.0204 \end{matrix}$
2.00-2.50	1.78-2.13	0.8914	$\begin{matrix} +0.0019 \\ -0.0019 \end{matrix}$	0.9235	$\begin{matrix} +0.0009 \\ -0.0009 \end{matrix}$	0.9653	$\begin{matrix} +0.0181 \\ -0.0181 \end{matrix}$
2.50-3.50	1.78-2.13	0.8966	$\begin{matrix} +0.0011 \\ -0.0011 \end{matrix}$	0.9235	$\begin{matrix} +0.0005 \\ -0.0005 \end{matrix}$	0.9708	$\begin{matrix} +0.0098 \\ -0.0098 \end{matrix}$
3.50-4.50	1.78-2.13	0.8830	$\begin{matrix} +0.0007 \\ -0.0007 \end{matrix}$	0.9161	$\begin{matrix} +0.0003 \\ -0.0003 \end{matrix}$	0.9639	$\begin{matrix} +0.0020 \\ -0.0020 \end{matrix}$
4.50-6.50	1.78-2.13	0.9228	$\begin{matrix} +0.0009 \\ -0.0009 \end{matrix}$	0.9491	$\begin{matrix} +0.0004 \\ -0.0004 \end{matrix}$	0.9723	$\begin{matrix} +0.0010 \\ -0.0010 \end{matrix}$
0.70-1.00	2.13-2.22	0.4273	$\begin{matrix} +0.0096 \\ -0.0096 \end{matrix}$	0.6034	$\begin{matrix} +0.0053 \\ -0.0053 \end{matrix}$	0.7081	$\begin{matrix} +0.0147 \\ -0.0146 \end{matrix}$
1.00-1.50	2.13-2.22	0.7775	$\begin{matrix} +0.0060 \\ -0.0061 \end{matrix}$	0.8949	$\begin{matrix} +0.0024 \\ -0.0025 \end{matrix}$	0.8689	$\begin{matrix} +0.0224 \\ -0.0224 \end{matrix}$
1.50-2.00	2.13-2.22	0.7842	$\begin{matrix} +0.0056 \\ -0.0057 \end{matrix}$	0.9385	$\begin{matrix} +0.0018 \\ -0.0019 \end{matrix}$	0.8355	$\begin{matrix} +0.0231 \\ -0.0232 \end{matrix}$
2.00-2.50	2.13-2.22	0.7711	$\begin{matrix} +0.0052 \\ -0.0053 \end{matrix}$	0.9498	$\begin{matrix} +0.0015 \\ -0.0015 \end{matrix}$	0.8119	$\begin{matrix} +0.0190 \\ -0.0191 \end{matrix}$
2.50-3.50	2.13-2.22	0.7808	$\begin{matrix} +0.0028 \\ -0.0028 \end{matrix}$	0.9637	$\begin{matrix} +0.0007 \\ -0.0007 \end{matrix}$	0.8102	$\begin{matrix} +0.0099 \\ -0.0099 \end{matrix}$
3.50-4.50	2.13-2.22	0.7601	$\begin{matrix} +0.0018 \\ -0.0018 \end{matrix}$	0.9632	$\begin{matrix} +0.0004 \\ -0.0004 \end{matrix}$	0.7892	$\begin{matrix} +0.0020 \\ -0.0020 \end{matrix}$
4.50-6.50	2.13-2.22	0.8542	$\begin{matrix} +0.0065 \\ -0.0068 \end{matrix}$	0.9807	$\begin{matrix} +0.0014 \\ -0.0015 \end{matrix}$	0.8710	$\begin{matrix} +0.0067 \\ -0.0069 \end{matrix}$
0.70-1.00	2.22-2.60	0.4091	$\begin{matrix} +0.0050 \\ -0.0050 \end{matrix}$	0.5988	$\begin{matrix} +0.0027 \\ -0.0027 \end{matrix}$	0.6831	$\begin{matrix} +0.0095 \\ -0.0095 \end{matrix}$
1.00-1.50	2.22-2.60	0.6552	$\begin{matrix} +0.0035 \\ -0.0036 \end{matrix}$	0.7995	$\begin{matrix} +0.0016 \\ -0.0017 \end{matrix}$	0.8195	$\begin{matrix} +0.0182 \\ -0.0182 \end{matrix}$
1.50-2.00	2.22-2.60	0.8005	$\begin{matrix} +0.0028 \\ -0.0029 \end{matrix}$	0.9205	$\begin{matrix} +0.0010 \\ -0.0010 \end{matrix}$	0.8697	$\begin{matrix} +0.0227 \\ -0.0227 \end{matrix}$
2.00-2.50	2.22-2.60	0.8407	$\begin{matrix} +0.0024 \\ -0.0024 \end{matrix}$	0.9350	$\begin{matrix} +0.0009 \\ -0.0009 \end{matrix}$	0.8991	$\begin{matrix} +0.0184 \\ -0.0184 \end{matrix}$
2.50-3.50	2.22-2.60	0.8596	$\begin{matrix} +0.0013 \\ -0.0013 \end{matrix}$	0.9380	$\begin{matrix} +0.0005 \\ -0.0005 \end{matrix}$	0.9165	$\begin{matrix} +0.0134 \\ -0.0134 \end{matrix}$
3.50-4.50	2.22-2.60	0.8502	$\begin{matrix} +0.0010 \\ -0.0010 \end{matrix}$	0.9436	$\begin{matrix} +0.0004 \\ -0.0004 \end{matrix}$	0.9010	$\begin{matrix} +0.0013 \\ -0.0013 \end{matrix}$
4.50-6.50	2.22-2.60	0.7757	$\begin{matrix} +0.0204 \\ -0.0217 \end{matrix}$	0.9295	$\begin{matrix} +0.0075 \\ -0.0082 \end{matrix}$	0.8345	$\begin{matrix} +0.0226 \\ -0.0241 \end{matrix}$

Table 6: Summary table of the data and MC efficiencies and the final correction values. Results are provided for  $\mu\text{ID}>0.95$  and the uncertainties reported are statistical and systematical.

p bin [GeV]	$\theta$ bin [rad]	Data efficiency	MC efficiency	Correction
0.70-1.00	0.40-0.64	0.6655 <sup>+0.0066</sup> <sub>-0.0066</sub>	0.7398 <sup>+0.0034</sup> <sub>-0.0034</sub>	0.8995 <sup>+0.0138</sup> <sub>-0.0138</sub>
1.00-1.50	0.40-0.64	0.7281 <sup>+0.0045</sup> <sub>-0.0045</sub>	0.8249 <sup>+0.0021</sup> <sub>-0.0022</sub>	0.8825 <sup>+0.0179</sup> <sub>-0.0179</sub>
1.50-2.00	0.40-0.64	0.8220 <sup>+0.0037</sup> <sub>-0.0038</sub>	0.9149 <sup>+0.0015</sup> <sub>-0.0015</sub>	0.8985 <sup>+0.0237</sup> <sub>-0.0237</sub>
2.00-2.50	0.40-0.64	0.8651 <sup>+0.0032</sup> <sub>-0.0032</sub>	0.9314 <sup>+0.0013</sup> <sub>-0.0013</sub>	0.9288 <sup>+0.0248</sup> <sub>-0.0248</sub>
2.50-3.50	0.40-0.64	0.8761 <sup>+0.0020</sup> <sub>-0.0020</sub>	0.9314 <sup>+0.0008</sup> <sub>-0.0008</sub>	0.9406 <sup>+0.0225</sup> <sub>-0.0225</sub>
3.50-4.50	0.40-0.64	0.8795 <sup>+0.0016</sup> <sub>-0.0017</sub>	0.9336 <sup>+0.0007</sup> <sub>-0.0007</sub>	0.9420 <sup>+0.0136</sup> <sub>-0.0136</sub>
4.50-6.50	0.40-0.64	0.9013 <sup>+0.0006</sup> <sub>-0.0007</sub>	0.9404 <sup>+0.0003</sup> <sub>-0.0003</sub>	0.9584 <sup>+0.0029</sup> <sub>-0.0029</sub>
0.70-1.00	0.64-0.82	0.4645 <sup>+0.0073</sup> <sub>-0.0072</sub>	0.6847 <sup>+0.0038</sup> <sub>-0.0038</sub>	0.6783 <sup>+0.0109</sup> <sub>-0.0109</sub>
1.00-1.50	0.64-0.82	0.7730 <sup>+0.0044</sup> <sub>-0.0045</sub>	0.9052 <sup>+0.0017</sup> <sub>-0.0018</sub>	0.8539 <sup>+0.0203</sup> <sub>-0.0203</sub>
1.50-2.00	0.64-0.82	0.8649 <sup>+0.0034</sup> <sub>-0.0035</sub>	0.9506 <sup>+0.0012</sup> <sub>-0.0012</sub>	0.9098 <sup>+0.0264</sup> <sub>-0.0264</sub>
2.00-2.50	0.64-0.82	0.8478 <sup>+0.0035</sup> <sub>-0.0035</sub>	0.9421 <sup>+0.0013</sup> <sub>-0.0013</sub>	0.8998 <sup>+0.0296</sup> <sub>-0.0296</sub>
2.50-3.50	0.64-0.82	0.8420 <sup>+0.0023</sup> <sub>-0.0023</sub>	0.9462 <sup>+0.0008</sup> <sub>-0.0008</sub>	0.8898 <sup>+0.0222</sup> <sub>-0.0222</sub>
3.50-4.50	0.64-0.82	0.8317 <sup>+0.0019</sup> <sub>-0.0019</sub>	0.9455 <sup>+0.0007</sup> <sub>-0.0007</sub>	0.8796 <sup>+0.0126</sup> <sub>-0.0126</sub>
4.50-6.50	0.64-0.82	0.8063 <sup>+0.0008</sup> <sub>-0.0008</sub>	0.9530 <sup>+0.0003</sup> <sub>-0.0003</sub>	0.8461 <sup>+0.0020</sup> <sub>-0.0020</sub>
0.70-1.00	0.82-1.16	0.6507 <sup>+0.0048</sup> <sub>-0.0048</sub>	0.8102 <sup>+0.0023</sup> <sub>-0.0023</sub>	0.8031 <sup>+0.0097</sup> <sub>-0.0097</sub>
1.00-1.50	0.82-1.16	0.8664 <sup>+0.0025</sup> <sub>-0.0026</sub>	0.9445 <sup>+0.0010</sup> <sub>-0.0010</sub>	0.9173 <sup>+0.0167</sup> <sub>-0.0167</sub>
1.50-2.00	0.82-1.16	0.9211 <sup>+0.0019</sup> <sub>-0.0020</sub>	0.9540 <sup>+0.0009</sup> <sub>-0.0009</sub>	0.9655 <sup>+0.0208</sup> <sub>-0.0208</sub>
2.00-2.50	0.82-1.16	0.9166 <sup>+0.0019</sup> <sub>-0.0019</sub>	0.9456 <sup>+0.0009</sup> <sub>-0.0009</sub>	0.9692 <sup>+0.0182</sup> <sub>-0.0182</sub>
2.50-3.50	0.82-1.16	0.9199 <sup>+0.0012</sup> <sub>-0.0012</sub>	0.9475 <sup>+0.0006</sup> <sub>-0.0006</sub>	0.9709 <sup>+0.0136</sup> <sub>-0.0136</sub>
3.50-4.50	0.82-1.16	0.9177 <sup>+0.0009</sup> <sub>-0.0009</sub>	0.9462 <sup>+0.0004</sup> <sub>-0.0004</sub>	0.9698 <sup>+0.0059</sup> <sub>-0.0059</sub>
4.50-6.50	0.82-1.16	0.9151 <sup>+0.0004</sup> <sub>-0.0004</sub>	0.9435 <sup>+0.0002</sup> <sub>-0.0002</sub>	0.9699 <sup>+0.0013</sup> <sub>-0.0013</sub>
0.70-1.00	1.16-1.46	0.7725 <sup>+0.0044</sup> <sub>-0.0045</sub>	0.9002 <sup>+0.0018</sup> <sub>-0.0019</sub>	0.8582 <sup>+0.0092</sup> <sub>-0.0092</sub>
1.00-1.50	1.16-1.46	0.9003 <sup>+0.0023</sup> <sub>-0.0024</sub>	0.9524 <sup>+0.0010</sup> <sub>-0.0010</sub>	0.9453 <sup>+0.0138</sup> <sub>-0.0138</sub>
1.50-2.00	1.16-1.46	0.9382 <sup>+0.0018</sup> <sub>-0.0019</sub>	0.9590 <sup>+0.0009</sup> <sub>-0.0009</sub>	0.9783 <sup>+0.0174</sup> <sub>-0.0175</sub>
2.00-2.50	1.16-1.46	0.9390 <sup>+0.0017</sup> <sub>-0.0017</sub>	0.9645 <sup>+0.0008</sup> <sub>-0.0008</sub>	0.9735 <sup>+0.0153</sup> <sub>-0.0153</sub>
2.50-3.50	1.16-1.46	0.9462 <sup>+0.0010</sup> <sub>-0.0010</sub>	0.9674 <sup>+0.0005</sup> <sub>-0.0005</sub>	0.9780 <sup>+0.0094</sup> <sub>-0.0094</sub>
3.50-4.50	1.16-1.46	0.9410 <sup>+0.0007</sup> <sub>-0.0008</sub>	0.9660 <sup>+0.0003</sup> <sub>-0.0003</sub>	0.9742 <sup>+0.0039</sup> <sub>-0.0039</sub>
4.50-6.50	1.16-1.46	0.9446 <sup>+0.0004</sup> <sub>-0.0004</sub>	0.9672 <sup>+0.0002</sup> <sub>-0.0002</sub>	0.9766 <sup>+0.0007</sup> <sub>-0.0007</sub>
0.70-1.00	1.46-1.78	0.8409 <sup>+0.0037</sup> <sub>-0.0038</sub>	0.9208 <sup>+0.0016</sup> <sub>-0.0016</sub>	0.9132 <sup>+0.0129</sup> <sub>-0.0129</sub>
1.00-1.50	1.46-1.78	0.9195 <sup>+0.0020</sup> <sub>-0.0021</sub>	0.9574 <sup>+0.0009</sup> <sub>-0.0009</sub>	0.9604 <sup>+0.0171</sup> <sub>-0.0171</sub>

1.50-2.00	1.46-1.78	0.9404	$\begin{matrix} +0.0017 \\ -0.0017 \end{matrix}$	0.9619	$\begin{matrix} +0.0008 \\ -0.0008 \end{matrix}$	0.9776	$\begin{matrix} +0.0181 \\ -0.0181 \end{matrix}$
2.00-2.50	1.46-1.78	0.9393	$\begin{matrix} +0.0016 \\ -0.0016 \end{matrix}$	0.9647	$\begin{matrix} +0.0007 \\ -0.0007 \end{matrix}$	0.9737	$\begin{matrix} +0.0153 \\ -0.0153 \end{matrix}$
2.50-3.50	1.46-1.78	0.9469	$\begin{matrix} +0.0009 \\ -0.0009 \end{matrix}$	0.9686	$\begin{matrix} +0.0004 \\ -0.0004 \end{matrix}$	0.9776	$\begin{matrix} +0.0087 \\ -0.0087 \end{matrix}$
3.50-4.50	1.46-1.78	0.9417	$\begin{matrix} +0.0006 \\ -0.0006 \end{matrix}$	0.9653	$\begin{matrix} +0.0003 \\ -0.0003 \end{matrix}$	0.9756	$\begin{matrix} +0.0032 \\ -0.0032 \end{matrix}$
4.50-6.50	1.46-1.78	0.9440	$\begin{matrix} +0.0005 \\ -0.0005 \end{matrix}$	0.9664	$\begin{matrix} +0.0002 \\ -0.0002 \end{matrix}$	0.9768	$\begin{matrix} +0.0006 \\ -0.0006 \end{matrix}$
0.70-1.00	1.78-2.13	0.7316	$\begin{matrix} +0.0043 \\ -0.0043 \end{matrix}$	0.8260	$\begin{matrix} +0.0021 \\ -0.0021 \end{matrix}$	0.8858	$\begin{matrix} +0.0156 \\ -0.0156 \end{matrix}$
1.00-1.50	1.78-2.13	0.8641	$\begin{matrix} +0.0024 \\ -0.0024 \end{matrix}$	0.9123	$\begin{matrix} +0.0011 \\ -0.0011 \end{matrix}$	0.9471	$\begin{matrix} +0.0213 \\ -0.0213 \end{matrix}$
1.50-2.00	1.78-2.13	0.8829	$\begin{matrix} +0.0021 \\ -0.0022 \end{matrix}$	0.9171	$\begin{matrix} +0.0010 \\ -0.0011 \end{matrix}$	0.9627	$\begin{matrix} +0.0202 \\ -0.0202 \end{matrix}$
2.00-2.50	1.78-2.13	0.8842	$\begin{matrix} +0.0020 \\ -0.0020 \end{matrix}$	0.9172	$\begin{matrix} +0.0010 \\ -0.0010 \end{matrix}$	0.9640	$\begin{matrix} +0.0180 \\ -0.0181 \end{matrix}$
2.50-3.50	1.78-2.13	0.8891	$\begin{matrix} +0.0011 \\ -0.0011 \end{matrix}$	0.9169	$\begin{matrix} +0.0005 \\ -0.0005 \end{matrix}$	0.9697	$\begin{matrix} +0.0097 \\ -0.0097 \end{matrix}$
3.50-4.50	1.78-2.13	0.8762	$\begin{matrix} +0.0007 \\ -0.0007 \end{matrix}$	0.9095	$\begin{matrix} +0.0004 \\ -0.0004 \end{matrix}$	0.9633	$\begin{matrix} +0.0020 \\ -0.0020 \end{matrix}$
4.50-6.50	1.78-2.13	0.9190	$\begin{matrix} +0.0009 \\ -0.0009 \end{matrix}$	0.9465	$\begin{matrix} +0.0004 \\ -0.0004 \end{matrix}$	0.9710	$\begin{matrix} +0.0010 \\ -0.0010 \end{matrix}$
0.70-1.00	2.13-2.22	0.3598	$\begin{matrix} +0.0094 \\ -0.0093 \end{matrix}$	0.5313	$\begin{matrix} +0.0054 \\ -0.0054 \end{matrix}$	0.6772	$\begin{matrix} +0.0138 \\ -0.0137 \end{matrix}$
1.00-1.50	2.13-2.22	0.7408	$\begin{matrix} +0.0063 \\ -0.0064 \end{matrix}$	0.8768	$\begin{matrix} +0.0026 \\ -0.0027 \end{matrix}$	0.8449	$\begin{matrix} +0.0215 \\ -0.0215 \end{matrix}$
1.50-2.00	2.13-2.22	0.7547	$\begin{matrix} +0.0058 \\ -0.0059 \end{matrix}$	0.9305	$\begin{matrix} +0.0019 \\ -0.0020 \end{matrix}$	0.8111	$\begin{matrix} +0.0226 \\ -0.0226 \end{matrix}$
2.00-2.50	2.13-2.22	0.7203	$\begin{matrix} +0.0056 \\ -0.0057 \end{matrix}$	0.9421	$\begin{matrix} +0.0016 \\ -0.0016 \end{matrix}$	0.7646	$\begin{matrix} +0.0181 \\ -0.0181 \end{matrix}$
2.50-3.50	2.13-2.22	0.7269	$\begin{matrix} +0.0030 \\ -0.0030 \end{matrix}$	0.9552	$\begin{matrix} +0.0008 \\ -0.0008 \end{matrix}$	0.7610	$\begin{matrix} +0.0093 \\ -0.0093 \end{matrix}$
3.50-4.50	2.13-2.22	0.7044	$\begin{matrix} +0.0019 \\ -0.0019 \end{matrix}$	0.9552	$\begin{matrix} +0.0005 \\ -0.0005 \end{matrix}$	0.7375	$\begin{matrix} +0.0021 \\ -0.0021 \end{matrix}$
4.50-6.50	2.13-2.22	0.8092	$\begin{matrix} +0.0073 \\ -0.0075 \end{matrix}$	0.9753	$\begin{matrix} +0.0015 \\ -0.0016 \end{matrix}$	0.8297	$\begin{matrix} +0.0075 \\ -0.0077 \end{matrix}$
0.70-1.00	2.22-2.60	0.3680	$\begin{matrix} +0.0049 \\ -0.0049 \end{matrix}$	0.5780	$\begin{matrix} +0.0028 \\ -0.0028 \end{matrix}$	0.6367	$\begin{matrix} +0.0089 \\ -0.0089 \end{matrix}$
1.00-1.50	2.22-2.60	0.6366	$\begin{matrix} +0.0036 \\ -0.0036 \end{matrix}$	0.7936	$\begin{matrix} +0.0017 \\ -0.0017 \end{matrix}$	0.8022	$\begin{matrix} +0.0177 \\ -0.0177 \end{matrix}$
1.50-2.00	2.22-2.60	0.7881	$\begin{matrix} +0.0029 \\ -0.0029 \end{matrix}$	0.9179	$\begin{matrix} +0.0011 \\ -0.0011 \end{matrix}$	0.8586	$\begin{matrix} +0.0223 \\ -0.0223 \end{matrix}$
2.00-2.50	2.22-2.60	0.8289	$\begin{matrix} +0.0025 \\ -0.0025 \end{matrix}$	0.9335	$\begin{matrix} +0.0009 \\ -0.0009 \end{matrix}$	0.8880	$\begin{matrix} +0.0181 \\ -0.0181 \end{matrix}$
2.50-3.50	2.22-2.60	0.8482	$\begin{matrix} +0.0013 \\ -0.0013 \end{matrix}$	0.9368	$\begin{matrix} +0.0005 \\ -0.0005 \end{matrix}$	0.9055	$\begin{matrix} +0.0132 \\ -0.0132 \end{matrix}$
3.50-4.50	2.22-2.60	0.8356	$\begin{matrix} +0.0010 \\ -0.0010 \end{matrix}$	0.9422	$\begin{matrix} +0.0004 \\ -0.0004 \end{matrix}$	0.8868	$\begin{matrix} +0.0013 \\ -0.0014 \end{matrix}$
4.50-6.50	2.22-2.60	0.7324	$\begin{matrix} +0.0217 \\ -0.0228 \end{matrix}$	0.9195	$\begin{matrix} +0.0079 \\ -0.0087 \end{matrix}$	0.7965	$\begin{matrix} +0.0239 \\ -0.0252 \end{matrix}$

# Bibliography

- [1] M. Giffels, J. Kallarackal, M. Krämer, B. O’Leary, and A. Stahl. Lepton-flavor-violating decay  $\tau \rightarrow \mu\mu\mu$  at the cern lhc. *Physical Review D*, 77(7), Apr 2008.
- [2] Lorenzo Calibbi and Giovanni Signorelli. Charged Lepton Flavour Violation: An Experimental and Theoretical Introduction. *Riv. Nuovo Cim.*, 41(2):71–174, 2018.
- [3] Ana M. Teixeira. Lepton flavour violation and neutrino physics: beyond the Standard Model. In *28th Rencontres de Blois on Particle Physics and Cosmology*, 12 2016.
- [4] Kazunori Akai, Kazuro Furukawa, and Haruyo Koiso. Superkekb collider. *Nuclear Instruments and Methods in Physics Research Section A: Accelerators, Spectrometers, Detectors and Associated Equipment*, 907:188–199, Nov 2018.
- [5] A. Paladino. Beam background evaluation at SuperKEKB and Belle II. *JINST*, 15(07):C07023, 2020.
- [6] M. Leon. *Particle physics: an introduction [by] M. Leon*. Academic Press New York, 1973.
- [7] D.H. Perkins. *Introduction to high energy physics*. 1 1982.
- [8] Jeremy Bernstein. Spontaneous symmetry breaking, gauge theories, the higgs mechanism and all that. *Rev. Mod. Phys.*, 46:7–48, Jan 1974.
- [9] P.A. Zyla et al. Review of Particle Physics. *PTEP*, 2020(8):083C01, 2020.
- [10] Nicola Cabibbo. Unitary symmetry and leptonic decays. *Phys. Rev. Lett.*, 10:531–533, 1963.

- [11] Q.R. Ahmad et al. Measurement of the rate of  $\nu_e + d \rightarrow p + p + e^-$  interactions produced by  $^8B$  solar neutrinos at the Sudbury Neutrino Observatory. *Phys. Rev. Lett.*, 87:071301, 2001.
- [12] Y. Fukuda, T. Hayakawa, E. Ichihara, K. Inoue, K. Ishihara, H. Ishino, Y. Itow, T. Kajita, J. Kameda, S. Kasuga, and et al. Evidence for oscillation of atmospheric neutrinos. *Physical Review Letters*, 81(8):1562–1567, Aug 1998.
- [13] G. Danby, J-M. Gaillard, K. Goulianos, L. M. Lederman, N. Mistry, M. Schwartz, and J. Steinberger. Observation of high-energy neutrino reactions and the existence of two kinds of neutrinos. *Phys. Rev. Lett.*, 9:36–44, Jul 1962.
- [14] K. Eguchi, S. Enomoto, K. Furuno, J. Goldman, H. Hanada, H. Ikeda, K. Ikeda, K. Inoue, K. Ishihara, W. Itoh, and et al. First results from kamland: Evidence for reactor antineutrino disappearance. *Physical Review Letters*, 90(2), Jan 2003.
- [15] C. Giganti, S. Lavignac, and M. Zito. Neutrino oscillations: The rise of the pmns paradigm. *Progress in Particle and Nuclear Physics*, 98:1–54, Jan 2018.
- [16] Ivan Esteban, M. C. Gonzalez-Garcia, Michele Maltoni, Thomas Schwetz, and Albert Zhou. The fate of hints: updated global analysis of three-flavor neutrino oscillations. *Journal of High Energy Physics*, 2020(9):178, 2020.
- [17] G. Hernández-Tomé, G. López Castro, and P. Roig. Flavor violating leptonic decays of  $\tau$  and  $\mu$  leptons in the Standard Model with massive neutrinos. *Eur. Phys. J. C*, 79(1):84, 2019. [Erratum: *Eur.Phys.J.C* 80, 438 (2020)].
- [18] STEPHEN P. MARTIN. A supersymmetry primer. *Advanced Series on Directions in High Energy Physics*, page 1–98, Jul 1998.
- [19] Ian Low. T parity and the littlest higgs. *Journal of High Energy Physics*, 2004(10):067–067, Oct 2004.
- [20] R. Barbier, C. Bérat, M. Besanc con, M. Chemtob, A. Deandrea, E. Dudas, P. Fayet, S. Lavignac, G. Moreau, E. Perez, and et al. R-parity-violating supersymmetry. *Physics Reports*, 420(1-6):1–195, Nov 2005.

- [21] Chongxing Yue, Yanming Zhang, and Lanjun Liu. Non-universal gauge bosons  $z'$  and lepton flavor-violating tau decays. *Physics Letters B*, 547(3-4):252–256, Nov 2002.
- [22] S.T Petcov, S Profumo, Y Takanishi, and C.E Yaguna. Charged lepton flavor violating decays: leading logarithmic approximation versus full rg results. *Nuclear Physics B*, 676(1-2):453–480, Jan 2004.
- [23] K. S. Babu and Christopher Kolda. Higgs-mediated  $\tau \rightarrow 3\mu$  in the supersymmetric seesaw model. *Physical Review Letters*, 89(24), Nov 2002.
- [24] Takeshi Fukuyama, Tatsuru Kikuchi, and Nobuchika Okada. Lepton flavor violating processes and muon  $g-2$  in the minimal supersymmetric  $so(10)$  model. *Phys. Rev. D*, 68:033012, Aug 2003.
- [25] Andrea Brignole and Anna Rossi. Lepton flavour violating decays of supersymmetric higgs bosons. *Physics Letters B*, 566(3-4):217–225, Jul 2003.
- [26] G. Cvetič, C. Dib, C. S. Kim, and J. D. Kim. Lepton flavor violation in tau decays. *Phys. Rev. D*, 66:034008, Aug 2002.
- [27] Hsin-Chia Cheng and Ian Low. Tev symmetry and the little hierarchy problem. *Journal of High Energy Physics*, 2003(09):051–051, Sep 2003.
- [28] Hsin-Chia Cheng and Ian Low. Tev symmetry and the little hierarchy problem. *Journal of High Energy Physics*, 2003(09):051–051, Sep 2003.
- [29] Howard Georgi and A. Pais. Calculability and Naturalness in Gauge Theories. *Phys. Rev. D*, 10:539, 1974.
- [30] Michael J. Dugan, Howard Georgi, and David B. Kaplan. Anatomy of a Composite Higgs Model. *Nucl. Phys. B*, 254:299–326, 1985.
- [31] Martin Schmaltz and David Tucker-Smith. Little higgs theories. *Annual Review of Nuclear and Particle Science*, 55(1):229–270, Dec 2005.
- [32] Chong-Xing Yue, Zheng-Jun Zong, Li Zhou, and Shuo Yang. Lepton flavor violating signals of the neutral top-pion in future lepton colliders. *Phys. Rev. D*, 71:115011, Jun 2005.
- [33] William J. Marciano, Toshinori Mori, and J.Michael Roney. Charged Lepton Flavor Violation Experiments. *Ann. Rev. Nucl. Part. Sci.*, 58:315–341, 2008.

- [34] J. P. Lees, V. Poireau, E. Prencipe, V. Tisserand, J. Garra Tico, E. Grauges, M. Martinelli, A. Palano, M. Pappagallo, G. Eigen, and et al. Limits on  $\tau$  lepton-flavor violating decays into three charged leptons. *Physical Review D*, 81(11), Jun 2010.
- [35] K. Hayasaka et al. Search for Lepton Flavor Violating Tau Decays into Three Leptons with 719 Million Produced Tau+Tau- Pairs. *Phys. Lett. B*, 687:139–143, 2010.
- [36] R. Aaij, B. Adeva, M. Adinolfi, A. Affolder, Z. Ajaltouni, S. Akar, J. Albrecht, F. Alessio, M. Alexander, and et al. Search for the lepton flavour violating decay  $\tau^- \rightarrow \mu^- \mu^+ \mu^-$ . *Journal of High Energy Physics*, 2015(2), Feb 2015.
- [37] E Kou, P Urquijo, W Altmannshofer, F Beaujean, G Bell, M Beneke, I I Bigi, F Bishara, M Blanke, C Bobeth, and et al. The belle ii physics book. *Progress of Theoretical and Experimental Physics*, 2019(12):689, Dec 2019.
- [38] M. Baszczyk et al. SuperB Technical Design Report. *arXiv 1306.5655*, 6 2013.
- [39] Pantaleo Raimondi. Status on SuperB effort. , 2006. Talk given at the 2nd SuperB Workshop at Frascati (Italy), available at: <http://www.lnf.infn.it/conference/superb06/talks/raimondi1.ppt>.
- [40] T. Abe et al. Belle II Technical Design Report. *arXiv 1011.0352*, 11 2010.
- [41] P.M. Lewis, I. Jaegle, H. Nakayama, A. Aloisio, F. Ameli, M. Barrett, A. Beaulieu, L. Bosisio, P. Branchini, T.E. Browder, and et al. First measurements of beam backgrounds at superkekb. *Nuclear Instruments and Methods in Physics Research Section A: Accelerators, Spectrometers, Detectors and Associated Equipment*, 914:69–144, Jan 2019.
- [42] I. Adachi et al. Search for an Invisibly Decaying  $Z'$  Boson at Belle II in  $e^+e^- \rightarrow \mu^+\mu^-(e^\pm\mu^\mp)$  Plus Missing Energy Final States. *Phys. Rev. Lett.*, 124(14):141801, 2020.
- [43] F. Abudinén, I. Adachi, P. Ahlburg, H. Aihara, N. Akopov, A. Aloisio, F. Ameli, L. Andricsek, N. Anh Ky, D. M. Asner, and et al. Measurement of the integrated luminosity of the phase 2 data of the belle ii experiment. *Chinese Physics C*, 44(2):021001, Jan 2020.

- [44] S. Belov, B. Suo, Z.Y. Deng, V. Korenkov, W.D. Li, T. Lin, Z.T. Ma, C. Nicholson, I. Pelevanyuk, V. Trofimov, A. Uzhinskiy, T. Yan, X.F. Yan, X.M. Zhang, and A. Zhemchugov. Design and operation of the bes-iii distributed computing system. *Procedia Computer Science*, 66:619 – 624, 2015. 4th International Young Scientist Conference on Computational Science.
- [45] Torben Ferber and Phillip Urquijo. Overview of the Belle II Physics Generators. *Internal Belle II note*, Jun 2015.
- [46] T. Kuhr, C. Pulvermacher, M. Ritter, T. Hauth, and N. Braun. The belle ii core software. *Computing and Software for Big Science*, 3(1):1, 2018.
- [47] Anders Ryd, David Lange, Natalia Kuznetsova, Sophie Versille, Marcello Rotondo, David P. Kirkby, Frank K. Wuerthwein, and Akimasa Ishikawa. EvtGen: A Monte Carlo Generator for B-Physics. , 5 2005.
- [48] Torbjörn Sjöstrand, Stefan Ask, Jesper R. Christiansen, Richard Corke, Nishita Desai, Philip Ilten, Stephen Mrenna, Stefan Prestel, Christine O. Rasmussen, and Peter Z. Skands. An introduction to pythia 8.2. *Computer Physics Communications*, 191:159–177, Jun 2015.
- [49] S. Agostinelli et al. GEANT4: A Simulation toolkit. *Nucl.Instrum.Meth.*, A506:250–303, 2003.
- [50] I. Antcheva, Maarten Ballintijn, Bertrand Bellenot, Marek Biskup, Rene Brun, Nenad Buncic, Ph Canal, Diego Casadei, Olivier Couet, Valeri Fine, Leandro Franco, Gerardo Ganis, Andrei Gheata, David Maline, Masaharu Goto, Jan Iwaszkiewicz, Anna Kreshuk, Diego Segura, Richard Maunder, and Matevz Tadel. Root - a c++ framework for petabyte data storage, statistical analysis and visualization. *Computer Physics Communications*, 180:2499–2512, 06 2011.
- [51] The Belle II collaboration. Muon and electron identification efficiencies and hadron-lepton mis-identification probabilities. *40th International Conference on High Energy Physics (ICHEP)*, Jul 2020.
- [52] H. Czyż, M. Gunia, and J.H. Kühn. Simulation of electron-positron annihilation into hadrons with the event generator PHOKHARA. *JHEP*, 08:110, 2013.

- [53] D.W. Bliss et al. New limits for neutrinoless tau decays. *Phys. Rev. D*, 57:5903–5907, 1998.
- [54] Albert M Sirunyan et al. Search for the lepton flavor violating decay  $\tau \rightarrow 3\mu$  in proton-proton collisions at  $\sqrt{s} = 13$  TeV. *arXiv 2007.05658*, 7 2020.
- [55] Morad Aaboud et al. A search for lepton-flavor-violating decays of the  $Z$  boson into a  $\tau$ -lepton and a light lepton with the ATLAS detector. *Phys. Rev. D*, 98:092010, 2018.
- [56] Giovanni Punzi. Sensitivity of searches for new signals and its optimization. *eConf*, C030908:MODT002, 2003.
- [57] P.V.C. Hough. Machine Analysis of Bubble Chamber Pictures. *Conf. Proc. C*, 590914:554–558, 1959.
- [58] F.A. Berends, R. Pittau, and R. Kleiss. All electroweak four-fermion processes in electron-positron collisions. *Nuclear Physics B*, 424(2):308 – 342, 1994.
- [59] Frederik Beaujean, Allen Caldwell, D. Greenwald, S. Kluth, Kevin Kröniger, and O. Schulz. Bayesian analysis toolkit: 1.0 and beyond. *Journal of Physics: Conference Series*, 664:072003, 12 2015.
- [60] W. Gilks, Sylvia Richardson, and D. Spiegelhalter. Introducing markov chain monte carlo. *Markov Chain Monte Carlo in Practice*, 01 1996.
- [61] F. James. MINUIT Function Minimization and Error Analysis: Reference Manual Version 94.1. *CERN-D-506*, 1994.
- [62] Lorenzo Moneta, Kevin Belasco, Kyle S. Cranmer, S. Kreiss, Alfio Lazzaro, Danilo Piparo, Gregory Schott, Wouter Verkerke, and Matthias Wolf. The RooStats Project. *PoS*, ACAT2010:057, 2010.
- [63] Nicholas Metropolis, Arianna W. Rosenbluth, Marshall N. Rosenbluth, Augusta H. Teller, and Edward Teller. Equation of state calculations by fast computing machines. *The Journal of Chemical Physics*, 21(6):1087–1092, 1953.
- [64] Allen C. Caldwell, Daniel Kollar, and Kevin Kroninger. BAT: The Bayesian analysis toolkit. *J. Phys. Conf. Ser.*, 219:032013, 2010.